TRIUMF

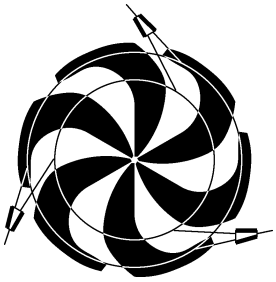

ANNUAL REPORT
SCIENTIFIC ACTIVITIES
2002

ISSN 1492-417X

CANADA'S NATIONAL LABORATORY
FOR PARTICLE AND NUCLEAR PHYSICS

OPERATED AS A JOINT VENTURE

MEMBERS:

THE UNIVERSITY OF ALBERTA
THE UNIVERSITY OF BRITISH COLUMBIA
CARLETON UNIVERSITY
SIMON FRASER UNIVERSITY
THE UNIVERSITY OF VICTORIA

ASSOCIATE MEMBERS:

THE UNIVERSITY OF MANITOBA
McMASTER UNIVERSITY
L'UNIVERSITÉ DE MONTRÉAL
QUEEN'S UNIVERSITY
THE UNIVERSITY OF REGINA
THE UNIVERSITY OF TORONTO

UNDER A CONTRIBUTION FROM THE
NATIONAL RESEARCH COUNCIL OF CANADA

DECEMBER 2003

The contributions on individual experiments in this report are outlines intended to demonstrate the extent of scientific activity at TRIUMF during the past year. The outlines are not publications and often contain preliminary results not intended, or not yet ready, for publication. Material from these reports should not be reproduced or quoted without permission from the authors.

Experiment 768

Generalized FFLO state and anomaly of flux line lattice state in novel superconductors

(R. Kadono, J. Akimitsu, KEK-IMSS, Aoyama-Gakuin)

The revelation of superconductivity in a binary intermetallic compound, MgB_2, has attracted much interest because it exhibits a transition temperature T_c almost two times higher than those of all other intermetallic superconductors known to date [Nagamatsu, *et al.*, Nature **410**, 63 (2001)]. The most interesting issue associated with this compound is whether or not it belongs to the class of conventional BCS type superconductors. In order to obtain information on the order parameter in MgB_2, we have observed the temperature and field dependence of magnetic penetration depth λ by muon spin rotation.

This μSR experiment was performed on the M15 beam line at TRIUMF using the high time resolution spectrometer Belle which allows μSR measurements up to 5 T. A muon-veto counter system was adopted to eliminate positron events from muons which missed the sample so that the relative yield of such events was less than 5% of the total positron events. The sample was field-cooled at the measured magnetic fields in order to eliminate the effect of flux pinning.

We show the temperature dependence of the muon depolarization rate σ_1 in Fig. 78. These data were obtained under a field $H \simeq 0.5$ T which is well above $H_{c1} \sim 10^{-2}$ T. The data were fitted by the two-gap model [Bouquet *et al.*, Europhys. Lett. **56**, 856 (2001); Ohishi *et al.*, J. Phys. Soc. Jpn., in press]. The solid line in Fig. 78 is the best fit result with $\Delta_1 = 4.9(1)$ meV, $\Delta_2 = 1.2(3)$ meV, $w = 0.84(3)$ and $T_c = 36.48(3)$ K. The dotted line shows the result of fitting using the values of Δ_1, Δ_2 and w in Niedermayer *et al.* [Phys. Rev. **B65**, 094512 (2002)]. Although our result shows reasonable agreement with Niedermayer *et al.*, the value of Δ_2 is considerably smaller than the reported value of 2.6(2) meV.

The field dependence of λ is shown in Fig. 79. It clearly exhibits a strong field dependence where $\lambda(h)$ increases almost linearly with $h \equiv H/H_{c2}$. This is similar to the cases of YNi_2B_2C [Ohishi *et al.*, Phy. Rev. **B65**, 140505R (2002)], $NbSe_2$ [Sonier *et al.*, Phys. Rev. Lett. **79**, 1742 (1997)] and high-T_c cuprate superconductors [Sonier *et al.*, Rev. Mod. Phys. **72**, 769 (2000)], where the increase of λ is attributed to the anisotropic order parameters and the associated nonlinear effect due to the Doppler shift of the quasiparticles in the nodal region ($\Delta(k) \simeq 0$) [Volovik, JETP Lett. **58**, 469 (1993)]. The field dependence of λ is expected to be stronger when the phase space satisfying $\Delta(k) \simeq 0$ has larger volume. A fitting by the relation $\lambda(h) = \lambda(0)[1 + \eta \cdot h]$ provides a dimensionless parameter η which represents the strength of the pair breaking effect. We obtain $\eta = 1.27(29)$ with $\lambda(0) = 116.1(6.2)$ nm which is shown as the solid line in Fig. 79. The obtained value of η is intermediate between that in YNi_2B_2C and $NbSe_2$ (e.g., $\eta = 0.97$ at $0.2\ T_c$, $\eta = 1.61$ at $0.33\ T_c$, respectively) and is smaller than those in d-wave superconductors (e.g., $\eta = 5.5 \sim 6.6$ for cuprates).

Our result on the temperature dependence of σ_1 is qualitatively consistent with earlier results [Niedermayer *et al., op. cit.*], suggesting that the order parameter in MgB_2 may be effectively described by adopting the two-gap model. However, the observed field dependence of λ is not expected for the isotropic order parameter irrespective of the multiplicity of the

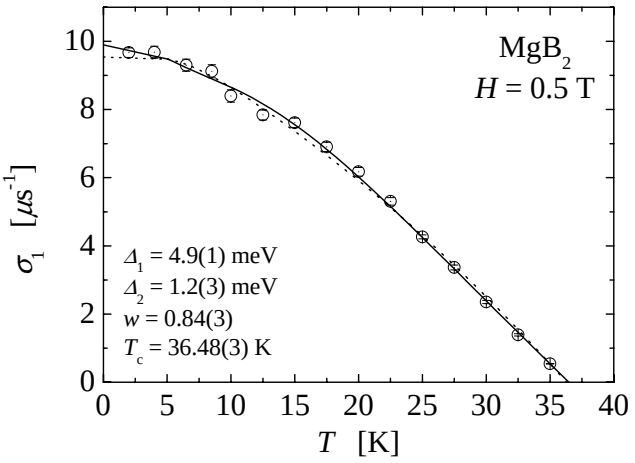

Fig. 78. T dependence of σ_1 at $H = 0.5$ T.

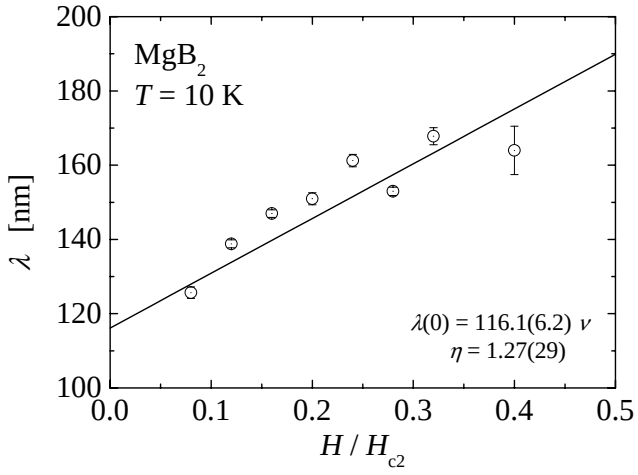

Fig. 79. H dependence of λ at $T \simeq 10$ K.

band structure and the associated gap energy. Considering that the current result on the field dependence of λ was obtained at $T \simeq 10$ K, this energy scale of $\varepsilon \equiv k_B T \sim 1$ meV places an upper boundary on the smaller gap energy Δ_2 in order to explain the observed effect of the Doppler shift. Since our estimation for $\Delta_2 = 1.2(3)$ meV is very close to ε, the observed H-linear behaviour of λ may be attributed to the quasiparticle excitations in the vicinity of the smaller gap. While this cannot be distinguished from the case of a nodal structure in the order parameter (i.e., considering a region where $\Delta(k) \ll \varepsilon$), our result is clearly inconsistent with the two-gap model with $\Delta_2 \gg \varepsilon$. On the other hand, it is also quite unlikely that the d-wave pairing is realized in MgB_2, because the coefficient η is much smaller than those in high-T_c cuprates. The recent observation that the order parameter in YNi_2B_2C (where the pairing symmetry has been identified as s-wave [Shu *et al.*, Phys. Rev. **B54**, 15341 (1996)]) has point nodes [Izawa *et al.*, Phys. Rev. Lett. **89**, 137006 (2002)] exhibits a good correspondence with the intermediate value of $\eta(\sim 1)$ obtained by μSR [Ohishi *et al.*, Phys. Rev. **B65**, 140505R (2002)], suggesting that there is a similar situation in MgB_2. Thus, the present μSR result leads us to conclude that the order parameter in MgB_2 has a structure with an energy gap smaller than $\varepsilon \simeq 1$ meV. The field dependence of λ measured at a much lower temperature would provide more useful information to distinguish the anisotropic order parameter from the isotropic one described by the two-gap model.

In summary, we have performed TF-μSR measurements in MgB_2 to obtain the temperature and magnetic field dependence of the penetration depth λ and the associated spin relaxation rate σ_1. Our result is perfectly in line with the presence of an anisotropic order parameter with a nodal structure, and it sets an upper boundary $\varepsilon \simeq 1$ meV for the smaller gap energy in the two-gap model. The magnetic field dependence of λ exhibits a linear dependence on the external field up to 5 T with the gradient η being considerably smaller than that in d-wave superconductors, which may disfavour the occurrence of d-wave pairing in MgB_2.

Experiment 782
Non-Fermi-liquid behaviour and other novel phenomena in heavy-fermion alloys

(D.E. MacLaughlin, California, Riverside)

Isotropic pairing in superconducting $PrOs_4Sb_{12}$

In most heavy-fermion (HF) metals and superconductors the f ion (Ce, Yb, U) has a magnetic ground state. HF behaviour has, however, been reported in a small number of praseodymium-based alloys and compounds [Yatskar *et al.*, Phys. Rev. Lett. **77**, 3637 (1996)], in which the crystalline electric field (CEF) ground state of the non-Kramers Pr^{3+} ion could be nonmagnetic and degenerate. In this case a charge-scattering analogue of Kondo spin scattering can give rise to the so-called "quadrupolar Kondo effect", an example of the two-channel Kondo effect that has been invoked to explain non-Fermi-liquid behaviour in HF systems [Cox and Jarrell, J. Phys.: Cond. Matter **8**, 9825 (1996)].

Superconductivity has recently been discovered in the cubic HF compound $PrOs_4Sb_{12}$ [Bauer *et al.*, Phys. Rev. **B65**, 100506 (2002)]. From thermodynamic measurements it is found that a large carrier effective mass $m^* \approx 50\, m_e$ characterizes both the normal and superconducting states, and the transition temperature $T_c = 1.85$ K is relatively high for a HF superconductor. Although a conventional spin-based HF mechanism has not been completely ruled out, thermodynamic properties of $PrOs_4Sb_{12}$ suggest a Pr^{3+} nonmagnetic doublet Γ_3 CEF ground state, so that the quadrupolar Kondo effect is a candidate mechanism for the HF behaviour. The symmetry of the superconducting pairing in such a system is a fundamental question.

In general the muon spin relaxation rate is related to the rms width $[\overline{(\Delta B)^2}]^{1/2}$ of the internal magnetic field distribution $n(B)$ in the vortex state of type-II superconductors [Sonier *et al.*, Rev. Mod. Phys. **72**, 769 (2000)]. In turn $[\overline{(\Delta B)^2}]^{1/2}$ is inversely proportional to the square of the magnetic penetration depth λ, which is related to the density n_s of superconducting carriers and m^* by the London equation

$$1/\lambda^2 = 4\pi n_s e^2/m^* c^2 \,. \qquad (1)$$

The temperature dependence of λ at low temperatures is therefore sensitive to the lowest-lying superconducting excitations, the thermal population of which reduces n_s with increasing temperature. In the presence of an isotropic or nearly isotropic energy gap, $\lambda(T) - \lambda(0)$ varies exponentially with temperature, whereas nodes in the gap function characteristic of non-s-wave pairing lead to power-law dependences.

We have carried out zero- and transverse-field μSR experiments in the superconducting state of $PrOs_4Sb_{12}$ using the dilution refrigerator at the TRIUMF M15 beam line. The penetration depth derived from the vortex-lattice field distribution width exhibits the temperature dependence characteristic of isotropic s-wave pairing. Isotropic p-wave pairing, which is indistinguishable from s-wave pairing by thermodynamic or electrodynamic measurements, is also possible. To our knowledge this is the only example to date of an isotropic gap in a HF superconductor. It suggests the possibility of (a) marked differences in superconducting properties between HF materials with magnetic and

nonmagnetic f-ion ground states, and (b) a relation between the pairing symmetry and the mechanism (spin or quadrupole Kondo effect) for the HF normal state from which the superconductivity evolves.

Zero-field μSR experiments were performed to determine whether static magnetism exists in the superconducting state of $PrOs_4Sb_{12}$. The zero-field data are well fit by the product of a damping exponential and the Kubo-Toyabe (K-T) function expected from nuclear dipolar fields. The exponential damping rate $W(T)$ is already appreciable in the normal state, increases only slightly more than experimental uncertainty below T_c, and is (negatively) correlated with the K-T rate $\Delta_{\rm KT}(T)$ in the fitting process. Thus there is no statistically significant evidence for static magnetism below T_c; the present data place an upper limit of $\sim$50 μT on any static field below T_c.

The internal field distribution in the vortex state is the convolution of the field distributions due to the vortex lattice and to the electronic and nuclear moments of the host material; by the convolution theorem the muon-spin precession signal is the product of the Fourier transforms of these distributions. The superconducting-state data have been fit to a product of exponential and Gaussian functions, where the latter is taken as an approximation to the relaxation function due to the vortex-lattice field distribution.

The temperature dependence of the Gaussian relaxation rate σ_s is shown in Fig. 80 for an applied field of 200 Oe. Salient features of these data are that $\sigma_s(T)$ varies only slowly at low temperatures, and that the $T = 0$ value $\sigma_s(0) = 0.91(1)$ μs^{-1}. This is large for a HF superconductor and is much larger than changes

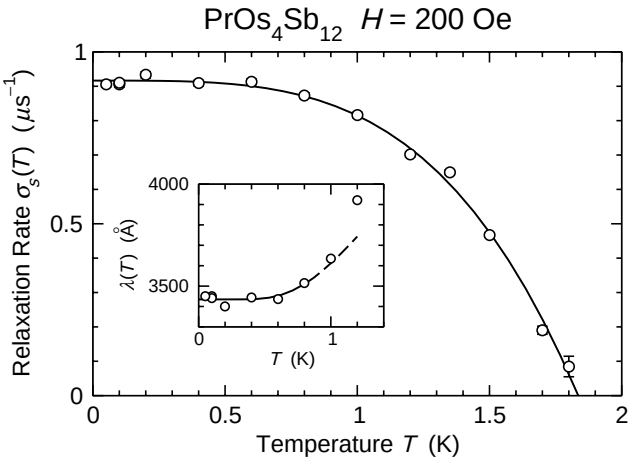

Fig. 80. Temperature dependence of vortex-state μ^+ relaxation rate $\sigma_s(T)$ in the superconducting state of $PrOs_4Sb_{12}$. Curve: $\sigma_s(T) = \sigma_s(0)[1 - (T/T_c)^y]$, $\sigma_s(0) = 0.91(1)$ μs^{-1}, $T_c = 1.83(2)$ K, $y = 3.6(2)$. Inset: low-temperature penetration depth $\lambda(T)$ derived from $\sigma_s(T)$. Curve: $\lambda(T) = \lambda(0)[1 + (\pi\Delta/2T)^{1/2}\exp(-\Delta/T)]$, $\lambda(0) = 3440(20)$ Å, $\Delta/T_c = 2.1(2)$, from fit to data for $T \leq 0.8$ K.

in the ZF-μSR rates, so that σ_s is dominated by the vortex-state field distribution.

We obtain λ from σ_s and the expression

$$\overline{(\Delta B)^2} = 0.00371\,\Phi_0^2\lambda^{-4}\,, \qquad (2)$$

appropriate to an isotropic extreme type-II superconductor, where Φ_0 is the flux quantum. The data are shown in the inset to Fig. 80. The BCS low-temperature expression $\lambda(T) = \lambda(0)[1 + (\pi\Delta/2T)^{1/2}\exp(-\Delta/T)]$ was fit to data for $T \leq 0.8$ K $< 0.4\,T_c$; the curve in the inset to Fig. 80 shows this fit and its extension (dashed) up to 1.2 K. The fit value $\lambda(0) = 3440(20)$ Å is short for a HF superconductor. The fit value of the ratio $\Delta/T_c = 2.1(2)$ is somewhat larger than the BCS value 1.76, suggesting strong coupling. Over the entire temperature range $\sigma_s(T)$ is consistent with the phenomenological "two-fluid" temperature dependence $1/\lambda^2(T) \propto 1 - (T/T_c)^4$, although the data are slightly better fit with an exponent of 3.6(2) (curve). All these properties indicate that the gap is isotropic or nearly so. Proportionality between $\overline{(\Delta B)^2}$ and λ^{-4} should survive vortex lattice disorder as long as the distance between vortices is much smaller than λ ($H \gg H_{c1}$); disorder increases the numerical coefficient in Eq. (2) but should not affect the temperature dependence of $\overline{(\Delta B)^2}$.

Early studies of the penetration depth in cuprate superconductors using unaligned powders also observed little temperature dependence of λ at low temperatures, and concluded that the pairing was s-wave [Sonier *et al., op. cit.*]. Later measurements in high-quality aligned crystals revealed the linear temperature dependence characteristic of d-wave pairing. The early results appear to have been due to a combination of circumstances: strong anisotropy in λ, oxygen inhomogeneity, and sensitivity to hole doping due to the low density n_s of superconducting carriers. None of these factors would seem to affect the current measurements. The crystal structure of $PrOs_4Sb_{12}$ is cubic, so that the penetration depth is isotropic. With $m^* \approx 50\,m_e$ we find $n_s \approx 10^{22}$ carriers/cm^3 from Eq. (1), so that $PrOs_4Sb_{12}$ is a good metal and the carrier concentration is insensitive to chemical inhomogeneity. Thus it seems unlikely that the observed temperature dependence of $\lambda(T)$ is due to extrinsic effects.

The resistive mean free path ℓ can be calculated from the residual resistivity $\rho(0) \approx 5$ $\mu\Omega$-cm using n_s as an estimate of the normal-state carrier concentration, and can be compared with the superconducting coherence length ξ_0 [Bauer *et al., op. cit.*]. We find $\ell/\xi_0 \approx 3$, so that $PrOs_4Sb_{12}$ is a rather clean superconductor (and Eq. (1), derived in the clean limit, is

valid); this is of importance in the analysis of thermodynamic properties.

The isotropy of the superconducting energy gap indicated by the temperature dependence of σ_s (Fig. 80) strongly suggests that superconductivity in $PrOs_4Sb_{12}$ is in some sense "conventional." In this regard $PrOs_4Sb_{12}$ differs markedly from other HF superconductors studied to date, a difference that may possibly be related to a nonmagnetic or quadrupolar Kondo state in this compound. Better understanding of the quadrupolar Kondo lattice will be needed to elucidate the questions of whether $PrOs_4Sb_{12}$ is indeed such a system and, if so, whether this property is related to the conventional superconducting behaviour.

Experiments 815, 816 and 817: β-NMR

(W.A. MacFarlane, R.F. Kiefl, TRIUMF/UBC)

The positive muon beams at TRIUMF and associated instruments are an excellent way to probe the magnetic properties of bulk materials. Over the past few years we have developed a closely related technique called β-detected NMR which uses the low energy radioactive ion beams from ISAC. These instruments complement muon spin rotation in that they can be used to probe magnetic and electronic properties of nanostructures and ultrathin films. Recently we have commissioned a second β-NMR spectrometer for carrying out nuclear quadrupole resonance in zero static external field. In particular we have observed nuclear quadrupole resonances of ^{8}Li in several crystals such as $SrTiO_3$, Al_2O_3 and Sr_2RuO_4. We anticipate that, as in the case of μSR, the ability to carry out measurements in zero external magnetic field will have significant applications in the area of magnetism and superconductivity. More details are given in the next section.

We also made progress in quantifying the beam spot imaging that we perform with a CCD camera by correlating these images with the β count rates. An example of the light output in a section through the beam spot is shown in Fig. 81, indicating the high quality of the beamspot for this energy and magnetic field.

β-detected pure quadrupole resonance

The most significant advance over the last year is the demonstration of β-detected nuclear quadrupole resonance. Nuclei with spins greater than $\frac{1}{2}$ possess electric quadrupole moments which couple the nuclear spin to the local gradient of the electric field (EFG). In a single crystal for a single site with an axially symmetric EFG, this leads to an effective spin Hamiltonian of the form [see Das and Hahn, *Nuclear quadrupole resonance spectroscopy* (Academic, NY, 1958) for example]: $H_Q = \frac{1}{6}h\nu_Q[3m^2 - I(I+1)]\delta_{mm'}$, where $h\nu_Q$ is the scale of the quadrupolar coupling, I and m are the

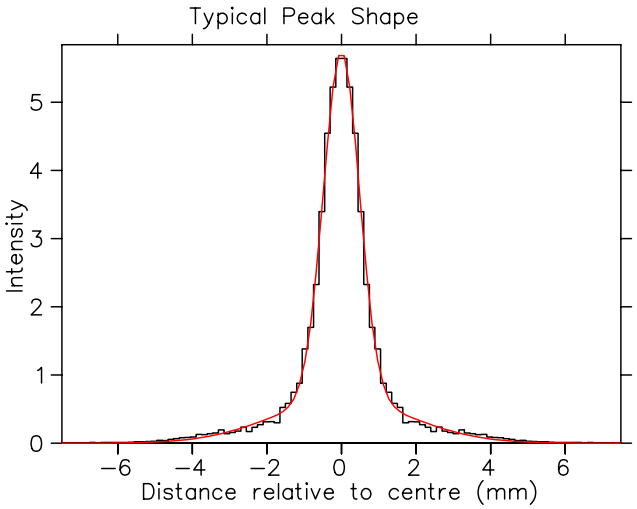

Fig. 81. A quantitative measure of the beam spot as measured by a CCD camera imaging a scintillator mounted at the sample position.

nuclear spin quantum number and the magnetic quantum number with a quantization axis (z) defined by the direction of maximal EFG. The quadrupolar spectrum is thus very simple with just two transition frequencies at $\frac{\nu_Q}{2}$ and $\frac{3\nu_Q}{2}$. Provided the initial polarization has a component in the z direction, then we should observe a resonant loss of the β decay asymmetry when the frequency of H_1 (the oscillating transverse magnetic field) matches the quadrupolar level splitting.

By analogy with conventional nuclear magnetic resonance, we call this zero field technique β-NQR. For light nuclei like ^{8}Li, the nuclear electric quadrupole moment is small (+32 mB), so the quadrupole coupling ν_Q is small. For ^{8}Li we expect it to be less than 200 kHz in most cases. These low frequencies were beyond the range of the rf system designed for the high field spectrometer. Consequently we developed a radio/audio frequency irradiation system which can irradiate either with a single frequency ν or an equal combination of ν and 3ν. In the case of high initial polarization, only the $m = \pm 2$ state is initially occupied and irradiation at $\frac{3\nu_Q}{2}$ will yield a small change in the asymmetry as the transition is saturated. To achieve full saturation, i.e. equalization of the populations of the magnetic states, yielding zero asymmetry, we thus require the two frequency irradiation. Figure 82 shows such a signal in an epitaxially prepared $\langle 100 \rangle$ crystal of $SrTiO_3$ at room temperature. We expected this value for ν_Q from our prior observations of quadrupolar splitting of the high field resonance in this material.

Conventional metals

Previously we observed a split resonance of ^{8}Li near the Larmor frequency in high magnetic field (3 T) in Ag and Au. We have proposed that this was due to two distinct Li sites differing in their Knight shifts. In

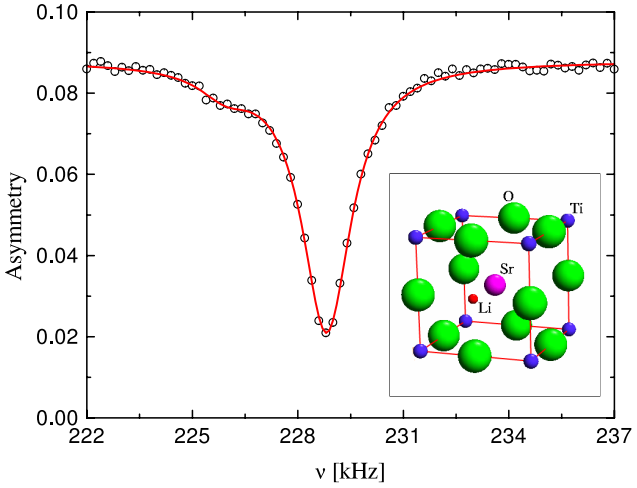

Fig. 82. The β-NQR signal of interstitial ^{8}Li $SrTiO_3$. The spectrum is taken at room temperature in zero applied field.

order to test this hypothesis it was necessary to carry out measurements in much lower magnetic field (0.3 T) where the back detector has a very small effective solid angle due to the reduced magnetic field. This is now possible since we have also commissioned a new neutral beam monitor (NBM), which detects βs from polarized neutral Li that is not reionized in the He cell of the polarizer. This in turn allows measurements with a single forward detector which can be normalized to the incoming beam rate as measured at the NBM. The NBM is now commissioned and fully integrated into the data acquisition system. The data on Ag were taken at 0.3 T and show a very narrow line at all temperatures. This confirms that the lines at high field are split because of a site dependent Knight shift.

In Ag and Au we have observed the split resonance now in several samples, but in addition only in Au in a temperature range around 225 K, at 0.3 T, we find a broad line in addition to the narrow one corresponding to the 2 cubic sites (unresolved here). Figure 83 shows an example of this line. We speculate that it is due to a transition state, i.e. the Li spends significant time just adjacent to a local-cubic-symmetry-breaking vacancy. It occurs in the same temperature regime where the amplitudes of the two lines we resolve at high field are changing.

Having developed the low frequency capability in order to measure the β-NQR, we also demonstrated that we can observe conventional β-NMR resonances in very small applied magnetic fields. Note the β-NQR spectrometer at the polarimeter station is equipped with a Helmholtz coil, allowing a static field of up to 0.015 T to be applied. Figure 84 shows such a resonance. Conventional NMR relies on thermal polarization of the nuclear spins (unlike the highly athermal polarization produced optically in the ^{8}Li beam), thus resonance in such low fields is nearly impossible.

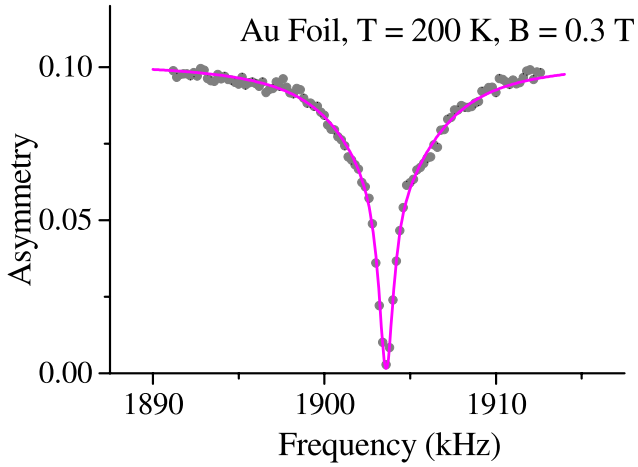

Fig. 83. The β-NMR signal of interstitial ^{8}Li in a high purity annealed Au foil. These data were taken with 1.7 W of rf power and full beam energy (30 keV). Notice the broad line superimposed on the narrow line at the Larmor frequency which is likely due to Li that is trapped adjacent to an Au vacancy.

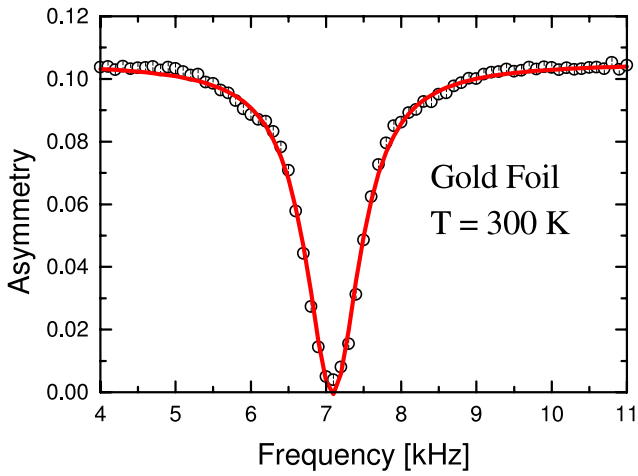

Fig. 84. The β-NMR signal of interstitial ^{8}Li in annealed high purity gold at room temperature in a field of about 11 G.

Superconductors

Recently, we have implanted ^{8}Li near the surface of a conventional superconductor $NbSe_2$. We find a remarkably small quadrupolar frequency ν_Q for interstitial ^{8}Li, even though the crystal is noncubic. From the asymmetry of the resonances for the two nuclear helicities, we estimate that $\nu_Q < 1$ kHz, considerably smaller than what is seen in analogous stable Li intercalation compounds [Prigge *et al.*, Z. Phys. Chem. **189**, 153 (1995)]. Above the critical temperature we observe a single resonance at the Larmor frequency with unresolved quadrupolar effects.

When a type II superconductor is cooled in a magnetic field H, for H in a certain range, the field will become inhomogeneous due to the formation of a lattice

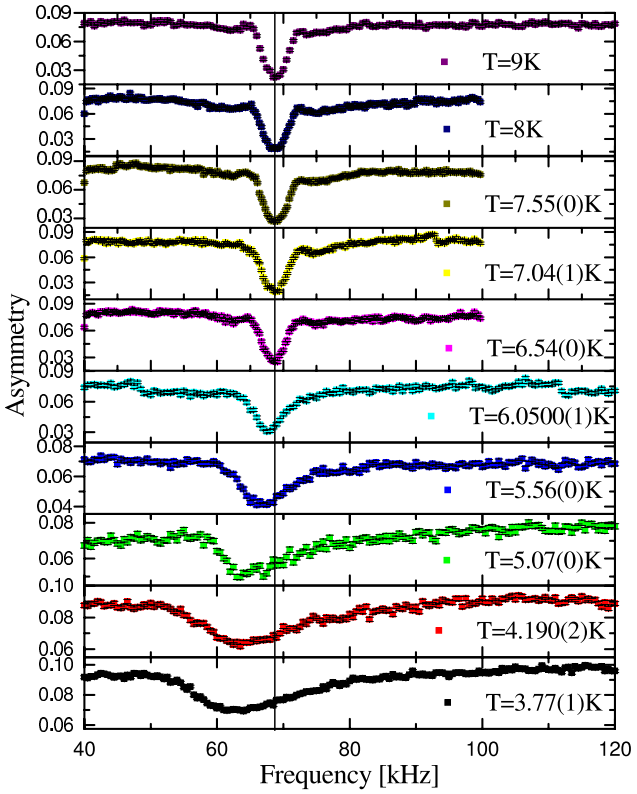

Fig. 85. The β-NMR signal of interstitial ^{8}Li in a crystal of $NbSe_2$ with $H//c$ (the hexagonal axis). The field H was about 110 G.

of magnetic vortices, a consequence of the superconductor's tendency to screen the field. Such a field inhomogeneity gives rise to the well-known broadening of the magnetic resonance in the superconducting state. In Fig. 85, we detect this effect by observing a broadened line possessing the expected long high frequency tail. Establishing the technique in a well studied superconductor such as $NbSe_2$ is an important step towards the application of β-NMR to the study of properties of the vortex state in exotic and thin film superconductors.

Semiconductors

We have also begun experiments on semiconductors in which the implanted radioactive atom is used to simulate the behaviour of an isolated Li impurity. The inset of Fig. 86 shows the β-NMR resonances at room temperature and at low temperature. In both cases there is a large amplitude line which is attributed to Li at sites which are close to being cubic and thus have no resolved quadrupole splitting. There is, however, a strong temperature dependence to the linewidth shown in the main part of Fig. 86. At low temperatures the width is attributed to nuclear dipolar broadening from the abundant ^{69}Ga, ^{71}Ga and ^{75}As nuclear moments. A slight decrease as the temperature increases from 5 K to 150 K is attributed to motional narrowing

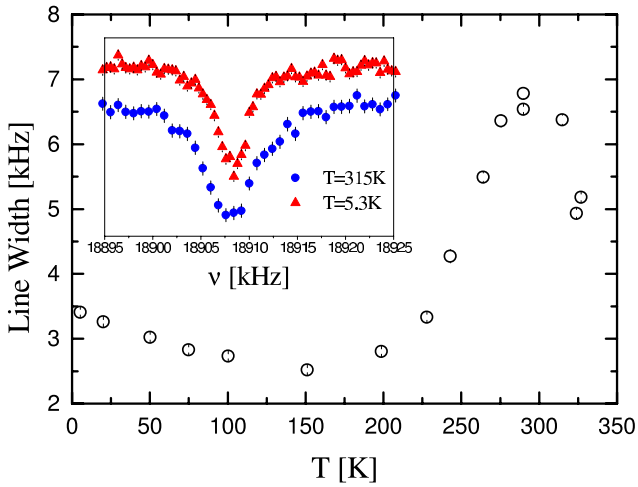

Fig. 86. The linewidth of the β-NMR resonance of ^{8}Li in semi-insulating high purity GaAs with $H \| < 100 >$.

as the Li begins to hop. However, above 150 K the line broadens significantly. This may be due to small unresolved quadrupolar splittings as the Li approaches the vacancies which are presumably created when the Li is implanted. Note the linewidth peaks at about 290 K. The drop at higher temperatures is likely due to the Li occupying the vacancy where the quadrupolar splitting is identically zero. This behaviour is very similar to that seen in the annealed Au foil. Further measurements are required to confirm this scenario.

Experiment 822
Effect of disorder on quantum spin liquid state
(A. Koda, R. Kadono, KEK)

The primary goal of the Expt. 822 collaboration is to elucidate the implicit correlation of quantum spin systems through the effect of controlled disorder on the magnetic property of parent compounds which is best probed by muon-spin-rotation/relaxation (μSR). Recently, an anomalous behaviour reminiscent of heavy f-electron systems, observed in a metallic spinel LiV_2O_4, has been drawing much interest as strong evidence for heavy quasiparticles which are carried by d-electrons. In order to identify the origin of such an enhanced density of states, we have carried out μSR experiments on polycrystalline samples of LiV_2O_4 and $Li_{1-x}Zn_xV_2O_4$ ($0.025 \leq x \leq 0.3$) under zero and longitudinal fields (ZF/LF-μSR) up to 300 mT.

In Fig. 87, typical ZF/LF-μSR time spectra in $Li_{1-x}Zn_xV_2O_4$ with $x = 0$ and 0.05 are shown. No remarkable increase of the relaxation rate corresponding to the development of staggered magnetic moments, as reported for one of the samples (#3) in previous reports [Kondo *et al.*, Phys. Rev. Lett. **78**, 3729 (1997)], was observed in a specimen with $x = 0$ over the investigated range of temperature. The result suggests

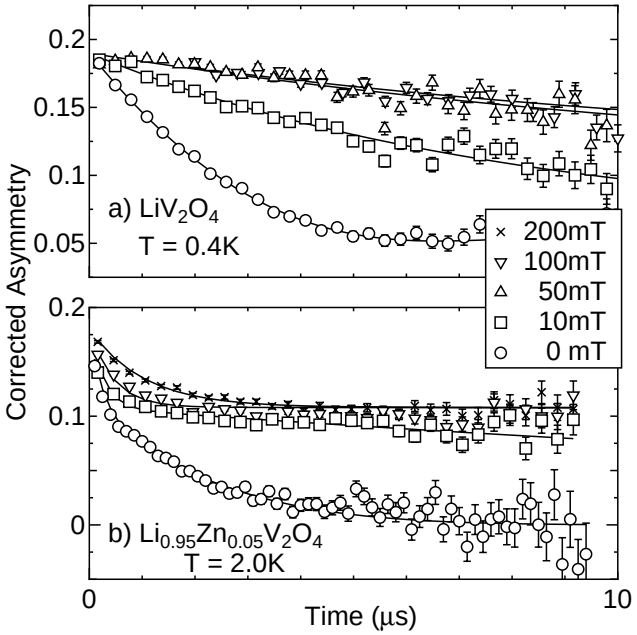

Fig. 87. Time evolution of muon spin polarization in LiV_2O_4 ($T = 0.4$ K) (a) and $Li_{0.95}Zn_{0.05}V_2O_4$ ($T = 2.0$ K) (b) under zero or longitudinal fields up to 200 mT.

the presence of two magnetic components, one which leads to a quasi-static internal field, which is readily quenched under $H \leq 100$ mT, and the other portion, which exerts dynamically fluctuating fields with a considerably high fluctuation rate. This situation is described by the following model of the relaxation function:

$$A_0 G_z(t) = A_0 \left[(1-f)\exp(-\lambda_S t) + f\exp(-\lambda_D t)\right] G_{\rm KT}^{\rm nuc}(t) + A_{\rm BG},$$

where A_0 is the initial asymmetry, λ_S is the relaxation rate for the quasi-static component, f is the fraction of the dynamically fluctuating component with the relaxation rate (λ_D), $G_{\rm KT}^{\rm nuc}$ is a relaxation function arising from the nuclear magnetic moments, and $A_{\rm BG}$ is the background contribution of the silver sample holder. The relaxation rate ($\lambda_i; i = S, D$) is given by Redfield's spectrum density function,

$$\lambda_i(\omega_\mu) = \frac{2{\delta_i}^2 \nu_i}{{\omega_\mu}^2 + {\nu_i}^2}, (i = S, D),$$

where $\omega_\mu \equiv \gamma_\mu H$ with γ_μ being the muon gyromagnetic ratio and H the external field; δ_i and ν_i are the dipolar width and fluctuation rate of each component, respectively. The temperature dependences of δ_i and ν_i in undoped LiV_2O_4 are shown in Figs. 88(a) and (b). The dynamically fluctuating component (λ_D) exhibits a relatively large dipolar width ($\delta_D \sim 10\ \mu s^{-1}$), which is independent of temperature, while the quasi-static one has a much smaller coupling ($\delta_S \sim 1\ \mu s^{-1}$). We

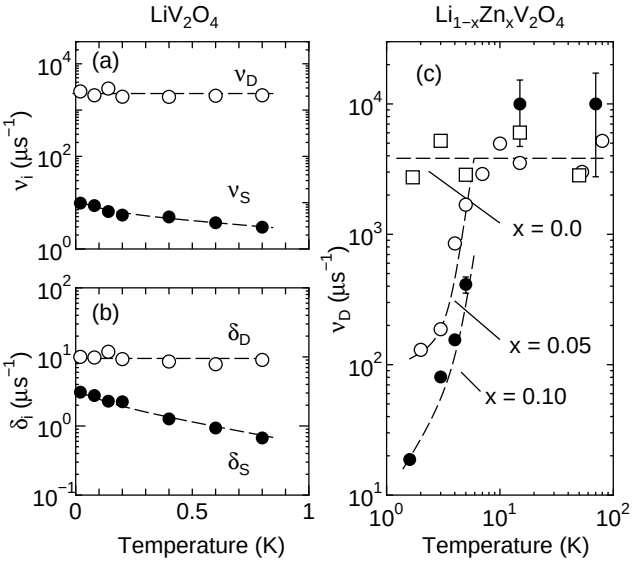

Fig. 88. Temperature dependences of (a) the fluctuation rate (ν_i) and (b) dipolar width (δ_i) in LiV_2O_4. The solid and open symbols represent the quasi-static (S) and the dynamical (D) component, respectively. (c) The fluctuation rate (ν_D) for different Zn concentrations (x), where those with $x > 0$ exhibit a clear tendency of slowing down below ~10 K.

note that the fraction of each component is independent of the temperature below 1 K with almost equal partition. The best-fit result was obtained for $f \sim 0.4$, which rules out the possibility that one of these components may be attributed to an impurity phase.

More direct evidence of phase segregation was obtained by the muon Knight shift in LiV_2O_4 deduced from TF-μSR measurements. In Fig. 89, the fast Fourier-transform (FFT) spectra of the μSR signal at a field of 1 T are shown, together with the Knight shift K vs. susceptibility plot. Two precession signals with different frequencies were observed over the investigated range of temperature (0.02 K $< T <$ 300 K). One having a smaller hyperfine coupling (HFC) constant of -0.27 kOe/μ_B exhibits a nearly temperature-independent behaviour down to 20 mK, implying a narrowed coupling due to a high fluctuation rate corresponding to the dynamical component identified by ZF/LF-μSR. On the other hand, it is notable in Fig. 89 that another part showing a greater HFC constant of $+5.57$ kOe/μ_B exhibits a broadening of the linewidth, which is in line with the temperature dependence of the quasi-static component. This result strongly supports the interpretation that the two components observed in the ZF/LF-μSR spectra originate from different magnetic couplings.

We believe that this phase segregation is intrinsic to LiV_2O_4, because a similar behaviour has been commonly observed in $Li_{1-x}Zn_xV_2O_4$ with varying Zn concentrations, whereas the dynamical property is

strongly dependent on x. In Fig. 88(c), the fluctuation rate (ν_D) exhibits a clear tendency of slowing down with increasing x below ∼10 K. These features indicate that phase segregation into two components having different dynamical character occurs in $Li_{1-x}Zn_xV_2O_4$ irrespective of x, in which the singularity of the undoped LiV_2O_4 is primarily related to the spin fluctuation of the dynamical component (ν_D) persistent even at 20 mK. Thus, we conclude that the observed duality in the magnetism of LiV_2O_4 is intrinsic and cannot be attributed to the second phase or imperfectness of the crystal lattice.

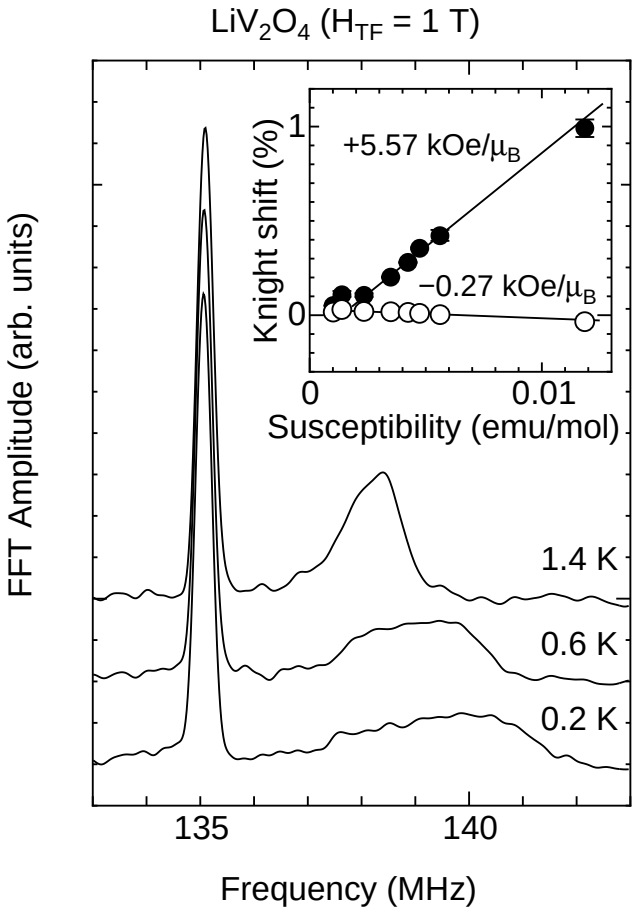

Fig. 89. FFT spectra of the TF-μSR signal under a field of 1 T. The inset shows a Knight shift (K) vs. susceptibility plot at $T > 2$ K.

Experiment 833
Muon spin relaxation studies on MnSi under applied pressure
(I.M. Gat, Columbia)

MnSi is one of the most investigated magnetic systems with itinerant electrons. The compound orders at $T_c = 29.5$ K in a helical magnetic structure with a long period (180 Å). We present μSR studies of a single crystal of MnSi at ambient pressure and under an applied pressure of 8.3 kbar. The critical temperature under 8.3 kbar is reduced to $T_c = 17$ K. At $p_c = 14.6$ kbar, the system becomes a correlated paramagnet.

The unexpected field dependence of the relaxation time T_1 in the paramagnetic phase, for magnetic fields less than 3000 G, is explained based on the helical nature of the magnetic structure. The relaxation time in the paramagnetic state, under the applied pressure of 8.3 kbar and the applied magnetic field of 61.3 G, shows a pronounced curvature when plotted vs. $1/T$. This might be due to the system approaching the ferromagnetic to paramagnetic crossover, where the spin fluctuations with small wave-vector and small energy are predominant, producing a deviation of the uniform susceptibility from the Curie-Weiss law close to the transition. Accordingly, a $T_1 \propto (T/T_c - 1)^2/T$ dependence is expected right above T_c. There is also an intermediate region between the critical region and the high temperature region, where $T_1 \propto ((T/T_c)^{4/3} - 1)/T$.

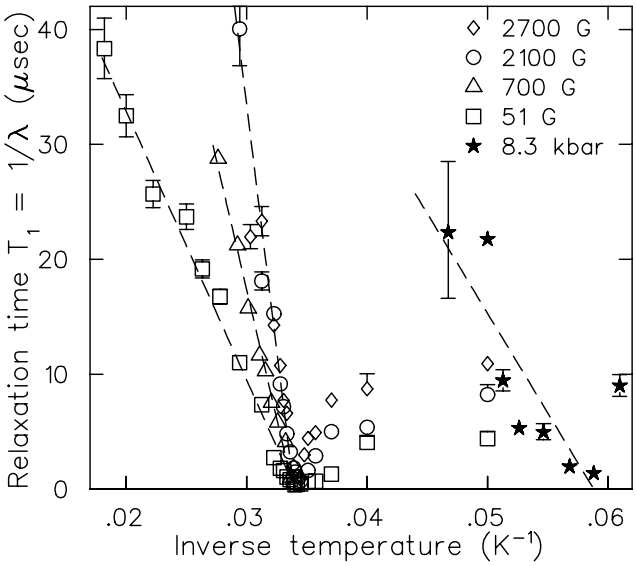

Fig. 90. The muon spin relaxation time T_1 vs. $1/T$ plot under applied magnetic fields of 51.5 G, 2115 G and 2700 G at ambient pressure and under 61.3 G under an applied pressure of 8.3 kbar. Data under 700 G and ambient pressure taken by Dr. Hayano's group [J. Phys. Soc. Japan **49**, 1773 (1980)] confirm our findings.

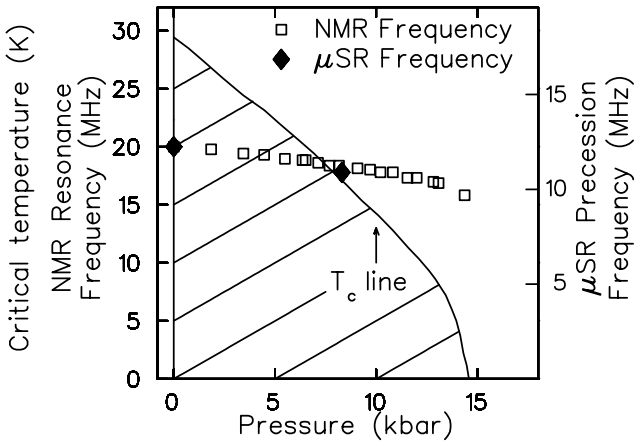

Fig. 91. The muon spin precession frequency in MnSi at 5 K at ambient pressure and under an applied pressure of 8.3 kbar is plotted together with the NMR resonance frequency at 1.4 K measured by Dr. Thessieu's group [J. Magn. Magn. Mater. **177-181**, 609 (1998)]. The μSR data confirm the small decrease of the magnetic moment with increasing pressure. This result might be related to the first order nature of the transition at p_c.

Experiment 834
μSR study of transverse spin freezing in a site-frustrated magnetic glass
(D.H. Ryan, McGill)

Random addition of antiferromagnetic (AF) exchange interactions to an otherwise ferromagnetic (FM) Heisenberg spin system leads to a loss of FM order through the effects of exchange frustration. In extreme cases, a spin glass (SG) is formed with random isotropic spin freezing and neither net magnetization nor long range order. At lower levels of frustration the system exhibits characteristics of both extremes as long-ranged FM order co-exists with SG order in the plane perpendicular to the FM order. On warming such a system from $T = 0$ K, the SG order first melts at T_{xy} followed by the loss of FM order at T_c. This picture has emerged from experimental measurements [Ren and Ryan, Phys. Rev. **B51**, 15885 (1995)], numerical simulations [Thomson *et al.*, Phys. Rev. **B45**, 3129 (1992)] and mean field calculations [Gabay and Toulouse, Phys. Rev. Lett. **47**, 201 (1981)]. The infinite-ranged interactions implicit in mean-field spin glass models make all forms of exchange frustration equivalent. However, real systems are generally dominated by shorter-ranged interactions, and for the case of first-neighbour-only exchange coupling, two distinct situations can be identified: (i) bond frustration [Thomson *et al., op. cit.*] and (ii) site frustration [Nielsen *et al.*, Phys. Rev. **B53**, 343 (1996)].

Bond frustration arises when each exchange bond to a moment's nearest neighbours may be either positive (i.e. ferromagnetic) or negative (i.e. antiferromagnetic). Our earlier work under Expt. 834 has allowed us to use zero-field muon spin relaxation (ZF-μSR) to establish the magnetic phase diagrams of two bond frustrated systems in great detail [Ryan *et al.*, J. Appl. Phys. **89**, 7039 (2001)]. We have shown that the static and dynamic signatures of both T_c and T_{xy} coincide within experimental error: the fluctuation rate diverges at the same temperature at which static order develops. These results are in perfect agreement with the predictions of numerical simulations [Thomson *et al., op. cit.*], and a cross-check using selective excitation double Mössbauer spectroscopy has confirmed that the fluctuations sampled by interstitial muons and those seen at the nuclei of the moment-carrying iron atoms are identical [van Lierop and Ryan, Phys. Rev. Lett. **86**, 4390 (2001)].

Site frustration is achieved by introducing a dopant with AF coupling to all of its nearest neighbours so that the frustration is introduced site-wise rather than bond-wise. While the gross magnetic behaviour is expected to be the same as the bond frustrated case (the system exhibits non-collinear order at low temperatures, there are two magnetic transitions at intermediate dopings and a spin glass at higher dopings), numerical simulations show that there are two striking differences [Nielsen *et al., op. cit.*]. Firstly, low levels of doping do not cause frustration as isolated AF-coupled sites simply order anti-parallel to the majority FM order. Frustration only appears when the dopant density is high enough for AF-AF pairs to occur. Secondly, the transverse correlations below T_{xy} exhibit short-range AF character rather than forming the xy-spin glass observed in the bond frustrated case. The first of these distinctions is clearly seen in the magnetic phase diagrams of manganese-doped metallic glasses, while Mössbauer spectroscopy in a–$(Fe_{1-x}Mn_x)_{78}Sn_2Si_6B_{14}$ [Kuprin *et al.*, Phys. Rev. **B61**, 1267 (2000)] and polarized neutron diffraction from a single crystal of Fe_2MnSi [Ersez *et al.*, J. Phys. : Cond. Matter **7**, 8423 (1995)] have confirmed that the transverse spin components exhibit AF correlations.

While the consistency between experiment and simulation for the two types of frustration appears excellent, one sharply conflicting result exists. A recent ZF-μSR study of a–$(Fe_{0.74}Mn_{0.26})_{75}P_{16}B_6Al_3$ [Mirebeau *et al.*, Hyp. Int. **104**, 343 (1997)] suggested that the static and dynamic signatures of transverse spin freezing at T_{xy} did not coincide. They argued that their data provided evidence for two distinct transitions below T_c: a canting transition at T_K that leads to the development of non-collinearity but involves no dynamical anomaly, followed by a freezing transition at T_F which is associated with strong energy losses and a peak in the fluctuation rate, but no specific change in the magnetic correlations. This three-transition inter-

pretation of the magnetic ordering in this single sample is inconsistent with numerical simulations of site frustrated Heisenberg spin systems [Nielsen *et al., op. cit.*], and the reported disagreement between the static and dynamic signatures of transverse spin freezing in the ZF-μSR data stands in stark contrast to the almost perfect agreement observed at T_{xy} in bond frustrated systems [Ryan *et al., op. cit.*].

The aim of the Expt. 834 runs in the summer was to re-visit this issue in a systematic way in order to clarify the situation. We carried out an extensive study of the entire magnetic phase diagram of a–$(Fe_{1-x}Mn_x)_{78}Si_8B_{14}$ for $0 \leq x \leq 0.5$, covering the full range of magnetic behaviour from ferromagnetic to spin glass, with five compositions in the two-transition region. These materials were studied using both bulk techniques (magnetization and susceptibility) and microscopic probes (Mössbauer spectroscopy and ZF-μSR). We found perfect agreement between the static and dynamic signatures of T_{xy} obtained from all techniques. There is no evidence for separate static and dynamic transitions below T_c. The phase diagram derived from our measurements is fully consistent with numerical simulations and the observed signatures of T_{xy} in this site frustrated material are identical to those observed previously in bond frustrated alloys.

Fitting procedure

Above T_c, fluctuations lead to an exponential dephasing of the muon polarization: $A_d = A_o \exp(-\lambda t)$ where λ is an effective relaxation rate. Below T_c, a static magnetic field will be present at the muon sites. However, the materials studied here are both structurally disordered (i.e. glassy) and magnetically disordered as a result of both random Mn substitution and also exchange frustration, therefore we expect a distribution of local fields to be present. In this case, the asymmetry will decay according to the Kubo-Toyabe (K-T) form:

$$G_z(\Delta, t) = \frac{1}{3} + \frac{2}{3}\left(1 - (\Delta t)^\alpha\right) \exp\left(-\frac{(\Delta t)^\alpha}{\alpha}\right)$$

with $\alpha = 2$, so that Δ/γ_μ is the rms field. In cases where both static order and fluctuations are present the asymmetry decays according to the product:

$$A = A_d \times G_z,$$

and both a K-T contribution at early times, and a slower exponential decay are seen. Note, we were able to fully fit all of our data using these functions, without resorting to the use of stretched exponentials.

Results

Fitting the μSR data using the functions described earlier yields the temperature dependences of the static relaxation rate (Δ), a measure of the static field seen by the muons, and the dynamic fluctuation rate (λ) which tracks the fluctuations in the field at the muon sites. These fits are summarized in Fig. 92 for four samples. The changeover from two transitions to one clearly occurs between $x = 0.30$ and $x = 0.325$, placing x_c in this range. Only a single transition is seen for the $x = 0.350$ sample as it is beyond x_c and is therefore a spin glass. The four samples $0.225 \leq x \leq 0.30$ each exhibit two distinct peaks in $\lambda(T)$. The higher temperature peak is associated with the onset of a non-zero static contribution and thus clearly corresponds to T_c, while the lower peak is aligned with the break in the slope of $\Delta(T)$ and therefore marks the freezing of the transverse spin components at T_{xy}. As the Mn content is reduced, the contribution of the transverse spin components to the total ordered moment declines, so that the increase in Δ below T_{xy} becomes difficult to localize reliably. Even with the high density of points apparent in Fig. 92, the error on T_{xy} at $x = 0.225$ is about 16 K, however, the derived value is fully consistent with the two dynamic determinations. At $x = 0.20$, only the fluctuation peak at T_{xy} was detected.

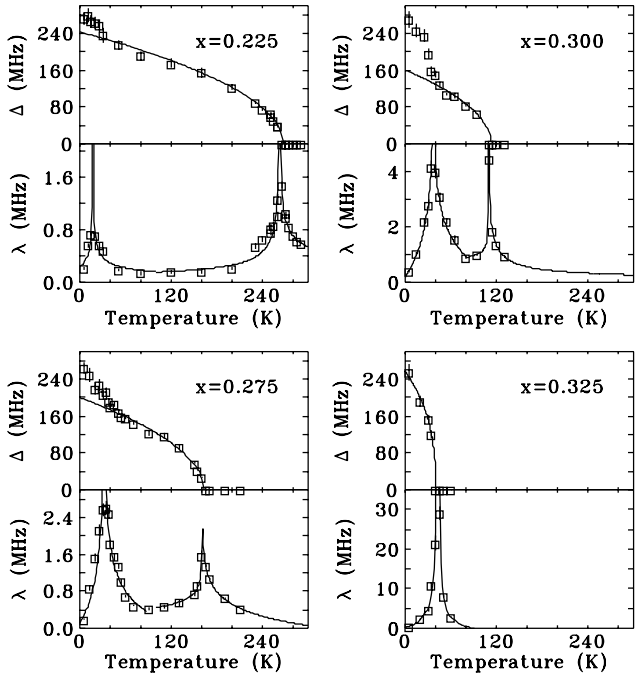

Fig. 92. Temperature dependence of the static (Δ) and dynamic (λ) signals from ZF-μSR for several a–$(Fe_{1-x}Mn_x)_{78}Si_8B_{14}$ alloys. In every case, the increase in static order (at T_c, T_{xy} or T_{sg}) is associated with a peak in the fluctuation rate.

The transition temperatures deduced from the ac-susceptibility data (χ' for T_c, χ'' for T_{xy}), $< B_{hf} > (T)$ from Mössbauer spectroscopy, and both Δ and λ from the ZF-μSR data are summarized in the phase diagram shown in Fig. 93. Manganese doping has a severe

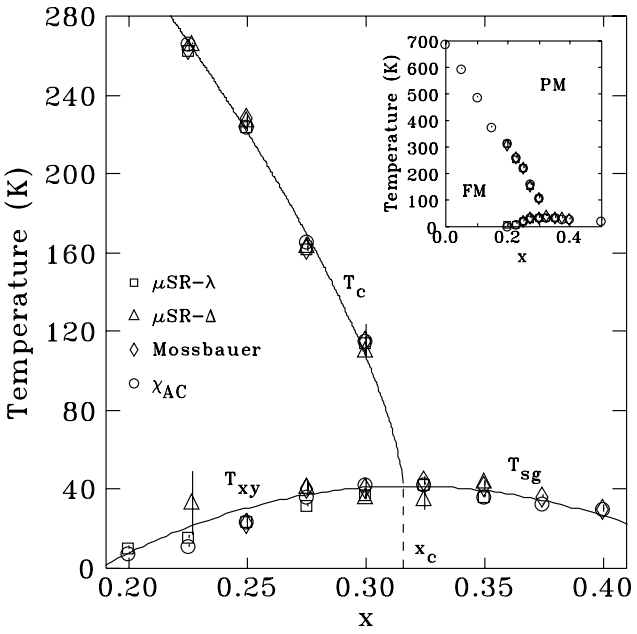

Fig. 93. Magnetic phase diagram for a–$(Fe_{1-x}Mn_x)_{78}Si_8B_{14}$ derived from ac-susceptibility data (χ' for T_c, χ'' for T_{xy}), $< B_{hf} > (T)$ from Mössbauer spectroscopy, and both Δ and λ from the ZF-μSR. Three transitions can be identified: ferromagnetic ordering at T_c, transverse spin freezing at T_{xy}, and spin glass ordering only for $x > x_c$ at T_{sg}. Note the perfect agreement between independent determinations of T_{xy}. Inset shows data for whole composition range studied.

effect on the magnetic ordering of this system, driving T_c down from 695 K at $x = 0$ (inset to Fig. 93), to ∼40 K at $x_c = 0.31$. A power-law does not fit the composition dependence of T_c particularly well, and extrapolating T_c to zero yields a rather poor estimate for the critical composition of $x_c = 0.33 \pm 0.02$. This failure is not unexpected, as the FM–SG boundary is not marked by $T_c \to 0$, but rather by $T_c \to T_{xy}$. Indeed, a power-law fit to $1 - T_{xy}/T_c$ is far superior, and yields $x_c = 0.309 \pm 0.004$, in perfect agreement with $x_c = 0.306 \pm 0.006$ derived from field-cooled magnetization data.

The excellent agreement between T_c values derived from χ', Mössbauer spectroscopy and ZF-μSR, coupled with consistent T_{sg} values obtained above x_c, provides strong evidence that the analysis and transition assignments are correct and self-consistent. However, it is the behaviour at T_{xy} that is the primary focus of this work. Only for $x \geq 0.2$ do we see a second transition below T_c, a result that is in full accord with numerical simulations [Nielsen *et al., op. cit.*]. There is excellent agreement between T_{xy} values derived from the various techniques. For $x = 0.275$ and 0.300, we have four independent determinations of T_{xy} that agree to better than 5 K. The static, dynamic and loss signatures of T_{xy} are in perfect agreement, with no systematic bias apparent in any of the measurements. While at $x = 0.250$, static data from Mössbauer, and dynamics from both $\lambda(T)$ and χ'' are in complete agreement. By $x = 0.225$, the change in the static order at T_{xy} is too small for its onset to be reliably determined from $< B_{hf} > (T)$ and the estimate from $\Delta(T)$ exhibits a substantial (∼50%) uncertainty. However, the ZF-μSR fluctuation peak, and the maximum in the χ'' loss signal are still clear and coincident. As was found in our earlier work on bond-frustrated alloys [Ryan *et al., op. cit.*], all observed signatures of T_{xy} line up perfectly.

It is important to emphasize that the techniques that have been used to determine T_{xy} with such good agreement probe a very wide range of frequencies: ZF-μSR–Δ (∼10^8 Hz), $< B_{hf} >$–Mössbauer (∼10^7 Hz), ZF-μSR–λ (∼10^6 Hz) and χ'' (∼10^2 Hz), yet they yield T_{xy} values that agree within a few K for five samples that exhibit transverse spin freezing transitions at temperatures that change by more than a factor of three. Furthermore, there is no systematic frequency related trend in the T_{xy} values for a given sample. The scatter is random. A separation of T_{xy} into distinct static (T_K) and dynamic (T_F) events can therefore be ruled out. There is no evidence in our data to support the existence of a third transition below T_{xy}.

Experiment 842
Mu-substituted free radicals in sub- and supercritical water
(P.W. Percival, SFU)

Experiment 842 and its predecessor, Expt. 713, were designed to study muonium chemistry under hydrothermal conditions, i.e. aqueous solutions at high temperatures and pressures. The motivation is to investigate the chemistry of reactive intermediates under the extreme conditions found in supercritical water reactors, used for the destruction of hazardous waste, and in the cooling water cycles of pressurized water nuclear reactors. Direct measurements of "pressure-cooker" chemistry are technically very demanding, and engineering studies have had to rely on extrapolation of lower temperature data. On the other hand we have demonstrated that muon spin rotation circumvents many of the limitations of conventional spectroscopic probes, and that it is therefore feasible to investigate muonium chemistry in such difficult environments. Since muonium behaves chemically as a light isotope of hydrogen it can be used to study H atom chemistry and the properties of free radicals which incorporate H (almost all organic free radicals).

Only one week of beam time was taken in 2002; it was used for measurements of muonium reaction rates. Two H abstraction reactions were investigated:

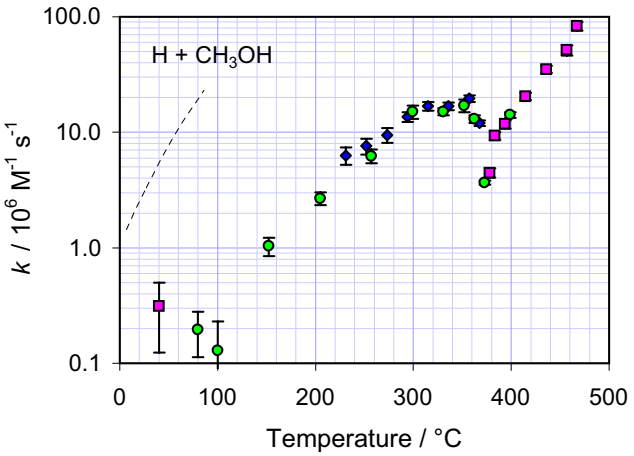

Fig. 94. Rate constants for Mu + methanol in water at 230 bar. The new data are denoted with square symbols. The dotted line indicates the best literature data for the equivalent reaction of H atoms.

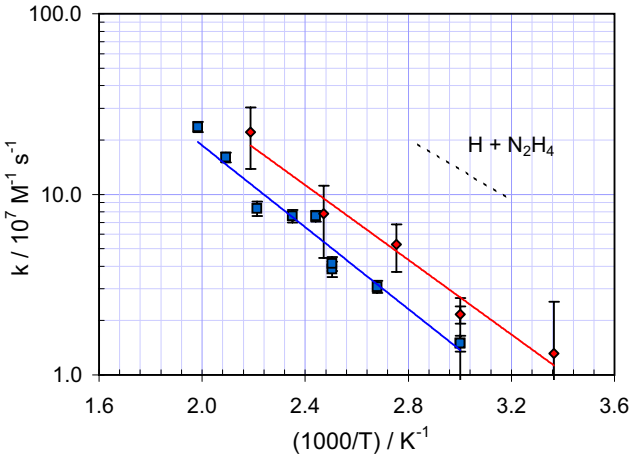

Fig. 95. Arrhenius plot of rate constants for Mu + hydrazine in water at pressures at or below 250 bar. The squares correspond to solutions at natural pH (mixture of N_2H_4 and $N_2H_5^+$) while the circles represent measurements on solutions at pH 1.5 (overwhelming $N_2H_5^+$).

1) Mu + $CH_3OH \longrightarrow$ MuH + $\cdot CH_2OH$ and
2) Mu + $NH_2NH_2 \longrightarrow$ MuH + $\cdot NHNH_2$.

We have already made extensive measurements of Mu kinetics for the reaction with methanol (TRIUMF Annual Report 2000) and some of the data have been published [Ghandi *et al.* (Physica B, in press)]. The new measurements extend the study to higher temperatures. Our earlier work for this and other reactions has shown that the rate constants go through a maximum as the temperature is raised, but we had very little data on either the "dip" or the "recovery" at higher temperatures. Since the dip occurs in the region of the critical point of water (374°C) the density is very sensitive to temperature and pressure. Precise control of the pressure is therefore essential to avoid huge systematic errors.

Figure 94 displays a selection of data at constant pressure (230 bar, except for a few points at lower temperature where the pressure effect is negligible). Also shown is the (very limited) range of published data for the H atom [Mezyk and Bartels, J. Phys. Chem. **101**, 1329 (1997)].

In addition to completing the study of Mu + methanol we began an investigation of the reaction with hydrazine (NH_2NH_2). Hydrazine is commonly used as a corrosion inhibitor in steam generators, including those in the nuclear power industry. Despite the obvious importance of understanding the radiation chemistry of water and additives, there are relatively little data on the reactions of radiolysis transients in aqueous solutions of hydrazine. Moreover, a recent study [Buxton and Sims, Phys. Chem. Chem. Phys. **2**, 4941 (2000)] calls into question published data on the reactions of H atoms with hydrazine. The situation is complicated by the existence of the hydrazinium ion ($N_2H_5^+$) in acidic solution, and the possibility of alternative reaction channels.

Our preliminary results for the muonium rate constant are displayed in Fig. 95. The activation energies derived from the slopes of the data sets at different pH are similar to the published result for H + N_2H_4 but not that for H + $N_2H_5^+$ [Mezyk *et al.*, J. Chem. Soc. Far. Trans. **92**, 2541 (1996)].

Experiment 843
Quadrupole ordering in dense Kondo systems studied by μLCR
(R. Kadono, J. Akimitsu, KEK-IMSS/Aoyama-Gakuin U.)

It has been reported by Young *et al.* that lightly doped divalent hexaboride $Ca_{1-x}La_xB_6$ shows a ferromagnetism [Young *et al.*, Nature **397**, 412 (1999)]. The ferromagnetic state has a number of unprecedented features, e.g., it appears only over a narrow carrier concentration range ($0 < x < 0.01$) with a small magnetic moment ($< 0.07\ \mu_B$/La) and a remarkably high Curie-temperature ($T_c \approx 600$ K). Various studies have been performed after this report to understand the mechanism of the ferromagnetism in this material. However, it turned out that this compound exhibits extremely strong sample dependence in bulk properties, and it is not clear whether or not impurities affect this ferromagnetic behaviour. Thus, there is no general consensus on the intrinsic character of ferromagnetism among researchers.

We have been studying this compound by μSR technique to elucidate the microscopic character of the reported ferromagnetism. We have found that the relaxation rate of CaB_6 is apparently larger than that

of CeB_6 in the paramagnetic phase over the low temperature region ($T < 150$ K). Since the contribution of nuclear dipolar field from boron nuclei is presumed to be the same between isostructural CaB_6 and CeB_6, the difference of relaxation rate for both systems suggests an additional contribution of magnetic moments in CaB_6.

In the 2002 beam time, we performed muon level-crossing resonance (μLCR) measurements to determine the electric field gradient q at the boron site in CaB_6. In the case of ^{11}B ($I = 3/2$), only one resonance signal is expected at a field,

$$B_{\rm res} \simeq \frac{3e^2qQ}{4\hbar\gamma_\mu}.$$

The time-integrated and field-differentiated asymmetry δA is shown in Fig. 96. The resonance signal is observed near 4 mT above 110 K, whereas it is shifted to near 7 mT below 110 K. It should be emphasized here that two resonance signals are clearly observed at the lowest temperature (4.5 K). These spectra can be described as

$$\delta A = \sum_{n=0}^{m} -c_n(B - B^n_{\rm res})\exp(-\gamma_\mu^2(B - B^n_{\rm res})^2/\Lambda^2) \left(\begin{array}{l} T < 110\,{\rm K} : m = 2 \\ T > 110\,{\rm K} : m = 1 \end{array} \right),$$

where c_n are the amplitudes determined by the relaxation rate, and Λ is the linewidth obtained from the second moment. The term of $n = 0$ corresponds to the zero-field crossing. The solid curves in Fig. 96 are the fitting results by the above equation, where we obtained the resonance fields ($B^n_{\rm res} : n = 1, 2$) as shown in Fig. 97. The resonance field above 110 K is in good agreement with those obtained from ^{11}B-NQR in the paramagnetic phase of CeB_6, thereby indicating that there is no muon-induced effect. On the other hand, however, there are two resonance fields below 110 K, being larger than that above 110 K. Since the change of a crystal structure in CaB_6 can not be observed around 110 K, two resonance peaks might be attributed to the change of electronic arrangement around boron atoms. Preparation of a more detailed report is now in progress.

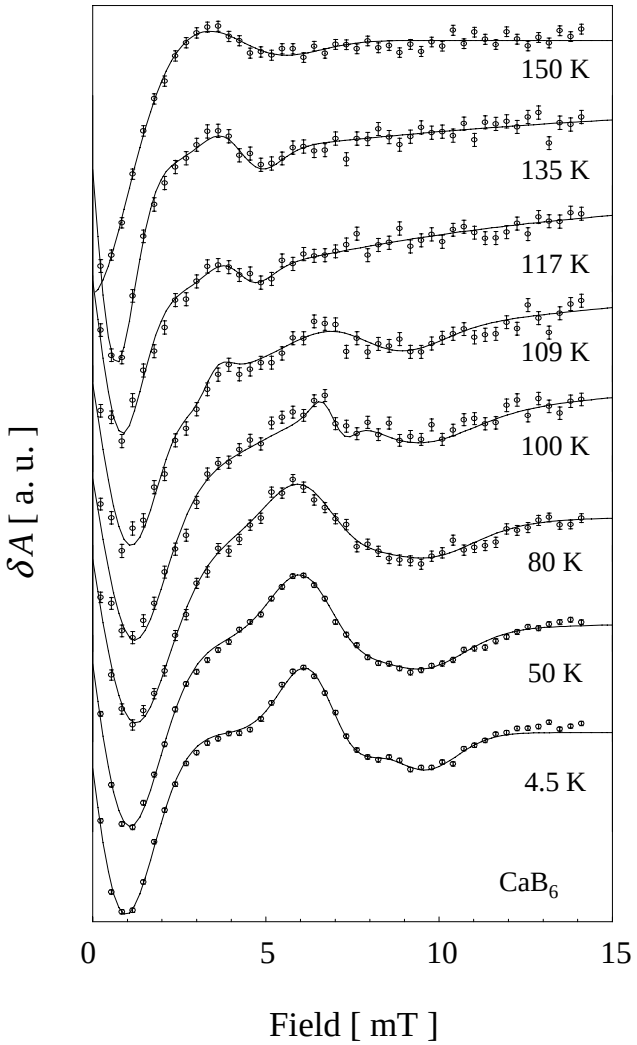

Fig. 96. Time-integrated μLCR spectra in CaB_6 at various temperatures. The solid curves are results of fitting by the function described in the text.

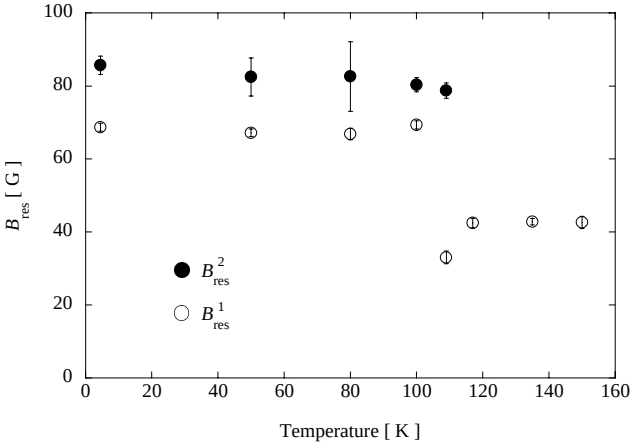

Fig. 97. Temperature dependence of muon level-crossing resonance field in CaB_6.

Experiment 846
Complex order parameter symmetry in $YBa_2Cu_3O_{7-\delta}$ at low T and high magnetic field
(J.H. Brewer, UBC; J.E. Sonier, SFU)

Superconductivity in $YBa_2Cu_3O_{7-\delta}$ depends both on the oxygen content, δ, as well as the oxygen ordering properties of the CuO chain layers. While early ZF-μSR measurements on underdoped polycrystalline samples displayed clear signatures of ordered and/or fluctuating Cu electronic magnetic moments, studies of

optimal and fully oxygenated samples showed sensitivity only to the static nuclear dipoles. More recent ZF-μSR measurements on high-quality superconducting single crystals showed that the muon-spin relaxation signal does in fact evolve considerably as a function of temperature at optimal doping, indicating the presence of an additional source of local magnetism [Sonier *et al.*, Science **292**, 1692 (2001)]. In order to gain more insight into the physical origin of the additional magnetism sensed by the μ^+, we carried out ZF-μSR experiments on a series of $YBa_2Cu_3O_{7-\delta}$ single crystals with different oxygen content. In 2002 we completed this study, and began work on the $Y_{1-x}Ca_xBa_2Cu_3O_{7-\delta}$ system. The substitution of Y^{2+} by Ca^{2+} introduces extra hole carriers into the superconducting CuO_2 layers. This allows for hole concentrations greater than that in fully-oxygenated $YBa_2Cu_3O_7$, thus enabling investigations of the overdoped regime over a wider range of hole doping.

Figure 98 shows measurements of the muon-spin relaxation rate in single crystals of Ca-doped $YBa_2Cu_3O_{6.99}$ at zero external field. Qualitatively the temperature dependence of the relaxation rate resembles that in the pure (nearly) fully-oxygenated compound $YBa_2Cu_3O_{6.99}$. In particular, a minimum near $T = 60$ K and a significant increase below $T = 35$ K are observed. We have previously attributed these features in the pure system $YBa_2Cu_3O_{7-\delta}$ to a redistribution of the hole carriers in response to local structural distortions. The observation of the same features in the Ca-doped sample supports our assertion that these structural changes occur at temperatures that are independent of hole concentration.

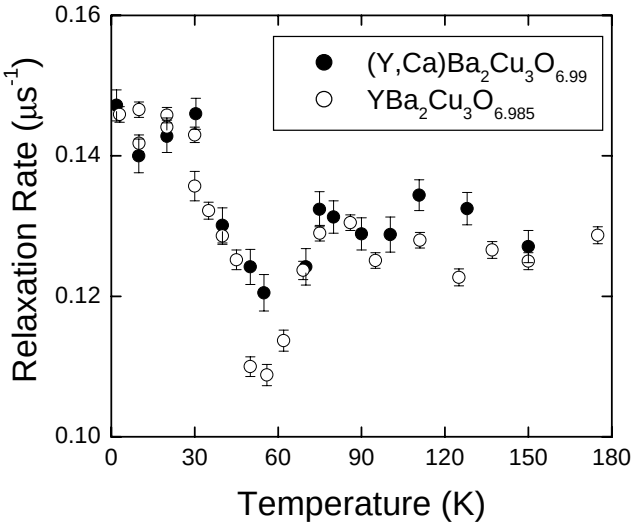

Fig. 98. Temperature dependence of the muon-spin relaxation rate measured at zero external field in Ca-doped and pure $YBa_2Cu_3O_{6.99}$ single crystals.

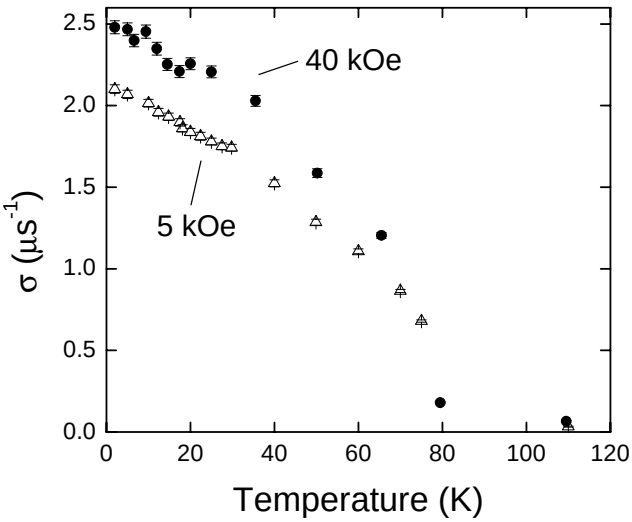

Fig. 99. Temperature dependence of the muon-spin depolarization rate in Ca-doped $YBa_2Cu_3O_{6.99}$ single crystals at $H = 5$ kOe and $H = 40$ kOe applied parallel to the c-axis of the crystals.

Figure 99 shows the temperature dependence of the muon-spin depolarization rate in Ca-doped $YBa_2Cu_3O_{6.99}$ single crystals in the vortex state. These results were obtained from a preliminary on-line analysis of the data. Both sets of data show the linear temperature dependence at low T that is characteristic of a "clean" d-wave superconductor. A detailed analysis of this data, assuming an appropriate theoretical field distribution for the vortex lattice, will ultimately lead to a precise determination of the temperature dependence of the in-plane magnetic penetration depth λ_{ab}.

Experiment 847
Electron-doped high-T_c superconductors
(J.E. Sonier, SFU)

While there now exists a large body of convincing experimental work on high-T_c superconductors with hole-type carriers, the intrinsic properties of the electron-doped cuprates $R_{2-x}Ce_xCuO_4$ ($R \equiv$ La, Pr, Nd, Sm or Eu) have remained very elusive. Part of the problem stems from the difficulty of preparing single phase superconducting samples. An additional complication is the presence of both Cu and rare-earth (R) moments. The interplay between these two magnetic sublattices has been studied extensively in the undoped parent compounds R_2CuO_4. In Ce-doped samples, there is the possibility that the magnetic exchange interactions involving the CuO_2 planes play an important role in superconductivity. There is also some uncertainty about the symmetry of the superconducting order parameter (i.e. s-wave, d-wave, p-wave etc.). In 2002 we continued our study of superconducting $Pr_{2-x}Ce_xCuO_4$ (PCCO) single crystals.

TF-μSR and magnetization measurements were carried out under both field-cooled (FC) and zero-field cooled (ZFC) conditions. Typical asymmetry spectra are shown in the inset of Fig. 100. In the ZFC case, pinning at the sample edges prevents flux from entering the bulk at $T = 2.3$ K and $H < 300$ Oe. Thus, the ZFC time spectrum in Fig. 100 resembles that observed in ZF. We note that this is also the case in high-quality $YBa_2Cu_3O_{7-\delta}$ single crystals. Above 300 Oe, flux fully penetrates the sample at $T = 2.3$ K, but pinning centres prevent the formation of an equilibrium vortex lattice configuration. On the other hand, a well-ordered vortex lattice is achieved in the FC procedure. Fast Fourier transforms (FFT) of the corresponding muon-spin precession signals at $H = 91$ Oe are shown in Fig. 100. The FFT provides an approximate picture of the internal magnetic field distribution $n(B)$. Above T_c, the linewidth is due to the electronic and nuclear magnetic moments. Below T_c, the lineshape is further broadened and becomes asymmetric as a result of the inhomogeneous field distribution created by a lattice of vortices.

Below T_c, there is a substantial increase of the average internal field B_0 at the μ^+ stopping site that nearly coincides with the increase of the diamagnetic signal observed in bulk susceptibility $\chi^{\parallel}$ measurements under FC conditions (see Fig. 101 inset). From μ^+ Knight shift measurements carried out in the normal state we have verified that this increase of B_0 cannot be explained by the formation of Cooper pairs. We surmise that the increased field at the μ^+ site is due to

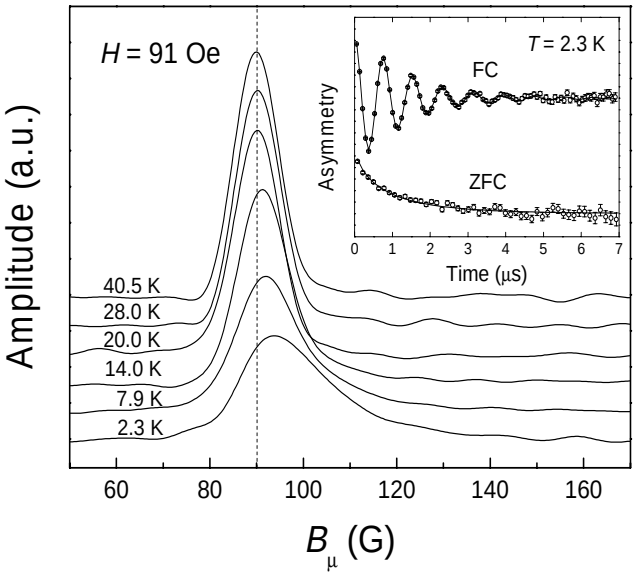

Fig. 100. Fourier transforms of the muon-spin precession signal in PCCO. Below T_c, the measurements were taken in an arbitrary sequence as a function of T under FC conditions. The dashed vertical line indicates the value of the external field $H = 91$ Oe. Inset: Asymmetry spectra taken at $T = 2.3$ K under both FC and ZFC conditions.

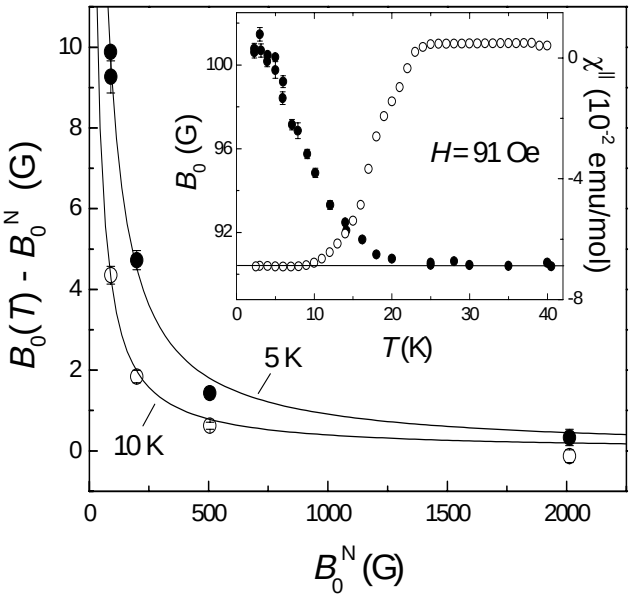

Fig. 101. $B_0(T) - B_0^{\rm N}$ vs. $B_0^{\rm N}$ at $T = 5$ K (solid circles) and 10 K (open circles). The solid curves are described in the text. Inset: Temperature dependence of B_0 and $\chi^{\parallel}$ taken under FC conditions.

supercurrents induced in the CuO_2 layers by the Pr $4f$-moments. The screening of R magnetic moments has previously been considered in the $RBa_2Cu_3O_{7-\delta}$ system, where TF-μSR measurements show large shifts of B_0 in the superconducting state. The main panel of Fig. 101 shows a plot of the difference between the value of B_0 below and above T_c. The solid curve is a fit assuming $B_0(T) = [(B_0^{\rm N})^2 + (B_\perp)^2]^{1/2}$, where $B_0^{\rm N}$ is the average internal field in the normal state and $B_\perp \approx 43$ G and 28 G, at 5 K and 10 K, respectively. This indicates that the additional field $B_\perp$ that appears at the μ^+-site is primarily directed in the ab-plane.

The in-plane magnetic penetration depth λ_{ab}, which is related to the density of superconducting carriers, was determined from an extensive analysis of the TF-μSR time spectra. The fits accounted for both the inhomogeneous field distribution associated with a vortex lattice and the local field distribution due to the nuclear and electronic magnetic moments. Figure 102 shows the temperature dependence of λ_{ab}^{-2}. The absence of data below $T = 2.3$ K forbids an accurate determination of the limiting temperature dependence of $\lambda_{ab}^{-2}(T)$. However, above this $\lambda_{ab}^{-2}(0)/\lambda_{ab}^{-2}(T)$ shows reasonable agreement with that determined by μSR in the hole-doped high-T_c systems $La_{2-x}Sr_xCuO_4$ and $YBa_2Cu_3O_{7-\delta}$. The zero-temperature value $\lambda_{ab}(0) \approx 3370$ Åsuggests our sample is primarily underdoped. Recently it has been suggested that there is a crossover from s-wave to d-wave behaviour in the underdoped regime of electron-doped cuprates. Our results could

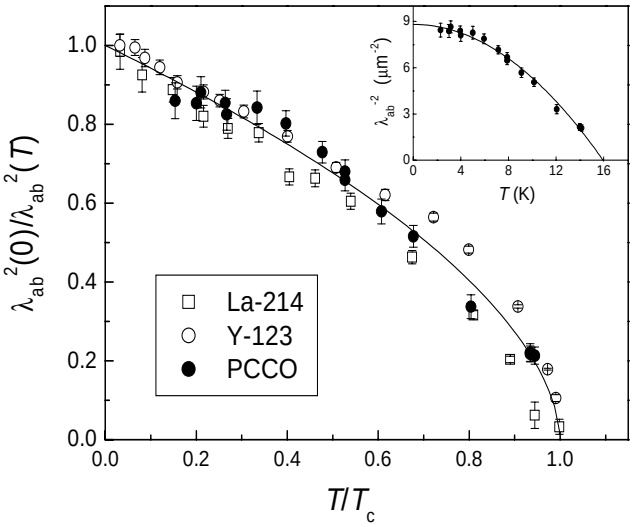

Fig. 102. Normalized magnetic penetration depth $\lambda_{ab}^2(0)\lambda_{ab}^2(T)$ as a function of T/T_c for single crystals of PCCO at $H = 90$ Oe (solid circles), $La_{2-x}Sr_xCuO_4$ at $H = 2$ kOe (open squares) and $YBa_2Cu_3O_{6.95}$ at $H = 5$ kOe. Inset: Temperature dependence of λ_{ab} in a PCCO single crystal.

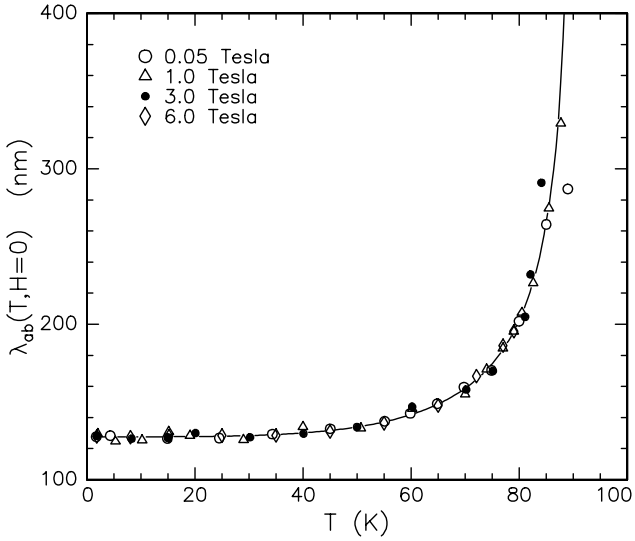

Fig. 103. The temperature dependence of the zero-field penetration depth, λ_{ab}(T, H=0), with the fitted effects of pinning removed. The curves are fitted with a London penetration depth value of λ_{ab}(T, H=0) = 127.6 ± 1.5 nm.

be interpreted as consistent with d-wave pairing in the presence of sample impurities. However, a unique determination of $\lambda_{ab}^{-2}(T)$ at low temperatures by μSR awaits the availability of larger high-quality single crystals.

Experiment 851
μSR in ruthenate and cuprate high-T_c compounds
(D.R. Harshman, Physikon Research Corp.)

Over the last year, our research program has focused on answering two basic questions regarding high-T_c superconductivity: (1) "What is the pairing state symmetry?", and (2) "Where does the hole condensate actually reside?" To this end, we have concentrated on measurements of $YBa_2Cu_3O_7$ and $Sr_2Y(Ru_{1-u}Cu_u)O_6$, respectively.

Proof of nodeless pairing state in single-crystal $YBa_2Cu_3O_7$

Muon spin rotation (μ^+SR) measurements were conducted on a single-crystal of $YBa_2Cu_3O_7$ with a superconducting transition temperature of $T_c \approx 91.3$ K and a transition width of $\Delta T_c < 0.5$ K in zero applied field. Data were taken at applied magnetic fields along the c-axis of 0.05, 1.0, 3.0, and 6.0 T. We found, by taking into account the expected field-dependent and temperature-activated flux-line disorder, that our results were in fact consistent with a nodeless (s-wave) superconducting order parameter and that they appeared to be inconsistent with order parameters possessing nodes, such as those having $d_{x^2-y^2}$ symmetry.

This result (shown in Fig. 103) is consistent with early μ^+SR measurements on sintered samples in which (we believe) strong pinning eliminated the temperature and field dependence of the vortex lattice disorder. These data (including their observed dependences on magnetic field) are, however, completely consistent with s-wave (or extended s-wave) pairing, provided that field-dependent and temperature-activated vortex de-pinning is also accounted for. Our results (i) confirm the s-wave superconductivity character originally observed in 1989, and (ii) show that the features of μ^+SR (and microwave) data claimed by other authors to be evidence for d-wave superconductivity are instead symptomatic of temperature-dependent depinning of vortices, which results in long-ranged distortion of the flux lattice. Indeed, the probability that any d-wave model gives a better fit than the two-fluid s-wave model is less than 4×10^{-6}.

Spin-glass behaviour, spin-fluctuations and superconductivity in $Sr_2Y(Ru_{1-u}Cu_u)O_6$

Muon spin rotation studies of $Sr_2Y(Ru_{1-u}Cu_u)O_6$ (for u = 0.1) reveal two distinct muon sites; one located in a SrO layer (which is superconducting at low temperatures) and the other in a $Y(Ru_{1-u}Cu_u)O_4$ layer (which is magnetically ordered at low temperatures). A precursor spin-glass state due to Ru moments is detected in high-fields (≈3.3 kOe) in the $Y(Ru_{1-u}Cu_u)O_4$ layers, with a spin-glass temperature, $T_G \approx 29.25$ K. The $Y(Ru_{1-u}Cu_u)O_4$ layers layers order ferromagnetically in the a-b planes at a Néel temperature, $T_N \approx 23$ K. This in-plane ferromagnetism alternates direction between adjacent $Y(Ru_{1-u}Cu_u)O_4$

planes, resulting in a net antiferromagnetic structure. Although the onset of superconductivity is observed both by electron spin resonance and by dc-susceptibility to occur for temperatures up to about $T_{c,onset} \approx 49$ K, this superconductivity is adversely affected by the Ru moments that fluctuate for $T > T_N$ producing magnetic fields that break pairs in the SrO layers. The muons, as well as other probes, sense the more-robust static superconductivity for $T < T_G$. In fact, resistance measurements only show zero resistance below T_N, at which temperatures the Ru moments that fluctuated for $T > T_N$ are frozen in-plane (resulting in a net zero field along the SrO layers). Hence, strictly speaking, the superconducting transition temperature is the same as T_N, which is far below $T_{c,onset}$. Below T_N there are no pair breaking fluctuating magnetic fields in the SrO layers where the hole condensate resides.

Experiment 877
μSR studies on strongly correlated electron systems under high pressure
(W. Higemoto, KEK-IMSS)

Pressure appears as an experimental parameter of primary interest in the field of strongly correlated electron physics. For the heavy fermion system (HF), volume reduction changes the strength of hybridization between conduction and f electrons and this in turn controls the behaviour of heavy-mass quasiparticles.

$CeRh_2Si_2$ shows two antiferromagnetic long-range ordering at ambient pressure (T_{N1} = 36 K and T_{N2} = 27 K). Magnetic Bragg peaks for $T_{N2} < T < T_{N1}$ were indexed to a $(\frac{1}{2}\frac{1}{2}0)$ magnetic structure; whereas below T_{N1} additional peaks corresponding to $(\frac{1}{2}\frac{1}{2}\frac{1}{2})$ appeared. Application of pressure suppresses T_N to 0 K at $P_c \sim 1$ GPa. Neutron diffraction study under high pressure shows decreasing of the saturated sublattice moment μ and transition temperature with increasing pressure [Kawarazaki *et al.*, Phys. Rev. **B61**, 4167 (2000)]. They found that μ becomes $\mu \sim 0$ at quantum critical point P_c. We study the magnetism of $CeRh_2Si_2$ by means of μSR method under high pressures. A high pressure μSR experiment was carried out at the M9B beam channel at TRIUMF. A piston cylinder type high pressure cell, which is made from CuBe alloy, was used. A positive muon of 102 MeV/c was implanted into a single crystalline sample of $CeRh_2Si_2$ through a thick wall of high pressure cell.

Figure 104 shows the typical μSR spectra in $CeRh_2Si_2$ under zero magnetic field (ZF) in the high pressure cell. Here about 40% of the implanted muons stopped at $CeRh_2Si_2$ and the rest of the muons stopped at the CuBe wall or the pressure medium (Fluorinert FC77/70). In $T_{N2} < T < T_{N1}$, no spontaneous muon

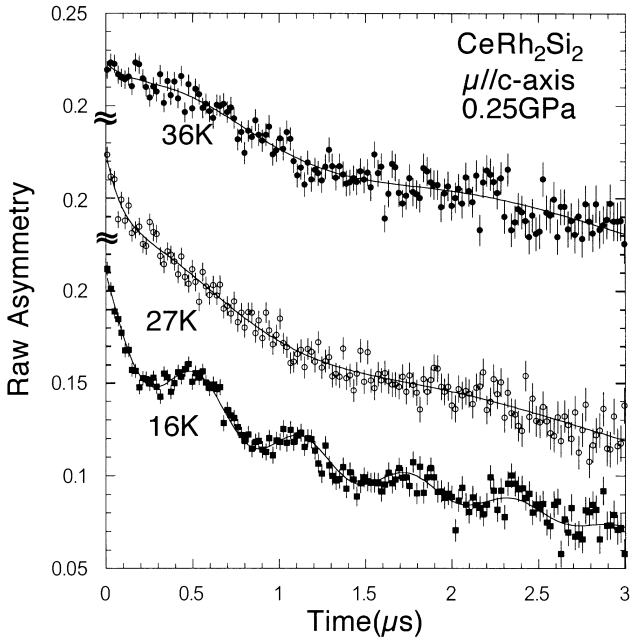

Fig. 104. ZF-μSR spectra in $CeRh_2Si_2$ at 0.25 GPa.

spin precession, but the fast spin relaxation is observed. In the lower magnetic ordering phase, $T < T_{N2}$, we observed both the fast relaxation and the spontaneous muon spin precession under ZF, which means that two kinds of the local fields exist at the muon site. The transition temperatures T_{N1} and T_{N2} decrease with increasing pressure. These behaviours are in good agreement with other experiments.

The precession frequency is almost temperature independent below T_{N2}, which shows the feature of the first order phase transition at T_{N2}. The pressure dependence of precession frequency below 10 K is plotted in Fig. 105. The precession frequency is nearly independent to the applied pressure up to 0.45 GPa. This result implies that the internal field and the saturated

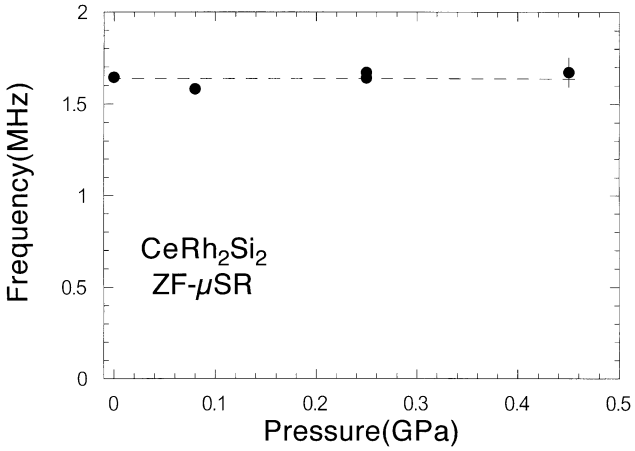

Fig. 105. Pressure dependence of ZF muon spin precession frequency below 9 K.

sublattice magnetic moment around the muon site are nearly independent to the applied pressure. It was proposed, based on the assumption of 4-**q** spin structure, that the saturated sublattice magnetic moment decreases with increasing pressure and disappears around 1 GPa [Kawarazaki *et al., op. cit.*]. These interpretations are inconsistent with each other. This fact implies that it is necessary to re-examine the magnetic structure below T_{N2}.

Experiment 881
Magnetism of Ce-based heavy fermion superconductor
(A. Koda, R. Kadono, KEK)

It is of principal interest whether or not magnetism coexists with superconductivity. Heavy fermion superconductors provide important opportunities to investigate the interplay between magnetism and superconductivity. $CeCu_2Si_2$ is an archetypal heavy fermion superconductor, which exhibits a magnetic phase (A-phase) adjacent to the superconducting phase as well. We have performed the muon spin rotation measurements of $Ce_{0.99}Cu_{2.02}Si_2$ under high transverse fields ($B_{\rm TF} \leq 3$ T), proving coexistence of the A-phase and the superconductivity in a microscopic level.

The chemical composition of the employed specimen is situated in the region where the dominance of the magnetic A-phase is observed. The hyperfine coupling (HFC) constant of muon spin has turned out to be -3.36 kOe/μ_B from a Knight shift vs. susceptibility plot at high temperatures ($T > 15$ K), which is comparable to the values reported on Cu and Si nuclei.

Below 15 K, on the other hand, the obtained TF-μSR signal exhibits a splitting with different HFC. We consider that this behaviour is attributed to the anisotropy of HFC, since a qualitatively similar anisotropy has been observed in Cu-/Si-NMR experiments [Ohama *et* al., J. Phys. Soc. Jpn. **64**, 2628 (1995)]. In addition, extrapolation from higher temperatures approximately divides the result at lower temperatures into a ratio of 1:2 as expected, because the isotropic Knight shift $K_{\rm iso}$ is given by $K_{\rm iso} = \frac{2}{3}K_\perp + \frac{1}{3}K_\parallel$, where $K_\perp$ ($K_\parallel$) is the Knight shift for the field perpendicular (parallel) to the c-axis. It is noteworthy that these μSR signals come from a unique domain in the sample.

In Fig. 106, the temperature dependences of $K_\parallel$ and the transverse depolarization rate ${T_2}^{-1}$ under several fields are shown. With decreasing temperature, ${T_2}^{-1}$ shows a pronounced increase below $\sim$0.8 K. Since this temperature dependence well reproduces previous ZF-/LF-μSR results, we consider that the increasing of the depolarization rate is due to the onset of the A-phase. A remarkable finding is that the central

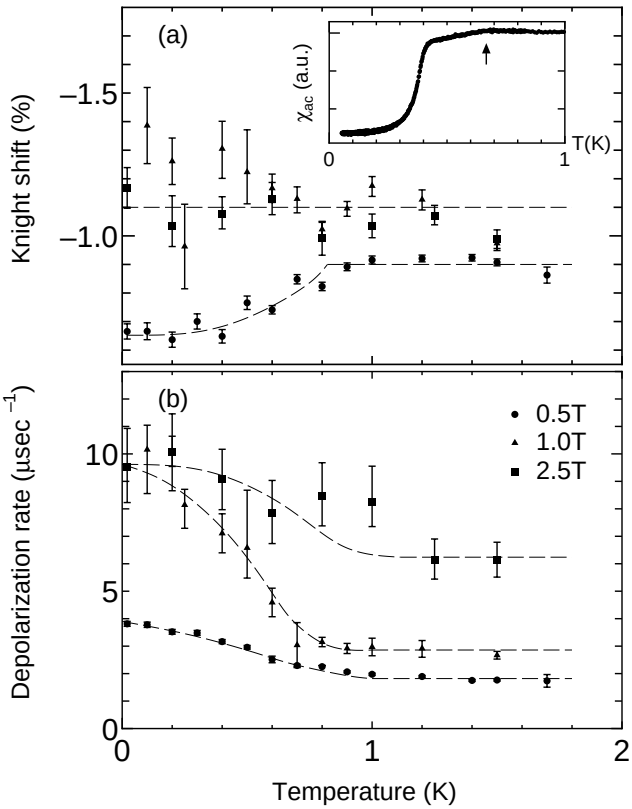

Fig. 106. Temperature dependences of the Knight shift parallel to the c-axis, $K_\parallel$, (a), and the transverse depolarization rate, ${T_2}^{-1}$, (b), at several magnetic fields. The broken lines are guides to the eye. In the inset of the upper panel, the ac-susceptibility of the present specimen is shown.

frequency of the broadening spectra is slightly shifted under the field of 0.5 T at lower temperatures, as shown in Fig. 106. The reduction of the Knight shift coincides with the appearance of the A-phase and is quenched by applying further high fields ($B_{\rm TF} \geq 1.0$ T). It is reasonable to interpret this field dependence as the suppression of superconductivity when $B_{\rm TF} \geq B_{c2}$. In summary, we have found evidence that superconductivity may exist within the magnetic A-phase in $CeCu_2Si_2$.

Experiment 883
Muoniated methyl and associated free radicals
(P.W. Percival, SFU)

In view of our successful detection in 2001 of the muoniated methyl radical, $\cdot CH_2Mu$, we had expected to study isotopomers such as $\cdot CD_2Mu$ in 2002. As it happens we used both weeks of beam time on some of the "associated free radicals" of the project title. These radicals are characterized as α-muoniated, because the Mu atom is directly bound to the radical centre, i.e. the atom which is the principal site of unpaired spin density in the molecule. Common methods for producing muoniated radicals involve addition of

Mu to a double bond (C=C, C=O) or aromatic ring, resulting in attachment of Mu to the radical centre or conjugated system. The methyl radical is the simplest α-muoniated organic radical, and we detected it as a product of the reaction between muonium and ketene ($CH_2C{=}O$). As part of the preliminary investigations for Expt. 883 we explored various other methods of generating α-muoniated radicals [McKenzie *et al.*, Physica B, in press]. One of these is the direct addition of Mu to a carbene:

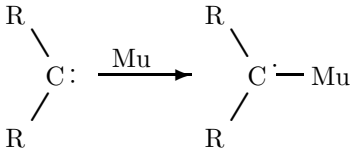

The relationship of such radicals to methyl is obvious when one replaces the alkyl groups (R) with H atoms.

Carbenes are relatively exotic species in chemistry. They possess a neutral dicoordinate carbon atom with a lone pair of electrons, so they are generally extremely reactive and are usually only postulated as reaction intermediates. However, over the past decade the synthesis and isolation of several singlet carbenes have been accomplished. A preliminary exploration with a commercially available carbene (**1** = 1,3,4-triphenyl-4,5-dihydro-1*H*-1,2,4-triazol-5-ylidene studied as a 0.25 M solution in tetrahydrofuran) gave encouraging results: A single pair of radical precession frequencies was detected by transverse field μSR, indicating that only one type of radical is formed, and this was tentatively assigned as radical **1a** (Fig. 107).

This result was very significant, since it represents the first example of radical formation by direct H (Mu) addition to a carbene. In fact, the addition of a hydrogen atom to a dicoordinate carbon constitutes one of the most fundamental addition reactions in chemistry – involving the creation of only one new chemical bond. The study of radicals formed from carbenes may permit the exploration of fundamental questions concerned with bond formation, such as: 1) How does the electronic structure of the reaction site change when the singlet carbene (sp^2 hybridized?) is converted into a doublet state? 2) Does the previously empty π-orbital accommodate the extra electron, or does the singly-occupied molecular orbital have more sp^3 character? The unpaired spin distribution in the radical and the geometry at the radical centre may provide valuable clues.

To investigate further we embarked on a collaboration with Dr. Jason Clyburne of the SFU Chemistry Department, who has considerable expertise and interest in carbene chemistry. The first step in the investigation was to confirm that Mu addition occurs at the carbene centre rather than elsewhere in the molecule. To

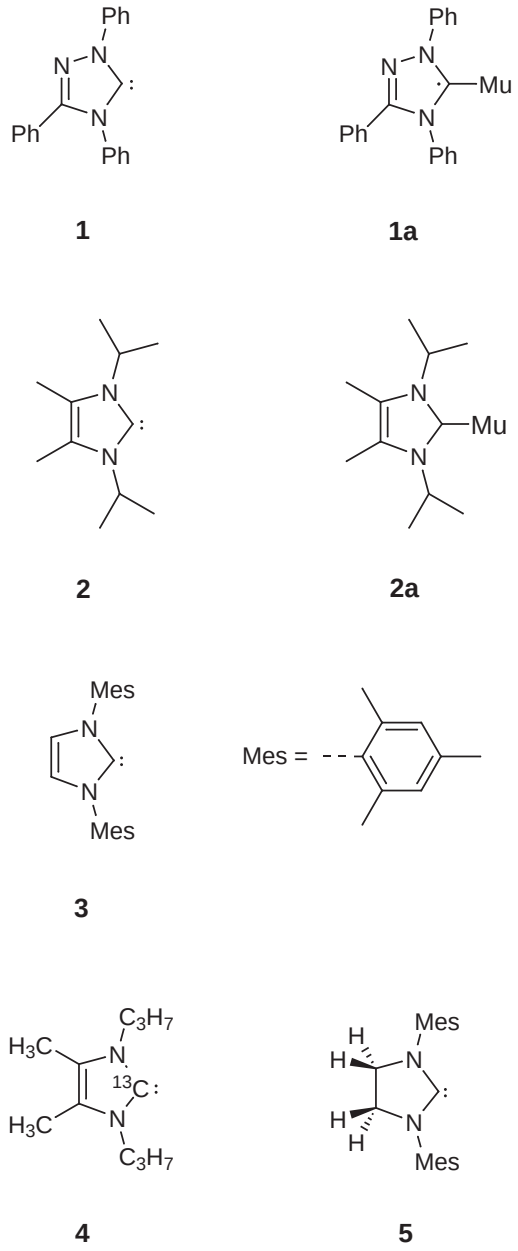

Fig. 107. The structures of carbenes (**1**–**5**) and some typical radical products (**1a**, **2a**) formed by Mu addition.

minimize the possible products, symmetrical carbenes are needed, so carbenes **2** and **3** were synthesized.

There are two obvious sites of Mu addition – at the carbene and alkene carbons (see Fig. 108).

Computational studies indicate that addition of hydrogen atoms to either site is exothermic, but addition to the carbene carbon is favoured (i.e. it gives the less energetic radical product).

Muon irradiation of **2** was found to produce only one type of radical. The muon hyperfine constant (hfc) was determined by TF-μSR (Fig. 109) and found to be 246.43 ± 0.02 MHz. One resonance was observed in

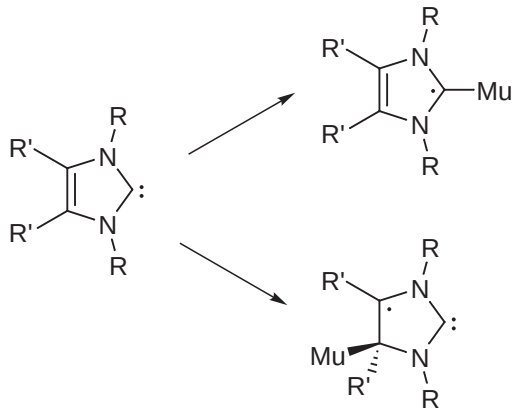

Fig. 108. Possible reactions of stable imidazole-type carbenes with muonium.

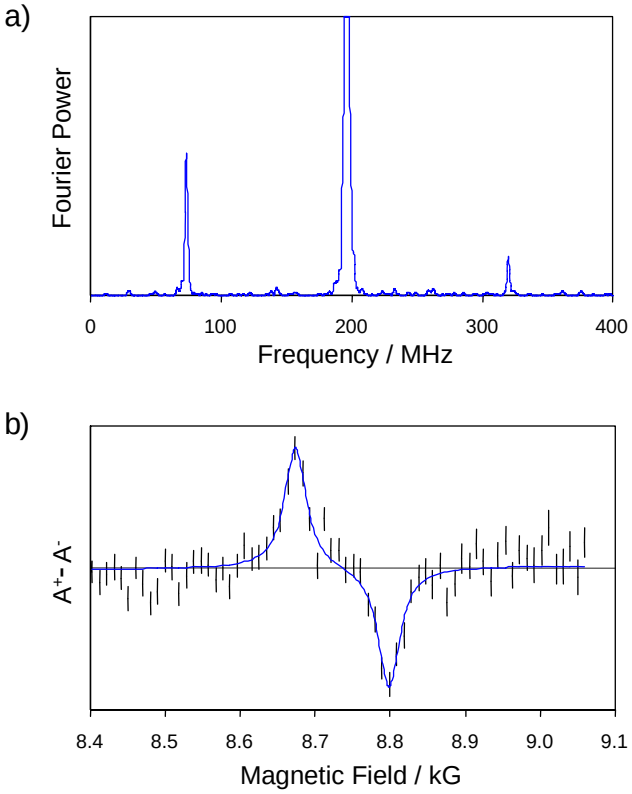

Fig. 109. (a) TF-μSR, and (b) μLCR spectrum of **2** in tetrahydrofuran at 298 K.

the μLCR spectrum at 8736.44 ± 1.24 G corresponding to either ^{14}N nuclei with hfc $A_N = 13.73 \pm 0.04$ MHz or protons with $A_p = 82.88 \pm 0.03$ MHz. Similar experiments were carried out with carbene **3**. The results for both carbenes are in good agreement with the predictions of density functional calculations, and we conclude that Mu adds exclusively to the carbene centre.

Two new avenues were explored in a second week of beam time. First, a ^{13}C-enriched version of carbene **2** was synthesized and investigated. The molecule was labelled at the carbene carbon (structure **4** in Fig. 107) to provide a clear signature of spin localization at this centre. Synthesis difficulties resulted in an enrichment of only 40%. In addition, the μLCR signal is predicted to be relatively weak, so it was a time-consuming exercise to locate the resonance and record it with adequate signal-to-noise. Nevertheless, this was achieved and the ^{13}C hfc was determined.

Second, a sample of a saturated imidazolylidene (**5**, the dihydro derivative of **3**) was obtained and investigated, the idea being to remove the possibility of Mu addition at the alkene site. The TF-μSR spectrum revealed a single radical but with a much smaller muon hfc than for **2** and **3**. This was unexpected and clearly merits further investigation. One possible explanation is that the Mu adduct of the saturated carbene has a more planar geometry at the radical centre. We plan to investigate this through measurements of the temperature dependence of muon and ^{13}C hfcs. However, such studies extend beyond the original scope of Expt. 883, and accordingly we have launched a new proposal, Expt. 945, which was approved by the Experiments Evaluation Committee in December, 2002.

The research carried out in Expt. 883 will form the major part of the Ph.D. thesis of Iain McKenzie (Chemistry Department, SFU).

Experiment 888
Test of delayed-muonium model for hydrocarbon liquids
(D.C. Walker, UBC)

These experiments were designed to test directly whether the "delayed" muonium-formation mechanism of low temperature inert materials [eg. Storchak *et al.*, Phys. Rev. Lett. **76**, 2969 (1996); Morris, Ph.D. thesis, University of B.C. (1997)] also applies to common chemicals like water, alcohols and hydrocarbons at room temperature. This possibility acquired extra importance for the Muonium Chemistry community when a theoretical model [Siebbeles *et al.*, J. Chem. Phys. **111**, 7493 (1999); Siebbeles *et al.*, Physica **B289-290**, 404 (2000)] was able to simulate the yields of muonium atoms (and their "complementary" diamagnetic species, D) in liquid hexane [Ito *et al.*, Can. J. Chem. **58**, 2395 (1980); Ito *et al.*, Hyp. Int. **8**, 355 (1981)] based on this delayed formation mechanism. In this model, the muonium atoms are predicted to be formed ~60 nm beyond the end of the muon's radiation-track and to take microseconds to form [Siebbeles *et al., op. cit.*]. This picture is a time-dilation of the old "spur" model [Percival *et al.*, Advances in Chemistry Series **175**, 335 (1979)] and both are in direct conflict with the even older hot model of muonium formation [Fleming *et al.*, Advances in Chemistry Series **175**, 279 (1979);

Walker, Muon and Muonium Chemistry (Cambridge University Press, 1983)], where the latter is based on reactions occurring at the pre-thermalization stage.

In both the delayed and spur models it is presumed that the positive muons survive as unattached μ^+ particles from the charge-exchange cycles of thermalization. Some of them form muonium atoms (Mu, μ^+e^-) later by combining with an electron produced in the muon's radiolysis track in the simple thermal neutralization reaction (1):

$$\mu^+ + e^- \rightarrow \mathrm{Mu}\,. \qquad (1)$$

Muons which do not undergo reaction (1) constitute the "diamagnetic" species, D. Mu formation is predicted to occur close to where the muon comes to rest, with the distance being within a nanometer or two of the muon's last track-ionization (i.e. very close to the last spur) in the spur model [Percival *et al., op. cit.*], and about 60 nm beyond that for the delayed model [Siebbeles *et al., op. cit.*]. As the electrons will not be distributed randomly around the muons in either case, nonhomogeneous kinetics will apply to reaction (1) giving a range of formation times. In these experiments solutes were added to scavenge e^- and μ^+ under pseudo-first order conditions. If reaction (1) occurred then the solutes would reduce the yield of Mu and increase that of D.

These were muon spin rotation studies using the SFUMU cart with backward muons on the M9B beamline and supported through the μSR Facility. About one hundred samples of pure liquids and solutions of selected solutes in these liquids were studied during the one week of beam time available. The samples were all deoxygenated and contained in 50 mL glass vessels. They were subjected to the usual on-line μSR fitting analysis [Percival *et al., op. cit.*; Fleming *et al., op. cit.*] to evaluate the initial asymmetry A (proportional to yield), the initial phase ϕ and the relaxation constants, for both Mu (M) and D. Muonium atoms were found to have lifetimes >1 μs in our hexane (and methanol and water) so Mu is directly observable, as shown in Fig. 110(a) for n-hexane (C_6H_{14}). To this hexane, a variety of solutes were then added which are known to scavenge electrons with rate constants in the 10^{12} $M^{-1}s^{-1}$ range (CCl_4, nitrobenzene, benzophenone, styrene, tempo and oxygen) or proton (μ^+) scavengers (methanol and triethylamine).

Our initial experiments used solutes at concentrations that targeted the delayed model – they used millimolar concentrations to reduce the electron lifetimes to $<10^{-7}$s. These results are indicated in Fig. 110 (same initial yield with or without CCl_4) and in Tables VIII and IX, where the fitted initial phases of Mu and D are seen to be unaffected by added scavengers of both e^- and μ^+. This shows clearly that Mu is not formed to any significant extent on the microsecond timescale by reaction (1).

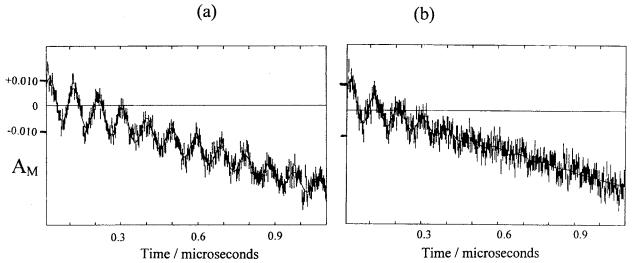

Fig. 110. (a) Plot of the TF-μSR muonium asymmetry (A_M) over the first μs in neat n-hexane at room temperature (293 ± 5 K) with an applied transverse magnetic field of 7.5 G. (b) Analogous plot to that in (a) except the hexane contains CCl_4 at a concentration of 0.0044 M (which reduces the electron lifetime to $\sim 10^{-10}$ s). The initial yield of Mu is seen to be the same, only the relaxation has changed.

Table VIII. Values of the initial phase of Mu (ϕ_M) recorded for experiments in neat hexane and various solutions of electron scavengers, in fields of 7.5 G at room temperature with diagonally opposite counters called UP and DOWN.

System	ϕ_M (DOWN)	ϕ_M (UP)
neat hexane (Fig. 110a)	265.32 ± 3.88	67.13 ± 4.74
neat hexane	266.30 ± 3.65	81.66 ± 4.52
neat hexane	272.48 ± 3.54	75.38 ± 4.48
CCl_4 in hexane (Fig. 110b)	270.94 ± 5.80	—
0.15 mM NitroB in hexane	262.11 ± 5.25	81.81 ± 6.83
0.30 mM NitroB in hexane	269.18 ± 6.11	71.77 ± 8.56
0.09 mM NitroB in hexane	254.70 ± 5.33	80.15 ± 8.03
21 μM Tempo in hexane	264.13 ± 5.00	79.38 ± 5.00
30 μM Tempo in hexane	265.79 ± 4.12	72.44 ± 5.60
46 μM Tempo in hexane	272.89 ± 5.45	81.89 ± 6.01

Table IX. Values of the initial phase of D (ϕ_D) recorded for experiments in neat hexane and solutions of electron and muon scavengers, in fields of 91 G at room temperature.

System	ϕ_D (DOWN)	ϕ_D (UP)
neat hexane (Fig. 111a)	87.75 ± 0.40	278.15 ± 0.44
neat hexane	88.35 ± 0.58	279.96 ± 0.68
Fig. 111b solution	89.18 ± 0.39	279.66 ± 0.45
0.5 M Methanol in hexane	87.17 ± 0.41	278.24 ± 0.47
Oxygen in hexane	86.15 ± 0.38	277.40 ± 0.44
0.2 M (NitroB + TEA) in hexane	89.15 ± 0.41	280.33 ± 0.48
0.2 M NitroB in hexane	88.23 ± 0.54	280.73 ± 0.64
0.1 M Benzophenone in hexane	87.60 ± 0.36	279.56 ± 0.42
0.2 M Triethylamine in hexane	87.55 ± 0.44	278.98 ± 0.50

The experiments were thus extended to much higher concentrations of scavengers to cover the nanosecond timescale corresponding to the spur model. Those results are represented by Fig. 111 (same initial

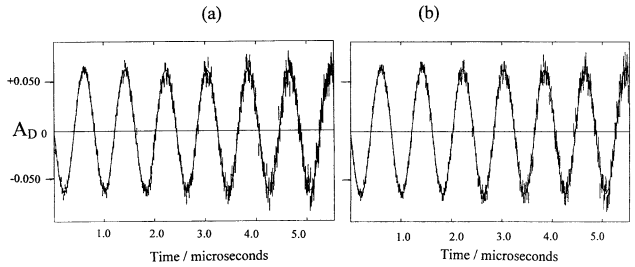

Fig. 111. (a) Plot of the TF-μSR diamagnetic asymmetry (A_D) against time over 5 μs for neat n-hexane at room temperature (293 ± 5 K) with a transverse magnetic field of 91 G. (b) Analogous plot to (a) except the hexane contains 0.49 M methanol + 0.087 M styrene (which essentially eliminates both e^- and μ^+). The initial yield of D is seen to be the same and no relaxation is observable.

yield and no decay, with or without e^- and μ^+ scavengers) and in Table X as the yields are unaffected by added scavengers in methanol and hexane. D was not measurably affected by the inhibition of reaction (1), so we deduce that Mu is not formed by that mechanism. (Mu itself could not be directly observed in those systems as all powerful electron scavengers react with Mu to some extent, as seen in Fig. 110(b) for 4.4 mM CCl_4.)

Having eliminated the delayed and spur models one is left with the hot model, the only model proposed so far whose precursor ($Mu_{(hot)}$) is not scavengable on the 10^{-11}s timescale. The hot model thus wins by default – at least in these chemical-active media at room temperature.

Unfortunately, similar scavenging experiments would be very difficult to do in the low temperature inert liquids or solids where electric field effects have shown reaction (1) to occur [Storchak *et al., op. cit.*]. But these are such inert systems that μ^+ and Mu have no other chemical reaction channels available, which is not the case in hexane, methanol or water.

Table X. Yields of D(P_D = 0.62 $A_D/A_{(water)}$) obtained in various solutions of hexane with electron or muon scavengers.

Solution	P_D
n-hexane	0.61
+ nitrobenzene (0.2 M)	0.59
+ benzophenone (0.1 M)	0.60
+ CCl_4 (4 mM)	0.60
+ oxygen (8 mM)	0.60
+ $N(C_2H_5)_3$ (0.2 M)	0.60
+ methanol (0.5 M)	0.61
+ $N(C_2H_5)_3$ (0.2 M) + nitrobenzene (0.2 M)	0.60
+ methanol (0.5 M) + styrene (0.1 M)	0.61

Experiment 891
Superconductivity and magnetism in $Ce_nM_mIn_{3n+2m}$
(G.D. Morris, LANL)

Experiment 891 is investigating superconductivity and magnetism in Ce-based heavy-fermion materials $Ce_nM_mIn_{3n+2m}$, M=Rh, Ir, Co. These materials exhibit a wide range of complex magnetic order and superconductivity which may be tuned with composition. The family of materials enables a systematic study of the relation between magnetism and unconventional superconductivity. Recently, our μSR experiments showed that antiferromagnetic order in $CeRh_{0.5}Ir_{0.5}In_5$ coexists microscopically with superconductivity [Morris *et al.*, Physica B, in press].

In 2002 we studied magnetic properties in several $n = 2$, $m = 1$ samples. Antiferromagnetic order is known from neutron scattering experiments to be present in Ce_2RhIn_8. Specific heat data show that T_N decreases on substitution of Rh with Ir and hint at the possibility of a quantum critical point (QCP) where T_N seems to approach zero temperature for the M=Ir material. Using μSR as a sensitive local probe of magnetism, we carried out experiments on several samples to follow the development of electronic magnetic moments with varying composition in the vicinity of this proposed QCP.

Representative muon relaxation spectra recorded in Ce_2IrIn_8 are shown in Fig. 112. Samples with Ir substituted with 5% Co or 5 and 10% Rh displayed qualitatively the same behaviour. At temperatures of about 1 K and above, the muon spin relaxation function follows a Gaussian Kubo-Toyabe form characteristic of isotropic nuclear dipolar fields. On cooling, an additional relaxation mechanism is apparent as an increase in spin depolarization rate. No coherent

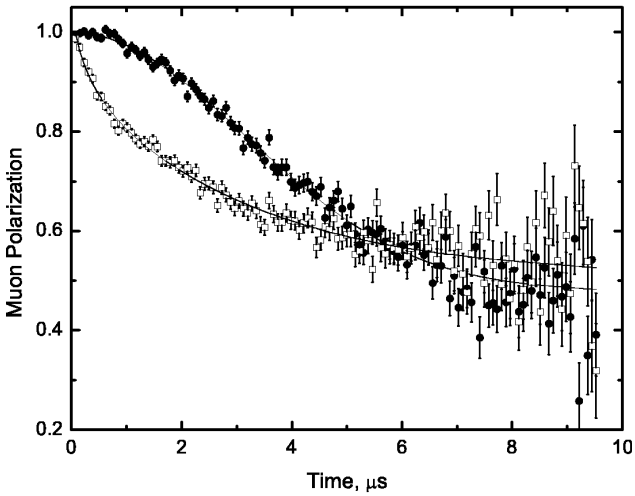

Fig. 112. Muon spin polarization functions in Ce_2IrIn_8 at T = 1.0 (circles) and 0.022 K (squares).

precession signal indicative of ordered magnetism was found; the muons see only randomly oriented magnetic fields. Assuming the nuclear dipolar broadening to be T-independent, the zero-field muon relaxation spectra were fitted with a polarization defined in terms of a product of Kubo-Toyabe functions

$$G(t) = \left[\frac{1}{3} + \frac{2}{3}(1-\Delta_{\rm n}^2 t^2)\exp(-\Delta_{\rm n}^2 t^2/2)\right] \times \left[\frac{1}{3} + \frac{2}{3}(1-\Delta_{\rm el}^p t^p)\exp(-\Delta_{\rm el}^p t^p/p)\right]$$

where the widths due to nuclear dipolar and electronic magnetic moments are characterized by $\Delta_{\rm n}$ and $\Delta_{\rm el}$ respectively. (A non-relaxing background signal was also present in this dilution refrigerator data.) $\Delta_{\rm n}$ for each sample was obtained from high temperature data and these values were held constant in fitting the low temperature spectra. The exponent p was found to be 0.6–0.7 in all samples. Figure 113 shows the temperature dependences of $\Delta_{\rm el}$. In all samples $\Delta_{\rm el}$ is not large; the additional local magnetic field is comparable to nuclear dipolar fields, implying the electronic moments are small. High transverse field data in Ce_2IrIn_8 also revealed two lines and hence two muon sites with different Knight shifts. The anomolous value of p may therefore result from characterizing the sum of two signals (resulting from Lorentzian field distributions with differing values of $\Delta_{\rm el}$) with one signal. Nevertheless, this phenomenological fitting model accomplishes the goal of extracting a measure of the additional line broadening from electronic magnetic moments and identifies their onset temperatures. Electronic magnetic moments appear at about 700 mK in all four samples, however, the widths $\Delta_{\rm el}(T=0)$ do vary with composition. These widths are highest for the $Ce_2Ir_{0.95}Co_{0.05}In_8$ sample and decrease by a factor of 2 across the series to the smallest value in $Ce_2Ir_{0.90}Rh_{0.10}In_8$.

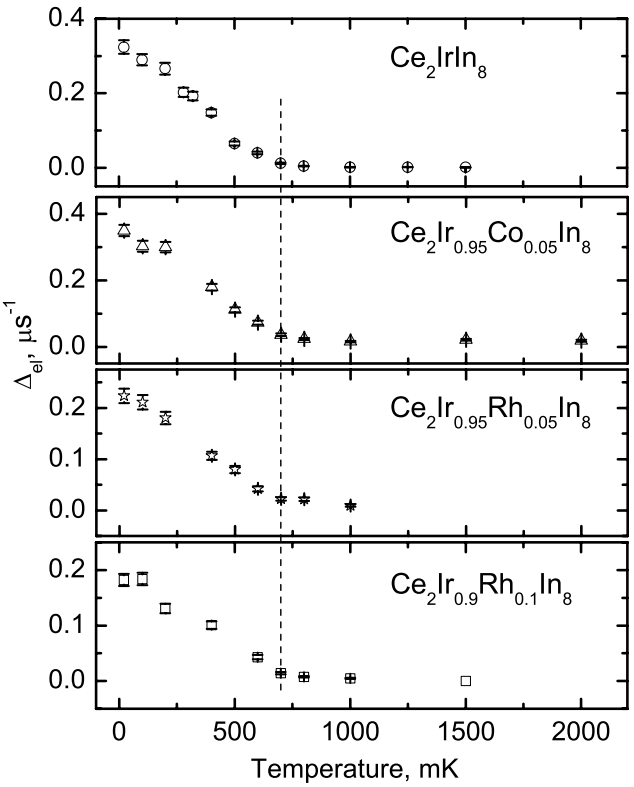

Fig. 113. Linewidths $\Delta_{\rm el}(T)$ characterizing the electronic contribution to muon spin relaxation in several $Ce_2Ir_{1-\delta}M_\delta In_8$ samples.

Runs with a longitudinal field of 20 mT applied parallel to the muon spin resulted in complete decoupling of the muon spin from the internal field, indicating the electronic moments are static on timescales of μs. We conclude that all the samples near the M=Ir composition develop weak, static and disordered electronic moments. These μSR results rule out the possibility of a quantum critical point at M=Ir in the Ce-218 family.

Experiment 894
Muonium kinetics and free radical formation in solutions of fullerenes
(P.W. Percival, SFU)

Aqueous solutions of fullerenes have long been sought for their application in biological systems. However, fullerenes are notoriously difficult to dissolve, and being hydrophobic their solubility in water is even more of a problem. One approach has been to generate fullerene sols, i.e. colloidal suspensions. Various methods of producing sols have been developed in the past few years, including (a) sonication of millimolar concentrations of fullerenes in organic solution in the presence of water; (b) preparation of organic solutions of the mono-anion, which are then added drop-wise to water; and (c) direct injection of a small amount of a concentrated solution of fullerene in an organic solvent into water. In all cases the organic solvent is removed, leaving fullerene clusters suspended in water.

Experiment 894 was conceived to explore muonium chemistry in aqueous fullerene sols. We set out to answer questions such as: How does fullerene aggregation affect chemical kinetics? Is the reaction between Mu and the sol clusters diffusion-controlled? What is the nature of the reaction? Can we identify the product? The chemistry is well understood for organic (true) solutions of fullerenes: In previous work (TRIUMF Expts. 654 and 749) we have clearly shown that Mu adds to fullerene molecules to form the radical adduct, e.g.

$$\mathrm{Mu} + \mathrm{C_{60}} \rightarrow \mathrm{C_{60}Mu}\,.$$

Radio frequency muon spin resonance, low-field

muon spin rotation (μSR), and muon level-crossing resonance (using ^{13}C-labelled material) have all been used to characterize the radicals formed from C_{60} and C_{70} in organic solvents. Only the second, low-field μSR is appropriate for aqueous sols, but unfortunately our experiments have been indeterminate. We had hoped to detect a clear signature of the Mu adduct, $(C_{60})_N$Mu, but the lack of a radical signal could be due to several reasons: a different product, broad lines due to a spread of hyperfine constants, or (most likely) simply inadequate concentration to achieve sufficient signal to noise at the radical precession frequencies.

Most of our beam time in 2002 was spent on a different type of measurement, albeit again with frustrating results. Regardless of product, it is possible to measure the damping of the Mu precession signal in low transverse field to determine the rate of reaction. If it is assumed that Mu reacts with a fullerene cluster (sol particle) containing N C_{60} molecules, then the Mu decay rate is given by

$$\lambda - \lambda_0 = k_{\rm sol}[{\rm sol}] = (k_{\rm sol}/N)[C_{60}]$$

where λ_0 is the Mu decay rate in pure water. To interpret the chemical kinetics we need the second-order rate constant $k_{\rm sol}$, but the usual plot of decay rate versus reactant (C_{60}) concentration would give us $(k_{\rm sol}/N)$. However, the aggregation number N is related to the size of the sol particle, which can be determined by dynamic light scattering (DLS). This we have done. In principle, then, we can determine the rate constant $k_{\rm sol}$ and compare it with the prediction for a diffusion-controlled reaction.

Muonium decay measurements have now been made in three different beam periods, but with inconsistent results. Some of the early data can be explained by technical problems, but the use of improved apparatus in 2002 has eliminated this source of error. The explanation for the scattered results seems to lie in the dependence of the reaction rate on the aggregation number N. Not only does N vary with method of sol preparation, it can also have a spread of values in fresh solutions prepared by the sonication method. To get around this problem we tried "aged" samples, which DLS measurements showed to be monodisperse (sol particles with a narrow size distribution). We were able to accumulate a set of consistent and reliable data, only to discover that the Mu decay rate (λ) in such sols is not a simply linear function of C_{60} concentration, as implied by the equation given earlier. Some of these data are shown in Fig. 114. Perhaps N varies with fullerene concentration? Detailed interpretation of the Mu decay results awaits further DLS studies.

Experiment 894 research will form the major part of the M.Sc. thesis of Sonja Kecman (Chemistry, SFU).

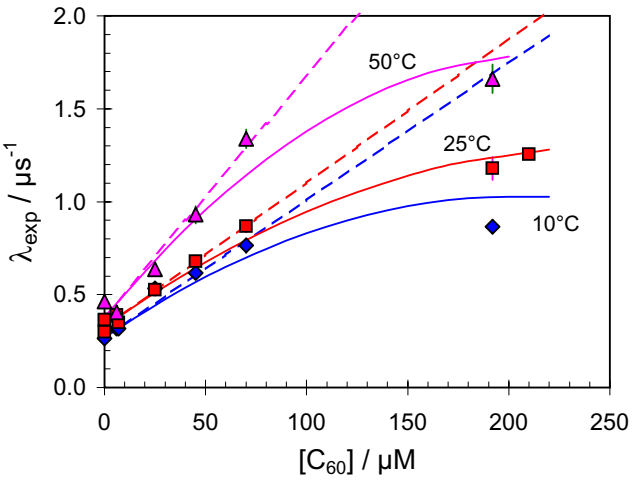

Fig. 114. Muonium decay rates as a function of C_{60} concentration for aqueous sol samples generated by the sonication method. The deviation from the expected linear behaviour is evident at all three temperatures.

Experiment 895
The vortex structure and magnetism of electron-doped cuprate superconductors
(R. Kadono, KEK-IMSS; K.M. Kojima, Tokyo)

Electron-hole asymmetry in the phase diagram of cuprate superconductors is one of the key issues for selecting the models of pairing mechanisms being proposed. Despite its importance, however, so far the study of electron-doped cuprates is far behind that of hole-doped systems. This is partly because of the limited variety of compounds and associated difficulty of obtaining them as large single crystal specimens; earlier works have been done mostly on $L_{2-x}Ce_xCuO_{4-\delta}$ (where L=Nd, Pr, and Sm) which are available only as a small amount of tiny crystals. This situation has been changed recently by Fujita and co-workers from ICR, Kyoto, who succeeded in growing a large single crystal of $Pr_{1-x}LaCe_xCuO_{4-\delta}$ (PLCCO).

Another important issue related to the electron-doped cuprates is the microscopic nature of the oxygen depletion process which is needed to turn the as-grown material into superconducting. It is believed that the excess oxygen atoms occupy apical sites between the CuO_2 planes, and that the removal of those leads to the electron doping. In this regard, the newly synthesized PLCCO has an interesting character in that it is stable over a wide range of the oxygen depletion, $0 \leq \delta \leq 0.12$. In the 2002 beam time, we concentrated on the μSR experiment to map out the magnetic phase diagram of this PLCCO system with δ as the primary parameter. (The phase diagram as a function of carrier concentration x has been reported by other groups, yielding a result similar to $Nd_{2-x}Ce_xCuO_{4-\delta}$ with a little wider region of superconductivity.)

The results of ZF-μSR measurements on

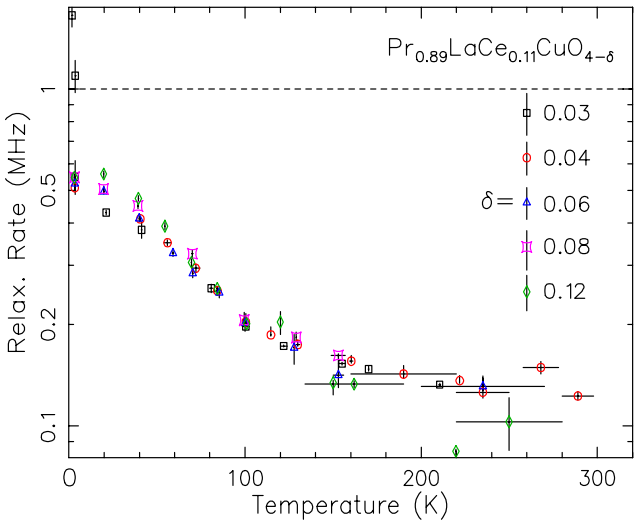

Fig. 115. Muon spin relaxation rate under zero field in $Pr_{0.89}LaCe_{0.11}CuO_{4-\delta}$. It is almost common among all the specimens except for $\delta = 0.03$, where the relaxation rate shows a steep increase below ∼2 K.

$Pr_{0.89}LaCe_{0.11}CuO_{4-\delta}$ with δ=0.03, 0.04, 0.06, 0.08, and 0.12 are summarized in Fig. 115. The relaxation rate exhibits a universal behaviour of increase with decreasing temperature below about 150 K regardless of the oxygen depletion. The observed time spectra in those specimens are common to show an exponential depolarization overlapped with Gaussian-like damping due to nuclear dipolar fields, indicating that the origin of the exponential relaxation is due to random magnetic moments. The absence of δ dependence further suggests that the random moments are carried by Pr^{3+} ions, although the ground state of which is presumed to be nonmagnetic. This means that there is a significant contribution of magnetic excited levels split by the crystal electric field over this temperature range. A similar situation has been reported to occur in $Pr_{1.85}Ce_{0.15}CuO_{4-\delta}$ (see 2000 TRIUMF Annual Report). A more detailed report is now in preparation.

Experiment 912
Formation, structure and dynamics of muonium in GaAs studied by EF-RF μ^+SR
(V.G. Storchak, Kurchatov)

Studies of traps and recombination centres in semiconductors is of fundamental and technological interest. Muon spin relaxation experiments with electric fields (EF) have shown that in condensed samples the stopped muon is very close to (at distances less than 10^{-5}cm) or even surrounded by its own track products. Some excess electrons generated in the track are close enough to reach and to be captured by the stopped muon and form a muonium atom. This process of delayed muonium formation is relevant to the process of trapping excess electrons by an attractive centre.

Radio frequency (rf) μSR is particularly well suited for investigating such processes because this technique can detect final states that are formed within a μs timescale, rather than only prompt or formed within nanoseconds scale fractions which are detected by conventional time-differential (TD) μSR. Here we report an EF + RF-μSR experiment in semi-insulating GaAs providing a demonstration of the role of track electrons in muonium dynamics.

Time-differential μSR experiments show that at low temperatures, $T < 100$ K, virtually no diamagnetic muonium (i.e. Mu^+ or Mu^-) is formed after muon implantation into semi-insulating GaAs RF-μSR studies detect a significant diamagnetic fraction at low temperatures: the diamagnetic fraction appears at $T \sim 20$ K and rises to about 0.4 at $T \sim 60$ K. Electric field dependences of the diamagnetic rf fraction measured at two different temperatures are presented in Fig. 116.

At $T = 61.5$ K the diamagnetic fraction in small electric fields $|E| < 2$ kV/cm is big; at high electric fields data tend to low temperature points.

There are two alternative explanations of this behaviour. According to the first approach the diamagnetic signal seen at low electric fields at $T = 61.5$ K is due to slow thermal ionization of Mu^0_{BC}. To explain the decrease of the diamagnetic signal in moderate electric fields one has to include rapid track electron recapture by the $Mu^0_{BC} \rightleftharpoons Mu^+_{BC}$ process.

An alternative model involves Mu^-_{BC} formation. Just after the slowing down process, the bare muon is surrounded with a cloud of its own track electrons. Due to strong Coulomb interaction, the muon captures one of the track electrons and forms Mu^0_{BC}. At this stage Mu^0_{BC} is still surrounded by electrons. Neutral muonium can attract a second electron and form Mu^-.

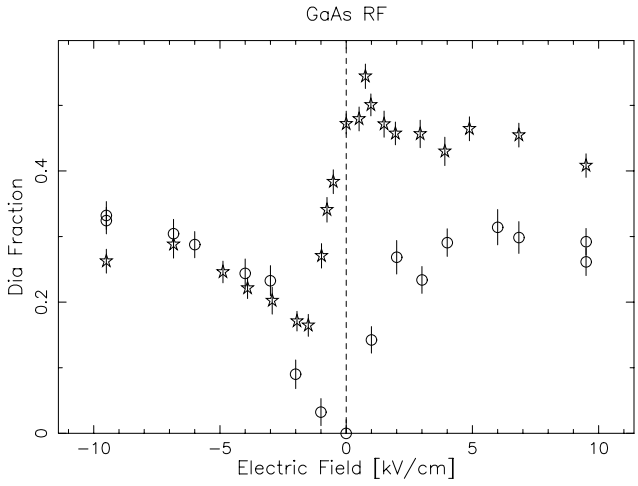

Fig. 116. Diamagnetic RF fraction in semi-insulating GaAs as a function of electric field. Circles: $T = 15$ K; stars: $T = 61.5$ K. Positive electric field is in the direction of the initial muon beam momentum.

The muonium-electron interaction is a weak charge-induced dipole attraction and muonium-electron mutual motion is a diffusion controlled random walk. At low temperatures the diffusion coefficient is small ($D = \frac{kTb}{e}$, where b is the electron mobility) and the probability of Mu^- formation is negligible. As the temperature is raised, D becomes larger and the probability of Mu^- formation increases. At some temperature Mu^- starts to ionize and the fraction we observe in zero electric field is a result of the $Mu^0 \rightleftharpoons Mu^-$ exchange process. This is valid until Mu^0_{BC} starts to ionize. According to the model of Mu^0_{BC} formation through the intermediate shallow state, this critical temperature is about 100 K. Electric fields higher than $E_c \approx 5$ kV/cm prevent Mu^0_{BC} formation and the diamagnetic fraction corresponds to the bare muon. Low electric fields move the cloud of track electrons away from the already formed Mu^0_{BC} and thus diminish the probability of Mu^- formation.

In conclusion, EF + RF-μSR experiments have been successfully carried out in semi-insulating GaAs. The results suggest Mu^- formation at $T < 100$ K and open new opportunities to study electron capture by positive and/or neutral centre in a semiconductor.

Experiment 915
Muonium in semiconductor alloys
(R.L. Lichti, Texas Tech)

TRIUMF Expt. 915 consisted of two separate parts, one to study the silicon-germanium alloys and the second to examine II-VI alloys with Cd and Zn mixed on one sublattice. The first week of beam time, taken in 2001, concentrated on the $Si_{1-x}Ge_x$ system, while the second week taken this year was on the (Cd,Zn)X chalcogenide alloys.

Figure 117 gives an update on results for the (Si,Ge) alloys, showing the mean hyperfine parameter for the bond-centred (BC) Mu^0 state as a function of alloy concentration. Although this graph shows that the average hyperfine interaction is remarkably linear across the full alloy range, a more detailed examination of the lineshapes and temperature dependences suggests that there may be a slight site preference for Si-Si bonds for Mu^0_{BC} at low temperatures. This is one of several areas to be pursued in future Expt. 915 allocations.

The metastable Mu^0_T state was only observed cleanly in one sample with low Ge content, x = 0.2; while any possible spin precession signal from Mu^0_T for x = 0.45 and 0.77 was very broad if observed at all. From the one data point, it appears that the hyperfine constant decreases from A_{hf}(T) for Si for small x instead of increasing toward the value for Ge. The implied non-monotonic behaviour for the T-site Mu^0 will

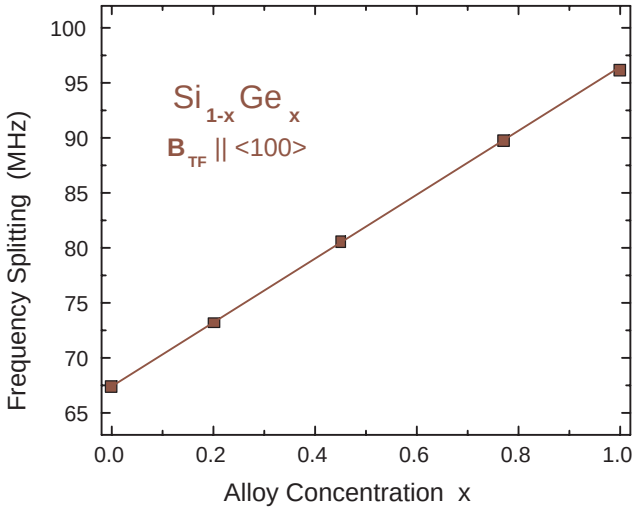

Fig. 117. The average hyperfine splitting obtained for Mu^0_{BC} as a function of concentration in the $Si_{1-x}Ge_x$ alloys. This variation, representing the isotropic part of A_{hf}(BC), is surprisingly linear across the full range.

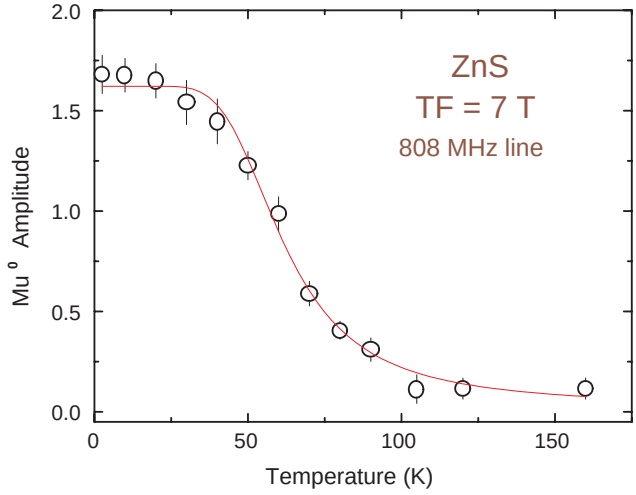

Fig. 118. The temperature dependent amplitudes for the Mu^0 signal in ZnS suggest a very low ionization energy, although the hyperfine constant implies a highly localized impurity-like electronic wavefunction for Mu^0 rather than that for an effective-mass shallow donor.

be investigated further with additional samples having low Ge concentration to follow the hyperfine splitting in more detail.

During the week of time dedicated to the II-VI alloys, we looked at several samples with low Zn content for both the (Cd,Zn)S and (Cd,Zn)Te systems. Unfortunately, we did not observe either a shallow donor or an atomic-like Mu^0 spin precession signal in any of these II-VI alloy samples. However, for Zn content below about 15% in both systems, at temperatures below 30 K there were changes in the relaxation functions associated with the diamagnetic signals that suggested the possibility of a shallow Mu^0 state undergoing very

fast dynamics of some sort. We suspect charge transfer with other defects since the impurity and native defect concentrations are quite high in the samples available during that beam time. Only an atomic-like Mu^0 signal was seen in the ZnS binary compound; however, this signal disappears by about 100 K as seen below.

The temperature dependence for the atomic-like (deep) Mu^0 centre in ZnS is shown in Fig. 118. Although the temperature at which the Mu^0 signal disappears is quite low, the large hyperfine constant, nearly the full free-atom value, identifies this state as a deep Mu^0 defect. Investigation of muonium states in the II-VI alloys as well as in the parent binary compounds will continue as part of a newly proposed experiment to determine the muonium (or hydrogen) defect energy level for comparison to recent theoretical predictions.

Experiment 916
QLCR of diamagnetic muonium states in GaP
(R.L. Lichti, Texas Tech)

Zero-field depolarization functions demonstrated that several different diamagnetic muonium states exist in doped GaP. The aim of TRIUMF Expt. 916 is identification of these states using quadrupolar level-crossing resonances (QLCR). The two Ga isotopes produce a clear signature of a Ga near neighbour to the muon, while P has no quadrupolar nuclei, and thus is invisible to this technique. We initially examined a mid-10^{16}cm^{-3} n-type sample near room temperature where the expected state is an isolated Mu^-; however, the resonances were weak and identification was not conclusive. Two higher concentration n-type samples and a heavily Zn-doped p-type sample have now been examined at temperatures where isolated Mu^- and Mu^+ were expected. We used earlier spectra for these states in GaAs as a guide in searching for their signature in GaP. The results confirm our preliminary identification of those states based on zero-field assignments.

Figure 119 (top) shows the Mu^- QLCR signature at 140 K with B$\|\langle 100\rangle$ for a 10^{18}cm^{-3} n-type GaP:S sample. This resonance is essentially identical to that for Mu^- in GaAs except that it is shifted to higher fields, implying an electric-field gradient (EFG) about 15% larger at the Ga neighbours in GaP compared to GaAs. The Mu^- location is assigned to the T-site with Ga nearest neighbours in both materials.

The diamagnetic fraction does not appear to change with n-type concentration as expected. There is essentially no major difference in three samples covering more than 2 orders of magnitude in electron concentration: Fig. 119 (bottom) shows the temperature dependence [Expt. 916 data below 300 K] for the high concentration sample. The state identity above 200 K

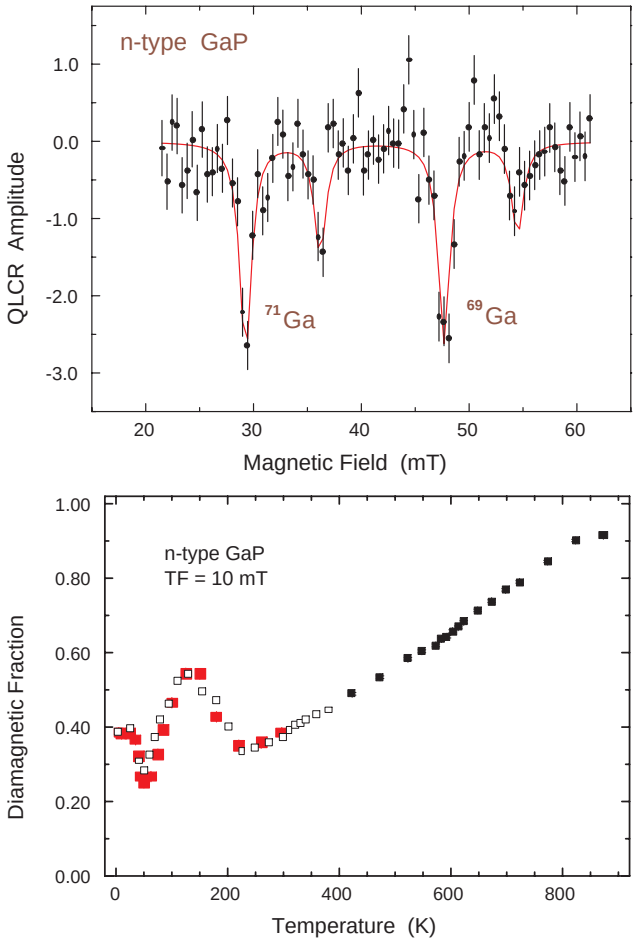

Fig. 119. QLCR spectra (top) confirm Mu^- in the T_{Ga} site at 140 K for heavily doped n-type GaP. However, the temperature-dependent diamagnetic fraction (bottom) is not as expected and further tests are required above 200 K.

remains in doubt pending QLCR tests in that range.

Most recently we examined the QLCR for Mu^+ in p-type GaP, finding the largest amplitude lines from both Ga isotopes. These lines are again at slightly higher fields compared to the GaAs spectra. These data confirm Mu^+ at the BC location at 150 K in GaP:Zn and indicate a somewhat larger EFG at Ga than for the Mu^+ state in GaAs. This trend in EFG is present for all states observed by QLCR thus far.

In addition to data at 150 K, the ^{71}Ga resonance was recorded at 50 K. A reduced amplitude at 50 K is consistent with zero-field data which suggest that up to 1/3 of the Mu^+ related centres may be paired with the Zn acceptor below about 100 K. A search for a different QLCR spectra to confirm a second state at low temperatures is planned for future Expt. 916 beam time.

To date, we have confirmed preliminary identification of three of the five proposed diamagnetic states in doped GaP; Mu^- at T_{Ga}, Mu^+ at BC, and a high-

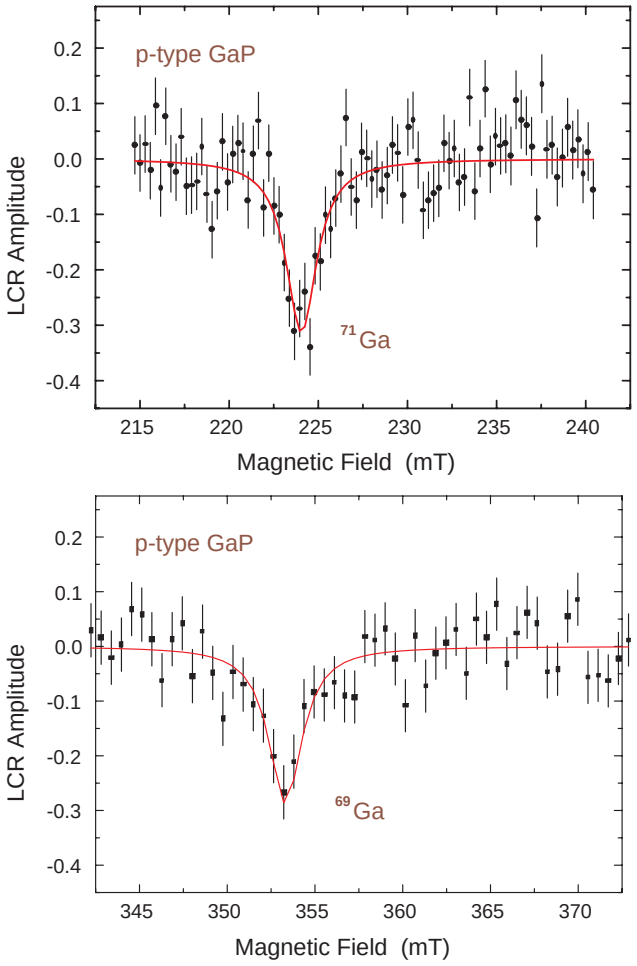

Fig. 120. QLCR spectra for the main line from ^{71}Ga (top) and ^{69}Ga (bottom) for Mu^+ in heavily doped p-type GaP at 150 K confirming the BC site based on similarity to the results for p-type GaAs.

temperature Mu-Zn paired state formed by Coulomb capture of mobile Mu^+ by Zn^-. We still seek confirmation of low-temperature pair formation proposed to occur by charge transfer interactions between mobile Mu_T^0 centres and neutral donors or acceptors below their respective ionization temperatures.

Experiment 917
Correlation between magnetism and transport properties of thermoelectric oxides
(J. Sugiyama, Toyota CRDL Inc.; J.H. Brewer, UBC-TRIUMF)

The "good" thermoelectric layered cobaltites $Ca_3Co_4O_9$ and Na_xCoO_2 share a common structural component: the CoO_2 sheets, in which a two-dimensional-triangular lattice of Co ions is formed by a network of edge-sharing CoO_6 octahedra. Charge carrier transport in these materials is thought to be restricted mainly to these CoO_2 sheets, as in the case of the CuO_2 planes for the high-T_c cuprates.

A recent μ^+SR experiment [Sugiyama *et al.*, Phys. Rev. **B66**, 134413 (2002)] indicated the existence of an incommensurate (IC) spin density wave (SDW) state below 100 K in $Ca_3Co_4O_9$, which was not detected previously by other magnetic measurements [Masset *et al.*, Phys. Rev. **B62,** 166 (2000)]. Meanwhile, the resistivity $\rho(T)$ exhibits a broad minimum around 80 K. Since the behaviour of conduction electrons is strongly affected by their magnetic order, this suggests a strong electron-electron correlation in $Ca_3Co_4O_9$. In order to further clarify the role of magnetism in thermoelectric layered cobaltites, we have measured both weak (∼100 Oe) transverse-field positive muon spin rotation and relaxation (wTF-μ^+SR) and zero field (ZF-) μ^+SR time spectra in $Ca_3Co_4O_9$ at temperatures below 700 K.

Figures 121(a) and (b) show the temperature dependences of the paramagnetic asymmetry $A_{\rm para}$ and the corresponding relaxation rate $\lambda_{\rm para}$ in three $Ca_3Co_4O_9$ samples: a randomly oriented polycrystalline sample, a c-aligned polycrystalline sample and single crystal platelets. The large decrease in $A_{\rm para}$ below 100 K (and the accompanying increase in $\lambda_{\rm para}$) indicates the existence of a magnetic transition with an onset temperature $T_c^{\rm on} \approx 100$ K and a transition width $\Delta T \approx 70$ K. The single crystal data suggest that the

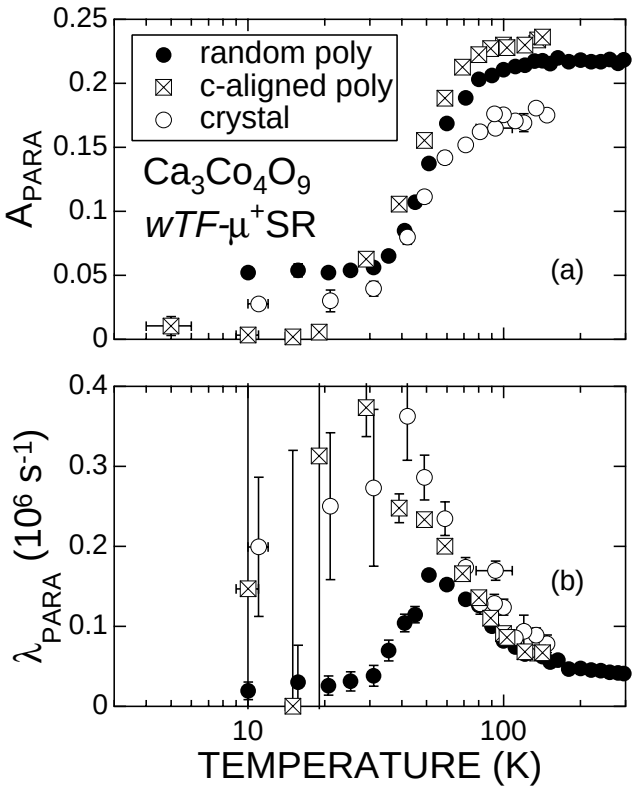

Fig. 121. (a) Paramagnetic asymmetry $A_{\rm para}$ and (b) relaxation rate $\lambda_{\rm para}$ as functions of temperature for the three $Ca_3Co_4O_9$ samples.

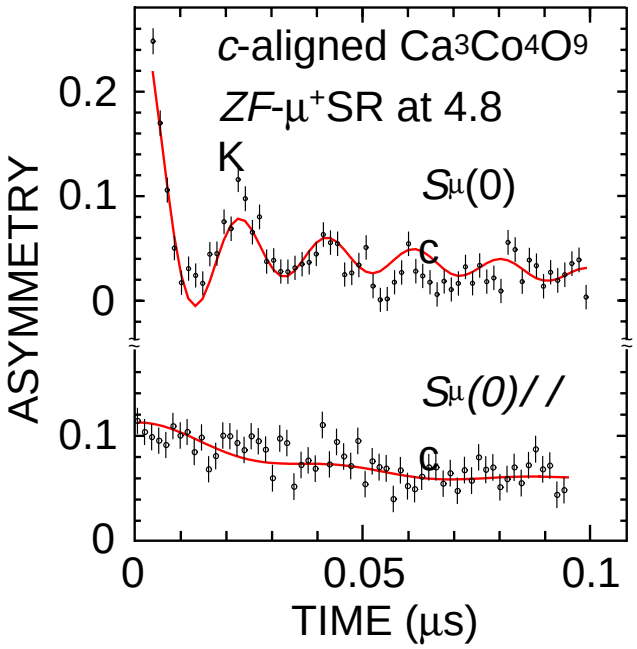

Fig. 122. ZF-μ^+SR time spectra of the c-aligned $Ca_3Co_4O_9$ plate at 4.8 K.

large ΔT is not caused by inhomogeneity of the sample but is an intrinsic property of this compound.

Figure 122 shows ZF-μ^+SR time spectra at 4.8 K in the c-aligned sample; the top spectrum was obtained with the initial μ^+ spin direction $\mathbf{S}_\mu(0)$ perpendicular to the c-axis and the bottom one with $\mathbf{S}_\mu(0) \parallel \hat{\mathbf{c}}$. A clear oscillation due to quasi-static internal fields is observed only when $\mathbf{S}_\mu(0) \perp \hat{\mathbf{c}}$. This oscillating spectrum is reasonably well fitted by the phenomenological function for an incommensurate spin density wave (IC-SDW) state [Kalvius *et al.*, in *Handbook on the physics and chemistry of rare earths* **32** (North-Holland, Amsterdam, 2001) p. 55], namely a zeroth-order Bessel function of the first kind. We therefore conclude that $Ca_3Co_4O_9$ undergoes a magnetic transition from a paramagnetic state to an IC-SDW state (i.e. $T_c^{\rm on} = T_{\rm SDW}^{\rm on}$). The absence of a clear oscillation in the bottom spectrum of Fig. 122 indicates that the internal magnetic field $\mathbf{H}_{\rm int}$ is roughly parallel to the c-axis, since the muon spins do not precess in a parallel magnetic field. The IC-SDW is therefore considered to propagate in the a-b plane, with oscillating moments directed along the c-axis.

The high-temperature wTF-μ^+SR spectra in the c-aligned $Ca_3Co_4O_9$ sample indicate the existence of a broad shoulder in the $\lambda_{\rm para}(T)$ curve at 400–600 K, although such a shoulder seems to be ambiguous in the Y-doped sample (Fig. 123(a)). This behaviour is in good agreement with the results of $\chi(T)$ measurements (see Fig. 123(b)). At these temperatures muons are diffusing rapidly, so that the relaxation rate usually decreases monotonically with increasing temperature.

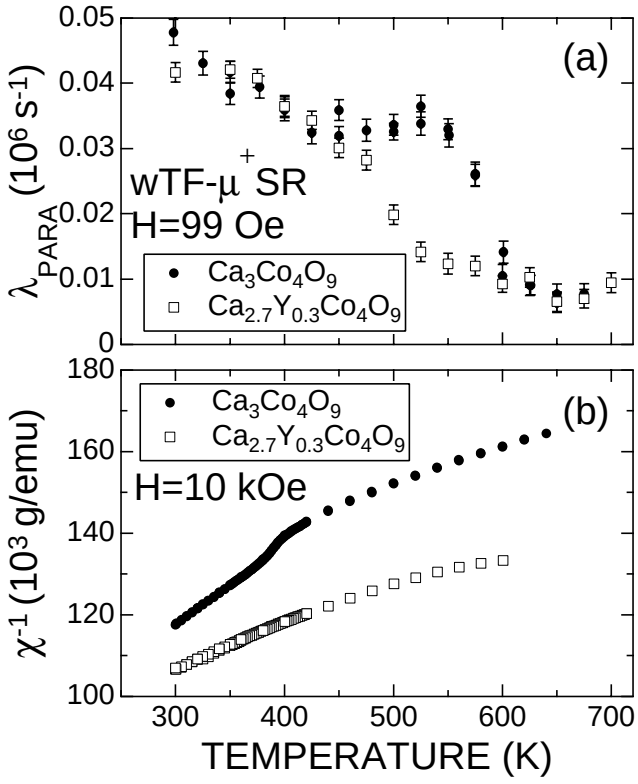

Fig. 123. Temperature dependences of (a) $\lambda_{\rm para}$ and (b) the inverse susceptibility χ^{-1} in polycrystalline $Ca_3Co_4O_9$ and $Ca_{2.7}Y_{0.3}Co_4O_9$ samples.

Furthermore, above 150 K $A_{\rm para}$ levels off to its maximum value ($\sim$0.23) – i.e., the sample volume is almost 100% paramagnetic. Hence we can conclude that this shoulder is induced by the spin state transition. Since $H_{\rm int}$ increases due to the spin state transition above $T_{\rm SS}$, $\lambda_{\rm para}$ is expected to increase with increasing T. On the other hand, both the rapid muon diffusion and the fast exchange rate of electrons between Co^{3+} and Co^{4+} ions decrease $\lambda_{\rm para}$ with increasing T. The competition between these three factors is likely responsible for the broad shoulder in $\lambda_{\rm para}(T)$ around 400–600 K.

The broad shoulder also indicates that the spin state changes gradually in the temperature range between 400 and 600 K. If the transition occurs abruptly at $T_{\rm SS}^{\chi}$ as seen in the $\chi^{-1}(T)$ curve, then a calculation [Koshibae *et al.*, Phys. Rev. **B62**, 6869 (2000)] using the degeneracy of spin and orbital degrees of freedom of Co ions predicts that the thermoelectric power should show a dramatic change at $T_{\rm SS}^{\chi}$. Therefore, this gradual change in the spin state is apparently essential to the large thermoelectric power at elevated temperatures.

Figure 124 summarizes the magnetic transitions in $Ca_3Co_4O_9$. The two magnetic transitions detected by μ^+SR, i.e. the IC-SDW and the spin state transitions, are found to correlate closely with the transport properties of $Ca_3Co_4O_9$. The existence of the IC-SDW transition indicates an enhancement of the effective mass

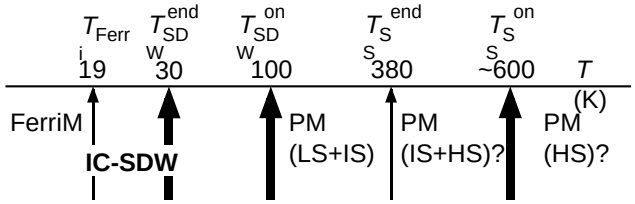

Fig. 124. Successive magnetic transitions in $Ca_3Co_4O_9$. The bold arrows indicate the transitions found by Expt. 917, while the narrow arrows show those detected by the previous susceptibility measurements.

of charge carriers (and thus the thermoelectric properties) by strong electron correlations. The existence of the spin state transition suggests that the crystal-field splitting between t_{2g} and e_g levels is comparable to ∼400 K. Furthermore, the gradual change in the spin state prevents a decrease in thermoelectric power above T_{SS}^{end}. In other words, these transitions are likely to be key factors in achieving a good thermoelectric performance.

Experiment 918
High field study of La_2CuO_4 based superconductors
(G.M. Luke, McMaster; Y.J. Uemura, A.T. Savici, Columbia)

Experiment 849 revealed the coexistence of static magnetic order and superconductivity in several La_2CuO_4 based samples, relatively close to hole concentration of 1/8 per Cu atom in spatially separated regions. Computer simulations suggest a radius of the magnetic regions on the order of 30 Å.

Mostly neutron inelastic scattering, but also some older μSR data, show that a high magnetic field tends to induce magnetic correlations in these samples. We therefore decided that it might be interesting to determine if we have an increase in the size of the magnetic moments or if we have an increase in the size of the magnetic regions.

We performed high magnetic TF-μSR measurements on several samples of $La_{2-x}Sr_xCuO_4$ (LSCO) and $Bi_2Sr_2CaCu_2O_{7-\delta}$ (Bi2212). While in Bi2212 we see no field induced magnetism in either underdoped or optimally doped samples, the picture for LSCO is completely different. We fitted the data by a gaussian damped cosine function. As we can see in Fig. 125, the TF relaxation rate increases with the applied field in the case of underdoped and optimally doped samples, but there is no field induced effect in the case of the overdoped one. The value of the relaxation rate at low temperatures is dependent on the time domain of fitting, which implies that this simple model is not enough.

We therefore need a better way to look at the data, even before we propose a model. Beside the standard

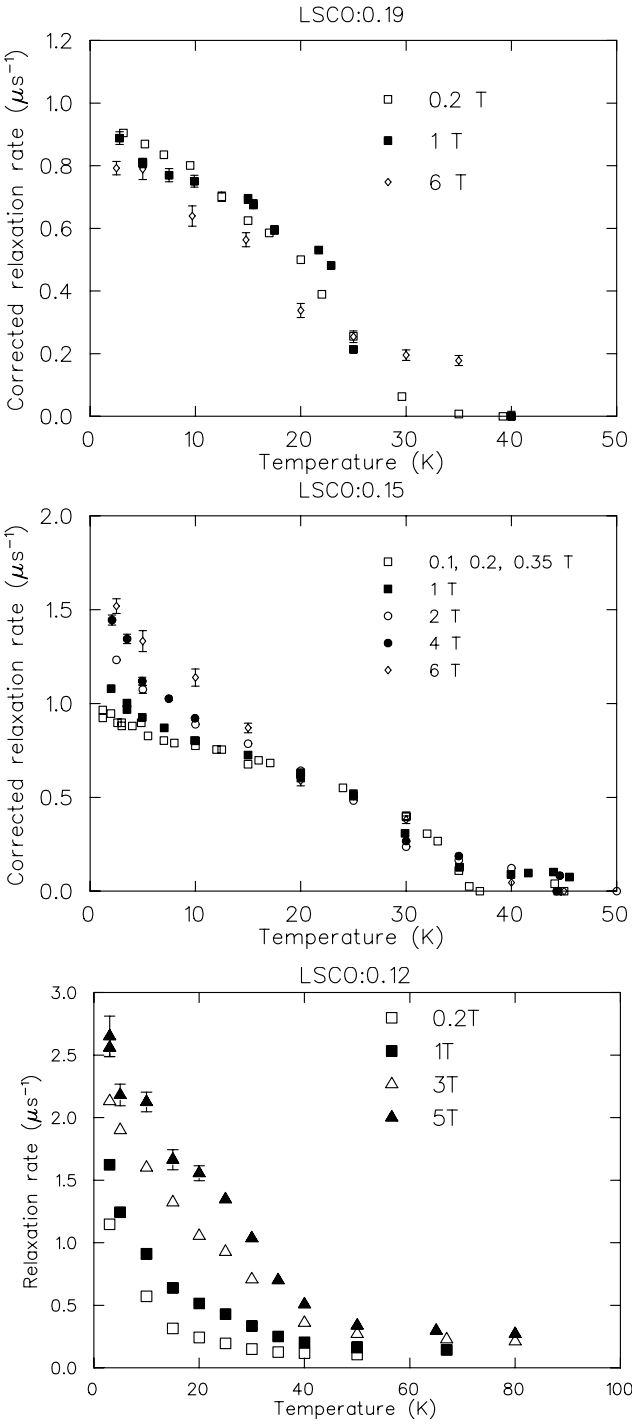

Fig. 125. Relaxation rates for TF-μSR signal in several LSCO samples.

way of looking at the asymmetry in rotated reference frame, we found that the Fourier transform does not produce enough new information to be useful in understanding the data. Another way to get useful results is looking at the envelope function. The results for $La_{2-x}Sr_xCuO_4$ are shown in Fig. 126. In the case of overdoped LSCO ($x = 0.19$) we see no change. For

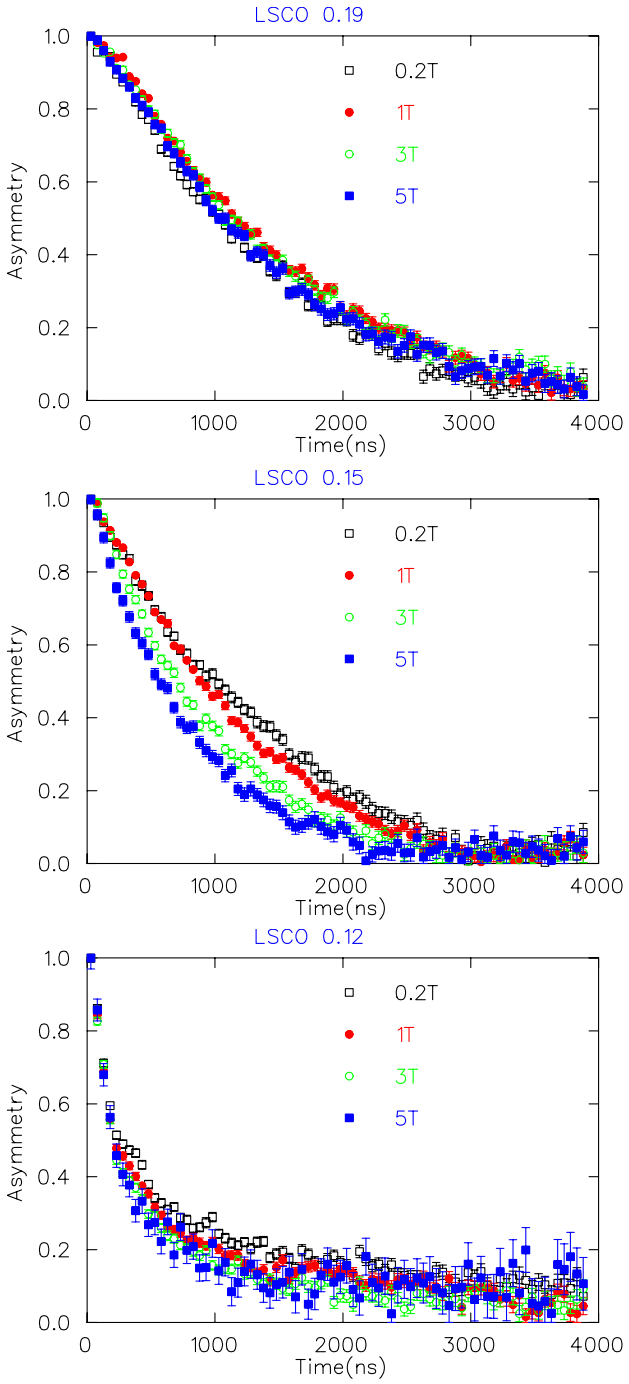

Fig. 126. Envelope functions for TF-μSR signal in several LSCO samples.

$x = 0.15$ we see a gradual change, all across the time spectrum. The $x = 0.12$ sample exhibits a two component signal, with a fast relaxation due to the magnetically ordered regions.

For the optimally doped LSCO sample, we see no volume fraction of sites with high magnetic fields. The field-induced relaxation in LSCO:0.15 seems to be due to slowing down of spin fluctuations occurring in the whole volume of the sample.

Experiment 931
Magnetic properties of multinuclear, open-shell coordination complexes and polymers probed by μSR
(J.E. Sonier, D.B. Leznoff, SFU)

Compounds that contain unpaired electrons, also called "open-shell" systems, can be found throughout chemistry, from the active sites in many proteins to magnetic materials. Every open-shell compound contains a particular "spin carrier" that actually carries the unpaired electron(s), such as transition metal ions, lanthanides and organic radicals. Molecular magnetism deals with the magnetic properties of isolated molecules and groups of molecules, which contain one or more spin carriers. It is the combination of these spin carriers, the bridges connecting them, and their multidimensional assembly that generates materials with unique properties. At the heart of these investigations are two general goals: first, we seek to understand the magnetic interactions between spin carriers, both via direct bonding and mediated by ligand bridges. The key issue of interest is the strength and type of magnetic coupling (ferromagnetic or antiferromagnetic) for a given system. Second, methods to generate high-dimensional systems in a controlled fashion must be explored and applied to open-shell systems. Generally, high-dimensionality systems can show bulk properties (magnetic, thermal, optical) attributable to their polymeric nature.

$Cu[Au(CN)_2]_2 \cdot H_2O$

The coordination polymer $Cu[Au(CN)_2]_2 \cdot H_2O$ shows ferromagnetic coupling down to 2 K. μSR measurements of this compound in zero external magnetic field show a first-order transition to magnetic order near 0.19 mK. Upon warming, hysteresis is observed (see Fig. 127). An outstanding question is whether the magnetic exchange coupling is mediated by the Au(I) centre or the copper(II)-bound H_2O via an H-bonding array.

$C_{24}H_{60}N_4Si_4O_2Fe_2$

The metal-diamidoether complex $C_{24}H_{60}N_4Si_4O_2Fe_2$ is unstable in air. Consequently, a special sample cell was prepared for use in a conventional He gas-flow cryostat. This limited the lowest temperature to ~2.3 K. Measurements in zero external magnetic field indicated a slowing down of the spin dynamics with decreasing temperature (see Fig. 128). However, no magnetic transition was observed.

Cu(II)/Au(I) and Cu(II)/Hg(II) 2-D arrays

The reaction of $Cu(ClO_4)_2 \cdot 6H_2O$ with tmeda (tmeda = $Me_2NCH_2CH_2NMe_2$) and two equivalents of

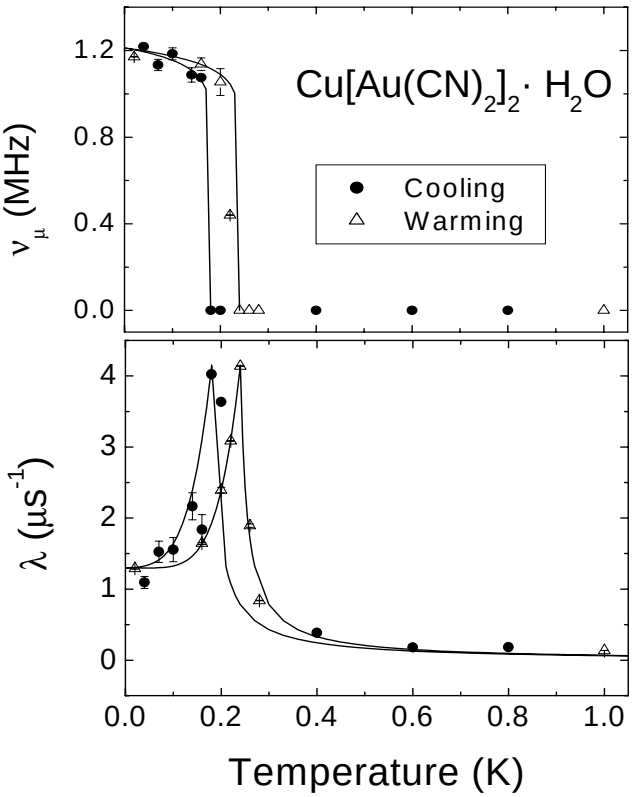

Fig. 127. Zero-field μSR measurements on polycrystalline $Cu[Au(CN)_2]_2{\cdot}H_2O$ taken as a function of increasing (open circles) and decreasing (solid circles) temperature. The top and bottom panels show the temperature dependence of the muon-spin precession frequency ν_μ and muon-spin relaxation rate λ, respectively.

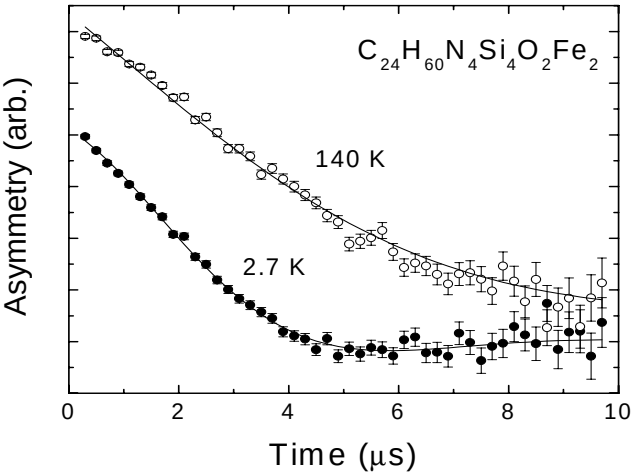

Fig. 128. Asymmetry spectra in $C_{24}H_{60}N_4Si_4O_2Fe_2$ at zero external field. The increased relaxation rate at lower temperatures is consistent with the slowing down of fluctuating magnetic moments, but no onset of magnetic order is observed.

$K[Au(CN)_2]$ yields $Cu(tmeda)[Au(CN)_2]_2$, a 3-D polymer which shows ferromagnetic interactions mediated by the Au(I) centre. We carried out ZF-μSR measurements of this compound to probe the nature of the

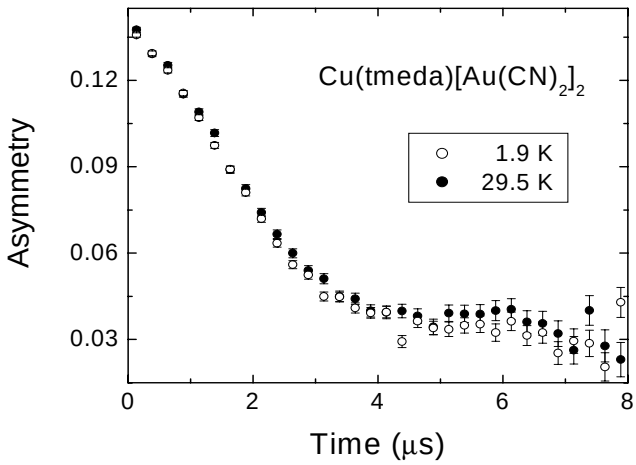

Fig. 129. Asymmetry spectra in $Cu(tmeda)[Au(CN)_2]_2$ at zero external field. The change upon cooling the sample below $T = 25$ K is very subtle.

transition observed at $T = 25$ K in bulk susceptibility measurements. While we did observe a subtle but abrupt change in the muon spin relaxation signal below 25 K (see Fig. 129), no clear evidence for magnetic order was found.

Experiment 932
Improving μ^-SR performance
(J.H. Brewer, CIAR/UBC/TRIUMF)

The applications of μ^+SR to condensed matter physics and chemistry are legion and familiar; by comparison, the uses of μ^-SR are rare and obscure. This is because of the well known disadvantages of μ^-SR (relative to μ^+SR), all of which are related to the formation of muonic atoms in which the μ^- orbits a positive nucleus roughly 200 times closer than a $1s$ electron:

- Lifetime: For heavy nuclei, the μ^- actually spends most of its time inside the nucleus. This has an adverse effect on μ^-SR because, in all but the lowest-Z materials, the muon lifetime τ_μ is dramatically shortened by nuclear capture involving the elementary reaction $\mu^- + p \rightarrow n + \nu_\mu$. In $^{16}O\mu^-$, $\tau_\mu \approx 1.8$ μs, not much shorter than the free muon decay lifetime of 2.197 μs, but in $^{58}Ni\mu^-$ it is only 152 ns and in $^{208}Pb\mu^-$ it is only 75 ns. The fraction of muons producing a decay electron to be detected in a normal μ^-SR experiment is reduced by the lifetime ratio (e.g. 3.4% for ^{208}Pb). On the other hand, higher μ^- stop rates (by the same factor) can be accommodated as long as the extra beam intensity is available and the sample contains no light elements.
- Depolarization: Meanwhile, strong L-S coupling in the radiative transitions of the muon on its way to the muonic $1s$ state cause a dramatic loss of polarization, with the result that no more than

20–25% remains in the ground state. This reduces the sensitivity of μ^-SR (relative to μ^+SR) by the same factor.

- Giant hyperfine interactions: The majority of nuclei have spins of their own. The extreme proximity of the muon to the nucleus causes an enormous hyperfine interaction (in muonic niobium the effective field of the nucleus on the muon is comparable to magnetic fields at the surfaces of neutron stars!) which effectively "locks" together the muon and nuclear spins into an F^+ state (parallel) or an F^- state (antiparallel). The energy difference between these states is often sufficient to eject core electrons in Auger processes accompanying hyperfine transitions. Because of these transitions, and the fact that the $F^\pm$ states precess in magnetic fields at their own characteristic Larmor frequencies different from that of the free muon, conventional wisdom holds that muonic atoms with nonzero-spin nuclei are not useful for μ^-SR studies of condensed matter.

On the other hand, μ^-SR reveals something that μ^+SR cannot: the local magnetic fields at lattice sites occupied by what is essentially a $Z_{\rm eff} = Z - 1$ impurity nucleus – usually $\mathrm{B}_\mu = {}^{12}\mathrm{C}\mu^-$ or $\mathrm{N}_\mu = {}^{16}\mathrm{O}\mu^-$, because most applications of μ^-SR as a condensed matter probe have relied upon muonic atoms of spinless nuclei, primarily ${}^{16}\mathrm{O}\mu^-$ in oxides. However, a number of muonic atoms of nuclei with spin (notably ^{7}Li, ^{9}Be, ^{11}B, ^{14}N, ^{19}F and ^{27}Al) produce useful μ^-SR signals of sufficient strength to be used as magnetic probes of materials that contain these isotopes but no convenient spinless nuclei. Their possible applications have never been seriously explored. Experiment 932 was therefore undertaken to explore some possible ways to make μ^-SR more efficient and versatile.

In the first year of Expt. 932 I have made a few calibration measurements on spinless nuclei and obtained new TF-μ^-SR spectra from ${}^{19}\mathrm{F}\mu^-$, ${}^{14}\mathrm{N}\mu^-$ and ${}^{23}\mathrm{Na}\mu^-$ in chemical compounds, where the F^+ frequency is easily separated from the free μ^- signal of muons captured on ^{12}C and ^{16}O.

${}^{12}\mathrm{C}\mu^-$ lifetime

As usual, graphite was used for calibration. In the process I obtained a ${}^{12}\mathrm{C}\mu^-$ lifetime (Fig. 130) of 2016.5 ± 1.0 ns (500 ppm), which is about half as precise as the best value to date. However, people preparing to measure the μ^+ lifetime to high precision should note that I made no effort to minimize the effects of the muon's polarization and asymmetric decay; instead, I made sure to understand (and fit) it.

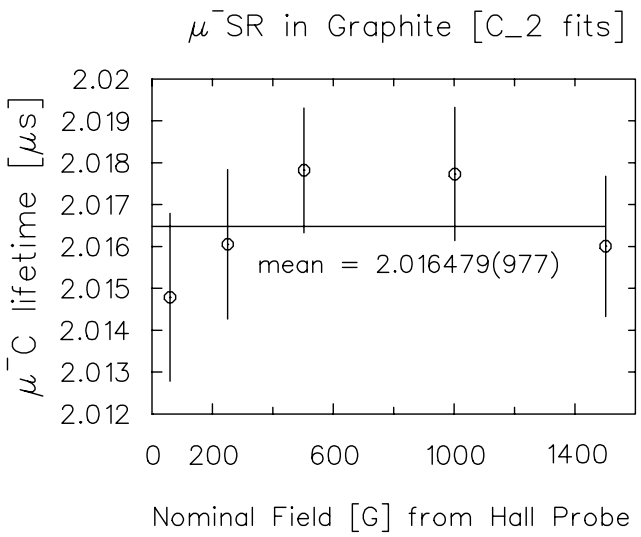

Fig. 130. μ^- lifetime in graphite vs. transverse magnetic field.

Relativistic shifts

I also obtained a nominal value for the ${}^{12}\mathrm{C}\mu^-$ relativistic shift ($-0.035\pm5\%$) [which should not be taken too seriously because there were no controls for systematic errors], as well as those of ${}^{208}\mathrm{Pb}\mu^-$ and natural $\mathrm{Cd}\mu^-$ (where systematics are less of a problem) for comparison with the measurements of Yamazaki *et al.* [Phys. Lett. **B53**, 117 (1974)]. Also, shown in Fig. 131 are the relativistic shifts of ${}^{14}\mathrm{N}\mu^-$ (in melamine, see below), ${}^{19}\mathrm{F}\mu^-$ (in Teflon, see below) and ${}^{27}\mathrm{Al}\mu^-$, where in each case the reference frequency is that calculated for the F^+ hyperfine state (see below).

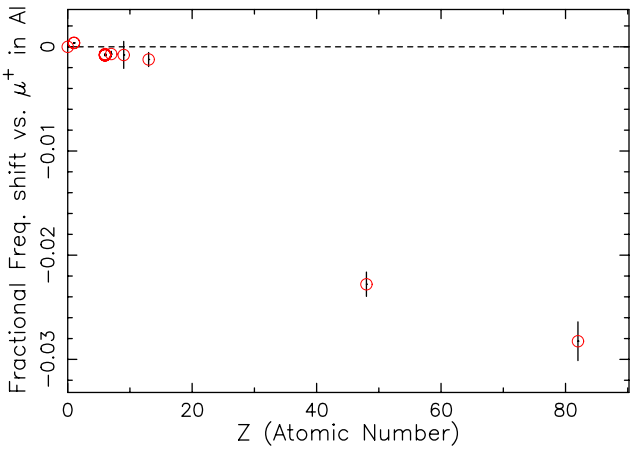

Fig. 131. Relativistic shift of negative muon precession frequency expressed as a fraction of the μ^+ frequency in aluminum at the same transverse magnetic field (0.7 T). Points at $Z = 0$ and $Z = 1$ are for μ^+ in aluminum and graphite, respectively. (In graphite the μ^+ has a large positive Knight shift.)

Giant hyperfine interactions

Since the muon penetrates deep into the nucleus in its $1s$ state, the hyperfine splitting for muonic atoms with nonzero-spin nuclei can be huge. In ^{93}Nbμ^- and ^{209}Biμ^- the energy difference between the F^+ state (muon and nuclear spins parallel) and the F^- state (muon and nuclear spins antiparallel) is $\sim$5 keV – equivalent to a magnetic field of $\sim 10^{14}$ G on the muon. (This is comparable to the magnetic fields at the surfaces of neutron stars!) Even in light nuclei, this interaction rigidly "locks" the muon spin to that of the nucleus in either the F^+ or the F^- state; these states then precess in an external field at well defined Larmor frequencies ν_+ and ν_- quite different from that of the "bare" muon (ν_μ). One can therefore measure the time evolution of the μ^- polarization in any such states independently of each other in a sufficiently strong transverse magnetic field (high enough that the muon survives in the state of interest for at least several periods of the corresponding frequency).

Hyperfine transitions

The hyperfine splitting is often sufficient to eject core electrons in Auger processes, the dominant mechanism for hyperfine transitions. The rates of these transitions are known for a few cases where it has been important to semileptonic nuclear physics experiments, but most have never been measured since the calculations of Winston in 1963 [Phys. Rev. **129**, 2766 (1963)]. As a general rule, the initial $F^\pm$ populations are stable in the lightest elements and transitions begin to be detectable by about ^{11}B.

^{19}Fμ^- in Teflon

The HF transfer rate $R_{\rm HF}$ in muonic ^{19}F is the best known of all such cases, so it made a nice "proof of principle" calibration. As can be seen from Fig. 132, the F^+ signal was easily observed in a Teflon ($(CF_2)_n$) sample and impossible to confuse with the carbon background signal by virtue of their radically different frequencies. Its "relaxation" rate was also easy to measure; with just under 18 hours of data accumulation I was able to determine $R_{\rm HF} = 5.2(5)\ \mu{\rm s}^{-1}$, consistent with previous measurements using neutrons from nuclear muon capture (which is strongly dependent upon the HF state).

I was also able to determine the product of $P_+(0)$ (the initial polarization of the muonic fluorine F^+ state) and the fraction $f_F \cdot f_+$ of muons initially in that state (which includes the fraction f_F initially captured on fluorine as opposed to carbon). The result was $f_F \cdot f_+ \cdot P_+(0) = 0.31(3)\%$.

Hyperfine transition rate in ^{23}Naμ^-

Measurements on sodium metal at a transverse field of about 0.7 T produced a tantalizing result, shown

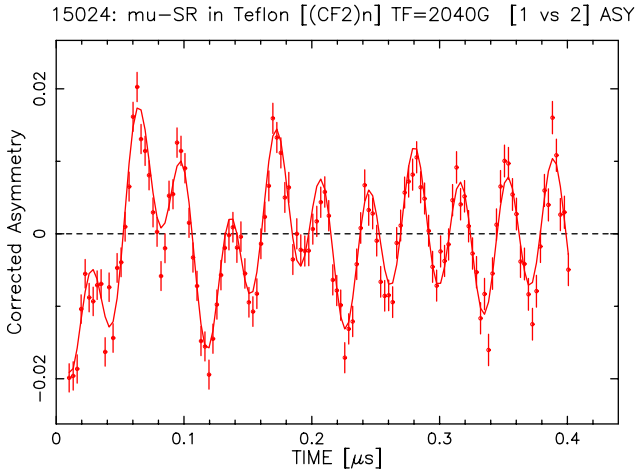

Fig. 132. Negative muon precession signal in Teflon ($(CF_2)_n$) at room temperature in a transverse magnetic field of 2040 G. The long-lived signal at higher frequency is from ^{12}Cμ^- and the rapidly decaying signal is from the F^+ state of ^{19}Fμ^- before its transition to the (singlet) F^- state.

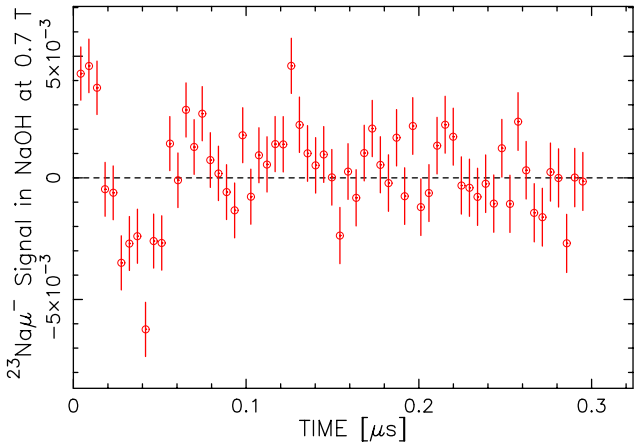

Fig. 133. Precession signal of the F^+ state of ^{23}Naμ^- in sodium metal, showing the apparent relaxation caused by the hyperfine transition to the F^- ground state.

in Fig. 133: a weak signal at a frequency about 0.18 times that of the free muon, consistent with the theoretical frequency of the F^+ state in muonic ^{23}Na ($\nu_+/\nu_0 = 0.18765$), with a "relaxation" rate of about $13 \pm 3\ \mu{\rm s}^{-1}$, consistent with the HF transition rate calculated by Winston in 1963 ($R_{\rm HF} \approx 14\ \mu{\rm s}^{-1}$).

^{14}N in melamine ($C_3H_6N_6$)

The F^+ signal in ^{14}Nμ^- is large and long-lived; its frequency is easily distinguished from that in ^{12}Cμ^-, and so it was easy to measure in a compound containing both nitrogen and carbon, as shown in Fig. 134. The ratio of the fitted ^{14}Nμ^- F^+ frequency to that of ^{12}Cμ^- was $\nu_+/\nu_C = 0.3180(3)$, in agreement with the theoretical value of $\nu_+/\nu_0 = 0.3182$ relative to the free muon frequency ν_0. (Since ^{12}Cμ^- and ^{14}Nμ^- will have

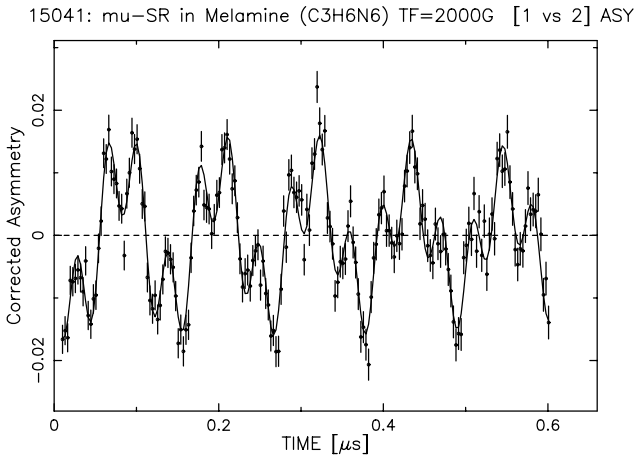

Fig. 134. Negative muon precession signal in melamine ($C_3H_6N_6$) at room temperature in a transverse magnetic field of 2000 G. The higher frequency signal is again from $^{12}C\mu^-$ and the slower decaying signal is from the F^+ state of $^{14}N\mu^-$; in this case the decay is not due to a transition to the F^- state but is caused by some sort of conventional magnetic or chemical spin relaxation mechanism.

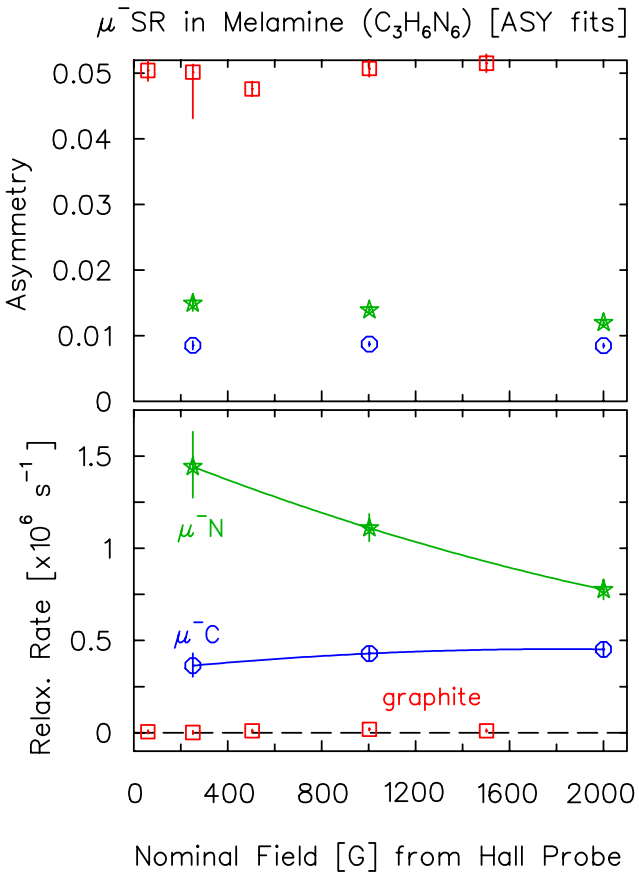

Fig. 135. Fitted asymmetry (top) and relaxation rate (bottom) of negative muon precession signals from $^{12}C\mu^-$ (circles) and $^{14}N\mu^-$ (stars) in melamine ($C_3H_6N_6$) at room temperature for several transverse magnetic fields. Results for pure graphite (squares) are shown for comparison. The relaxation rates are much too high to be caused by random local fields from neighbouring nuclear dipole moments.

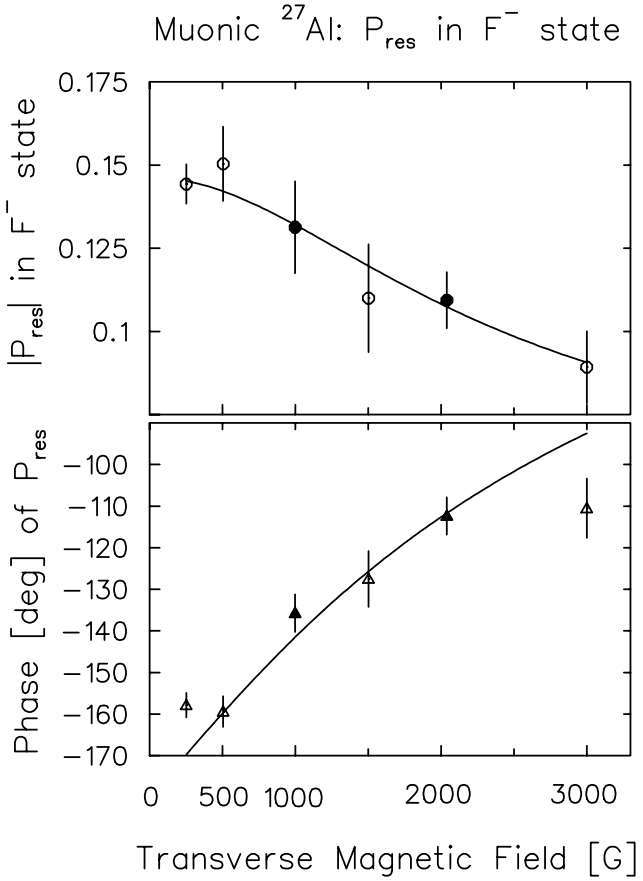

Fig. 136. Magnitude (top) and initial phase (bottom) of the residual polarization of the F^- state in $^{27}Al\mu^-$ as a function of transverse magnetic field. Lines are fits to a simple model.

roughly the same relativistic shift, this complication has been ignored.)

As shown in Fig. 135, the product $f_N \cdot f_+ \cdot P_+(0)$ and the relaxation rate of the F^+ signal were both sharply decreasing functions of increasing magnetic field, starting from 0.01495 ± 0.00129 and 1.44 ± 0.19 μs^{-1}, respectively, at 251 G and dropping to 0.0120(4) and 0.776(5) μs^{-1} at 2000 G. This behaviour is mysterious. The $F^+ \rightarrow F^-$ transition is thought to be energetically forbidden, leading to skepticism about the association of $R_{\rm HF}$ with the (much slower) relaxation rate observed in a liquid nitrogen target in 1983 by Nagamine *et al.* [Phys. Lett. **B167**, 31 (1986)]. The present result is clearly not a HF transition rate, but a "real" spin relaxation by random local magnetic fields; the question is, what could produce such large fields? The rate is too high to be due to nuclear moments, even those of protons. It seems likely that paramagnetic moments are involved, but it is anybody's guess which. This system may be very interesting for reasons as yet unguessed, but it will not make a good one for determining $R_{\rm HF}$ for muonic nitrogen.

Hyperfine transition rate in ^{27}Alμ^-

For elements heavier than sodium, $R_{\rm HF}$ becomes larger than ν_+ in experimentally accessible magnetic fields, so that direct observation of "relaxation" of the F^+ signal is no longer a feasible method for measuring $R_{\rm HF}$. However, at lower magnetic fields the muon polarization can be transferred efficiently to the lower F^- state with a field-dependent amplitude and phase shift. Using this "residual polarization" method I made the first measurement of $R_{\rm HF}$ in ^{27}Alμ^- at SIN in 1982 [Brewer, Hyp. Int. **17-19**, 873 (1984); Brewer, *ibid.*, p.879]. Under Expt. 932 the number of measurements at different fields was increased to confirm this "residual polarization" effect and improve the precision of the measurement (see Fig. 136). As soon as the data analysis is complete, I will publish a new value for the HF ($F^+ \rightarrow F^-$) transition rate $R_{\rm HF}$ as well as the products of initial polarization and population for each of the HF states, which is difficult to determine any other way. It will then be interesting to investigate other muonic atoms of intermediate mass where this method might be used to determine these HF parameters.

Experiment 934
μSR study of polymerized C_{60}
(Y.J. Uemura, Columbia; T. Makarova, Umeå Univ.)

Recently, Makarova *et al.* [Nature **413**, 716 (2001)] reported that polymerized C_{60} exhibited ferromagnetic behaviour at room temperatures. The C_{60} polymerizes into an oriented rhombohedral C_{60} phase (Rh-C_{60}). We performed μSR measurements in ZF and LF on this sample.

We ran two samples of polymerized C_{60} with slightly different annealing temperatures of 750°C and 775°C. Results were extremely similiar for both samples. SQUID magnetometry was performed in the range of –2 kOe< H <2 kOe, for temperatures of 10 K and 300 K. The room temperature magnetization hysteris loops are shown in Fig. 137. One can clearly see a saturation of the magnetization at higher fields 2×10^4. These SQUID results are consistent with the Makarova *et al.* measurements and seem to indicate the presence of ferromagnetic order within the sample.

Our group performed μSR on the Rh-C_{60} samples mentioned above. The results are summarized in Fig. 138. The ZF and WTF measurements show no substantial internal magnetic field within the bulk of the sample. The asymmetry in the ZF measurement does not oscillate, and the WTF measurement does not show any effect of dephasing except due to perhaps lifetime effects of the muon. Hence, there does not seem to be any static internal magnetic field in the sample. We find no evidence of static magnetic order in

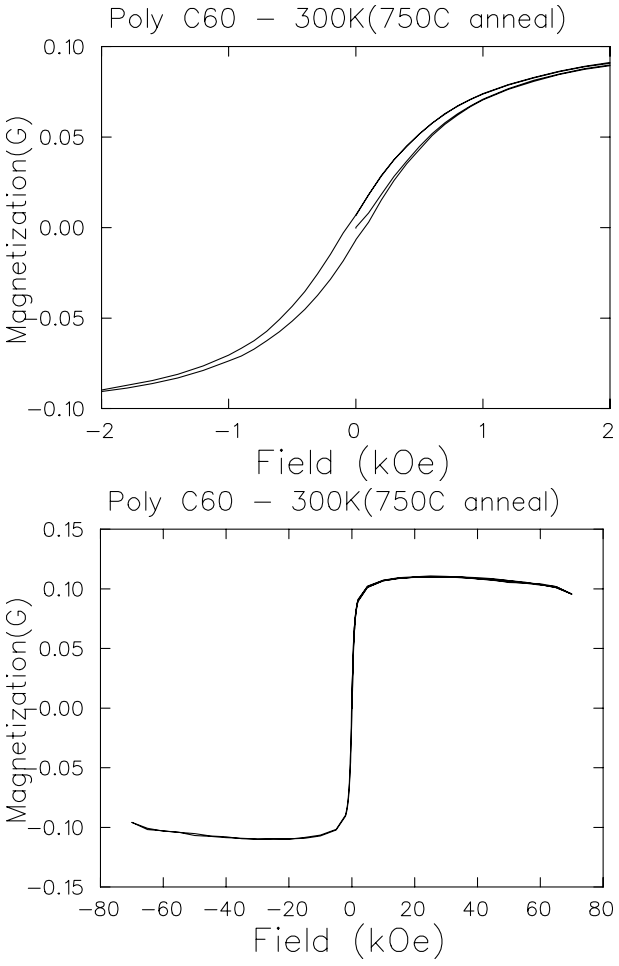

Fig. 137. Magnetic susceptibility for Rh-C_{60} (annealed at 750°C).

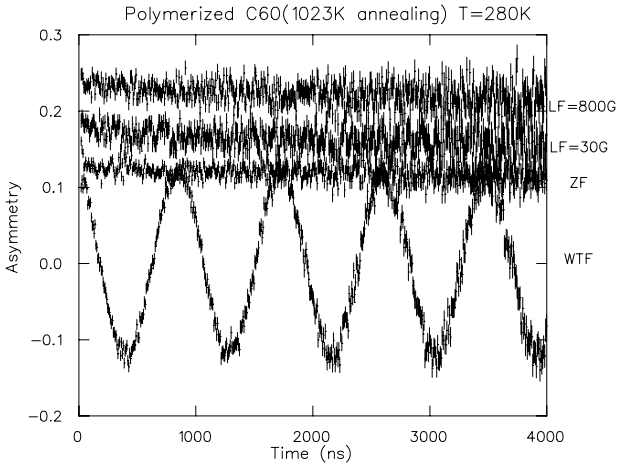

Fig. 138. Results of μSR experiments on Rh-C_{60}.

polymerized C_{60}. The ferromagnetism in the sample may be due to localized impurity. The ZF and LF results indicate that about half of the implanted muons form muonium. Characterization of this muonium state is currently under way.

Experiment 937
Muonium in hexagonal semiconductors
(R.L. Lichti, Texas Tech)

TRIUMF Expt. 937 was given time specifically to investigate the differences in muonium behaviour in single crystal AlN compared to that in sublimation grown thick films or those deposited by CVD. We have obtained the temperature dependence of the qlcr resonances for a single crystal of AlN. The sample, obtained on loan from Crystal IS, Inc., had a cross section slightly under 80 mm^2 and was sufficiently thick to stop all muons hitting the sample; those hitting the Ag holder do not contribute to any resonance feature.

The main spectral features are associated with N neighbours of diamagnetic Mu^+ centres, specifically yielding information related to the sites and dynamics of these defects. The likely stable site for an isolated Mu^+ is a nitrogen anti-bonding location oriented into the channels formed by the 2H wurtzite stacking order, commonly noted as $AB_{\perp}[N]$. The other likely site based on our previous results in GaN is a second N anti-bonding location with Mu^+ inside the most tightly confined cage region of the structure. The strong qlcr line observed near 4.5 mT was initially assigned to this metastable $AB_{\parallel}[N]$ cage site.

For thick AlN films grown by CVD or sublimation techniques, the 4.5 mT resonance is strongest in samples with the smallest grain sizes or otherwise visually defective. Preliminary single crystal data at room temperature showed only a very weak resonance in this range, consistent with formation of the responsible Mu state primarily in defective regions. If this state requires migration of Mu^+ to a grain boundary or some other highly stressed region, one might expect the resonance to grow at higher temperatures where the main Mu^+ centre can rapidly diffuse through the crystal. Zero-field depolarization functions imply a second Mu^+ centre in AlN films. This state was assigned to the stable Mu^+ site and is mobile within the wurtzite channels. Hints in the depolarization data suggest a change from local tunneling to diffusive motion above 300 K in AlN films, but the details are highly sample dependent. Our main goal for Expt. 937 was to examine the temperature dependence of the 4.5 mT line in single crystal AlN.

Figure 139 shows the qlcr spectra for single crystal AlN at a few temperatures between 500 and 1050 K. The 4.5 mT line increases in intensity up to 800 K and then decreases at higher temperatures. The decrease is consistent with earlier data on AlN films which gave a state dissociation energy of 1.0 eV. This energy had been tentatively assigned to the cage to channel site change for Mu^+ based on initial signal identifications.

Figure 140 shows the T-dependent amplitudes for

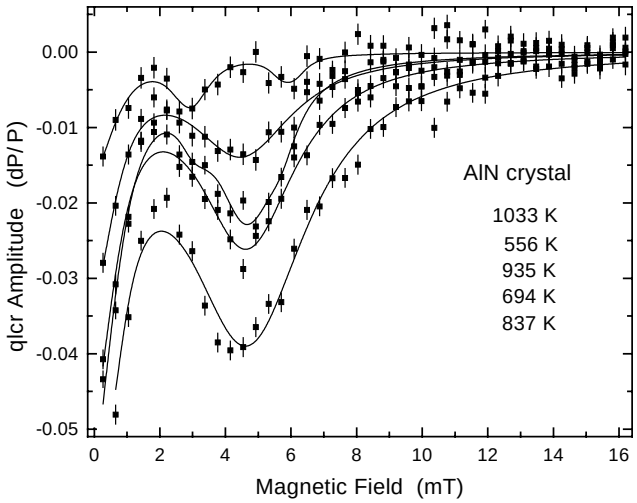

Fig. 139. The qlcr spectra obtained for single crystal AlN at several temperatures between 500 and 1050 K. The large resonance near 4.5 mT represents a trapped Mu^+ state.

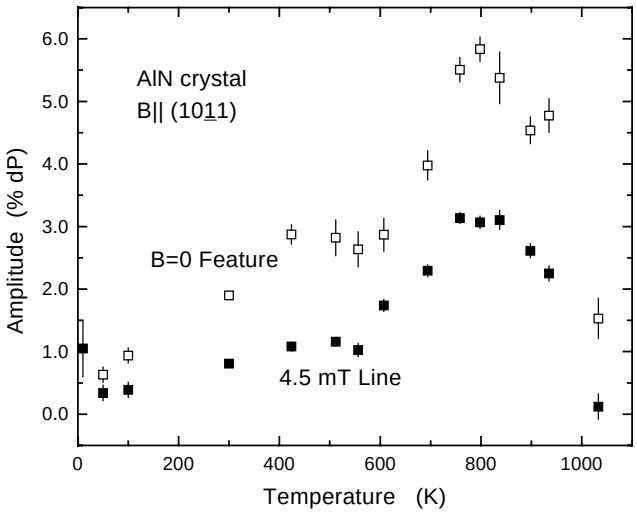

Fig. 140. Temperature dependence for the amplitudes of the main 4.5 mT qlcr line (filled squares) and the zero-field feature (open squares) due to non-resonant interactions.

the main qlcr line and the zero-field feature for this AlN crystal. The spectra for 935 and 1033 K have two additional lines present. These lines are from a different Mu^+ state (or states) and verify earlier conclusions that, at temperatures above the stability limit for the state responsible for the 4.5 mT resonance, Mu^+ can trap at another site, presumably paired with a specific, as yet undetermined, defect.

Because the T-dependence (and intensity) for the 4.5 mT line in various AlN samples is very different below 800 K, but very similar above 800 K, we conclude that the same trapped state is seen in films and single crystal samples, but that its formation is controlled by encounter rates between a mobile Mu centre and the relevant parent defect, grain boundary, or stressed region. These results suggest that this state is probably

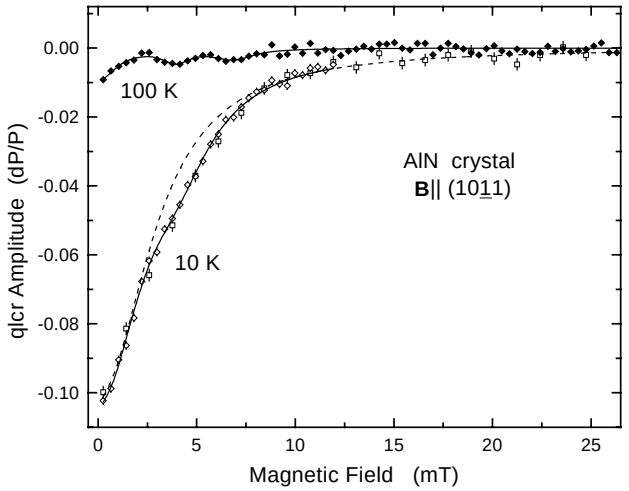

Fig. 141. Comparison of spectra taken at 10 K and 100 K displaying the large zero-field relaxation feature at the lowest temperatures. The 100 K data show a two-line qlcr spectrum shifted from that at 1000 K.

associated with an Al vacancy or a more extended defect rather than residing at the $AB_{\|}[N]$ cage site in the regular wurtzite lattice. Details of Mu^+ motion and an estimate of the density of trapping sites yielding the 4.5 mT qlcr resonance await zero-field depolarization measurements to quantify Mu^+ diffusion rates.

We took a few spectra at cryogenic temperatures. The resonance amplitudes are included in Fig. 140. The spectra at 50 and 100 K are basically consistent with the overall trends seen above room temperature. However, at 10 K there is a large-amplitude, broad zero-field feature reminiscent of II-VI materials that show a shallow-donor Mu^0 state. Figure 141 shows the 10 K and 100 K spectra for comparison. Hyperfine decoupling curves had earlier implied an atomic-like Mu^0 up to at least 300 K. No hyperfine precession signals have yet been observed for either a shallow or deep (atomic-like) Mu^0 in AlN. Either a neutral muonium state is present or a much different relaxation mechanism is active at 10 K compared to 50 K and above. Spectra at 300 K and below show two extra lines, similar to those near 1000 K but at higher fields, as well as a weak 4.5 mT line. It is not obvious whether or not these high-T and low-T extra resonances represent the same state.

Experiment 938
Muonium formation and ionization in semiconductors and insulators
(V.G. Storchak, Kurchatov)

Properties of impurities in semiconductors have been the subject of substantial experimental and theoretical interest due to their physical properties as well as important applications, most notably in studies of metal-insulator transition. Atomic hydrogen represents the simplest and the lightest impurity in semiconductors, therefore its electronic structure and dynamics are of special interest. Even so, very little is known about isolated hydrogen impurity in bulk semiconductors due to its high mobility and reactivity: most of our knowledge is accumulated on hydrogenic-impurity complexes in which hydrogen removes electrically active levels from the band gap and thus passivates electrical and optical activities of other impurities. As a result of binding with other impurities, hydrogen removes its own electrically active levels from the semiconductor band gap as well.

In this regard the technique of muon spin rotation/relaxation/resonance (μSR) has made a significant contribution in clarifying the electronic structure of the isolated state of muonium ($Mu = \mu^+e^-$) atom. The structure and dynamics of muonium in semiconductors have been suggested to be directly relevant to understanding the analogous hydrogen defect: Muonium has a reduced mass almost the same as that of H, so its electronic states and chemical interactions are literally those of a light hydrogen isotope ($m_\mu \simeq m_p/9$); as such, and with due regard to isotope effects, muonium is expected to provide an accessible model for isolated hydrogen defect centres in semiconductors.

In μ^+SR experiments one accumulates the necessary statistics into a time spectrum that reveals the spin polarization of positive muons stopped in the sample. Each incoming 4 MeV muon leaves behind an ionization track of excess electrons and ions liberated during the μ^+ thermalization process. Experiments in insulating and more recently in semiconducting media (Si and GaAs) have shown that the ionization track products are very close to the thermalized muon. (The characteristic distance is about $10^{-5} - 10^{-6}$ cm.) Some of the excess electrons generated in the end of the μ^+ track are mobile enough to reach the thermalized muon and form the muonium atom.

The phenomenon of delayed muonium formation described above implies that as the electron approaches the stopped muon it may be captured initially into an excited electronic state. In semiconductors with low electron effective mass and high dielectric constant, an electron and a positively charged centre can form a hydrogen-like weakly bound state with macroscopic-sized orbits. In particular in GaAs, the binding energy of such a shallow donor is $U \approx 7$ meV while its characteristic radius $a \approx 8 \times 10^{-7}$cm.

The phenomenon of formation of this weakly bound muonium centre may serve to model the process of a free electron capture (or electron localization) by an attractive centre. What is relevant to current studies is the magnetic-field effects on shallow-impurity (hydrogen-like) states. It is suggested that in semiconductors the presence of an external magnetic field en-

hances the binding energy of the impurity atom. The point here is the effect of competition of the magnetic energy and the Coulomb energy: when the magnetic field is strong enough so that cyclotron energy $\frac{1}{2}\hbar\omega_c$ is comparable or larger than Coulomb interaction, a considerable compression of the electronic wave function of the atomic state occurs because its orbital radius tends to decrease as the field is increased. This shrinkage of the wave function in turn causes the electron to be affected by stronger binding of the attractive Coulomb potential, and thus results in an increase of the ionization energy. This effect of magnetic freezing out could be observed as a decrease in number of conduction carriers due to thermal deionization against an increase of the field H.

In bulk semiconductors, the phenomenon of metal-insulator transition is typically studied using "electrical" techniques (such as measurements of magnetoresistance or Hall coefficient). In these experiments, however, the conclusion on electron localization is made indirectly based on measuring properties of the electrons "left" as delocalized and thus available for conduction. The phenomenon of delayed muonium formation via capture of the free electron by positive muon gives an opportunity to study the elementary act of metal-insulator transition. These studies are carried out in extremely dilute limit of a single impurity in the sample thus avoiding complications related to impurity-impurity interactions. Here we present the results of our study of magnetic freezing out of electrons into muonium atoms in GaAs in magnetic fields up to 7 T.

Muonium centres in semiconductors typically ionize above several hundred K, with the Mu^0_{BC} signals not observed above roughly 150–200 K in GaAs. Ionization of Mu^0_{BC} in GaAs is accompanied with an increase of the diamagnetic fraction (diamagnetic polarization). In the middle of the ionization curve it is very hard to detect the Mu^0_{BC} signal as it relaxes too fast. An influence of the magnetic field on muonium formation may, however, be studied by measuring the magnetic field dependence of the diamagnetic fraction: a decrease in diamagnetic signal amplitude signifies an increase of muonium fraction (although unobservable).

Figure 142 presents the magnetic field dependence of the diamagnetic polarization in GaAs at T=190 K. The diamagnetic signal amplitude in GaAs is normalized to that in Ag in order to take into account effects of the final time resolution of the spectrometer (it is known that in Ag 100% of polarization is diamagnetic). The data are normalized at every temperature point.

A significant decrease of the diamagnetic fraction is seen at high magnetic field (above about 1 T). We consider this decrease as a result of freezing out of free electrons into muonium atom energy level.

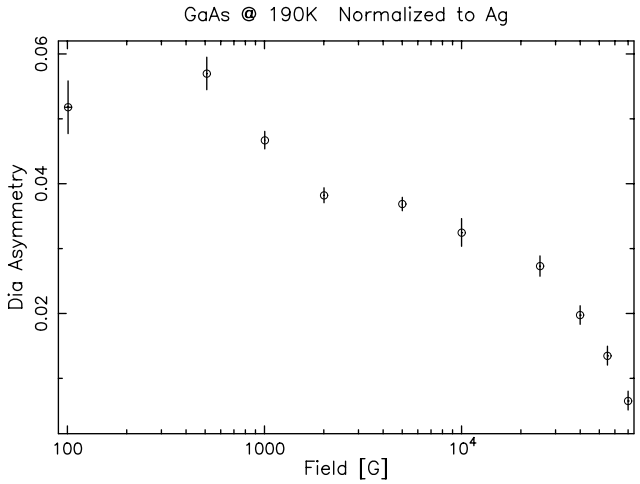

Fig. 142. Magnetic field dependence of the diamagnetic polarization in semi-insulating GaAs at T=190 K.

Experiment 939
Guest-host interactions and Hfcs of Mu-radicals in zeolites
(D.G. Fleming, UBC)

In Expt. 677, the guest-host interactions and hyperfine coupling constants (Hfcs) of the Mu-cyclohexadienyl radical were studied in various zeolites [Fleming *et al.*, J. Phys. Chem. **B106**, 6395 (2002)]. Particular focus was on the NaY, HY and USY zeolites for their distinct differences in SiO_2/Al_2O_3 ratio and charge-balancing-cation type. In the 2002 beam time of its successor, Expt. 939, the Mu-ethyl and Mu-*t*-butyl radicals in NaY and HY, formed by Mu addition to ethylene and isobutene, respectively, were investigated by both TF-μSR and ALC-μSR. Preparation of the alkene-loaded zeolites is identical to the technique used in Expt. 677. Two zeolite loadings were used in this experiment, 1 and 3 per supercage (SC). Here we report on the data obtained from ethylene- and isobutene-loaded NaY. Results from HY are incomplete and will be reported at a later time.

Figure 143 shows the Hfc data obtained for the Mu-*t*-butyl radical in NaY (3 per SC loading), compared to data for the same radical in bulk solid and liquid isobutene [Yu, Ph.D. thesis (SFU, 1989)]. For the temperature range of 150–300 K, the reduced muon Hfc ($A'_\mu = A_\mu/3.184$) curve follows a similar trend as seen in the liquid, albeit with somewhat higher values. At lower temperatures, 5–120 K, this trend also looks similar to that of solid isobutene, though with reduced values that also flatten out, likely due to "freezing" at the favourable low-T orientation of hindered rotation from the McConnell equation of β-Hfcs ($A(\theta) = L + M\langle\cos^2(\theta)\rangle$, where θ is the dihedral angle between the p_z-orbital of the free-radical electron and

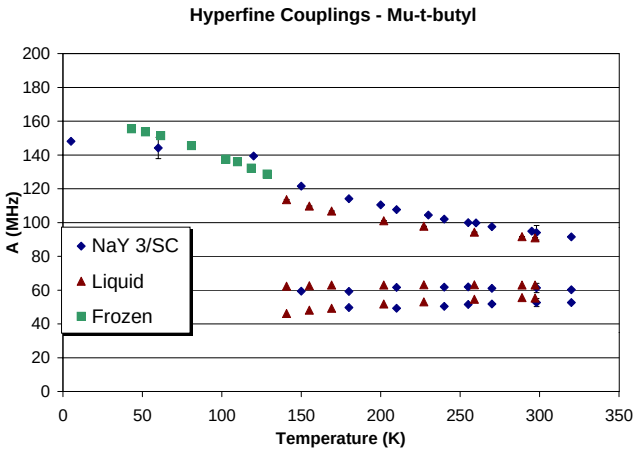

Fig. 143. T-dependence of the muon and proton Hfcs for the Mu-t-butyl radical compared in NaY zeolite (Expt. 939) and in the solid and liquid bulk. Note that the reduced muon Hfc ($A'_\mu = A_\mu/3.184$) is plotted.

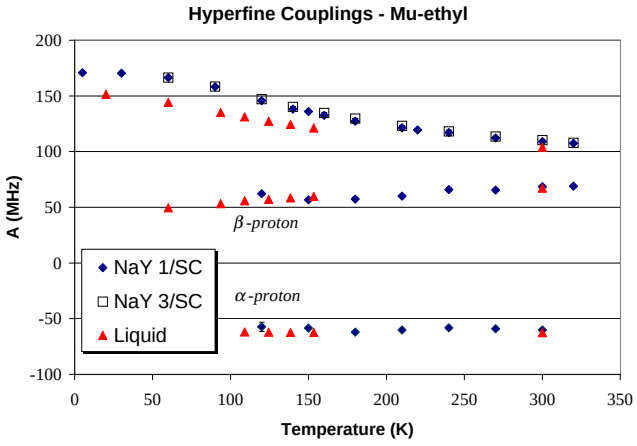

Fig. 144. Muon ($A'_\mu(T)$) and proton Hfcs for the Mu-ethyl radical in NaY zeolite at 1 and 3 per SC loadings (Expt. 939), compared with similar data in the bulk. Note that there is little or no loading dependence in the zeolite.

the β C-H bond). Both proton Hfc-temperature dependences are linear with slightly positive slopes, and are close to the values seen in liquid isobutene, though in the zeolite the proton couplings are 3 to 4 MHz lower than in the bulk.

Hfc data obtained for the Mu-ethyl radical in the NaY zeolite are shown in Fig. 144. Reduced muon Hfcs were obtained for loadings of both 1 and 3 per SC and show little loading dependence. When compared to data for the same radical in bulk ethylene and on a silica surface (not shown in figure) [Schwager *et al.*, Hyp. Int. **87**, 859 (1994)], deviations due to interactions with the zeolite framework begin to show. The temperature dependence of the muon Hfc ($A'_\mu(T)$) for the zeolite-loaded Mu-ethyl radical is ≈10% higher than found in the bulk, at lower temperatures, indicating enhanced binding to the Na^+ cation of NaY. In contrast, the proton Hfcs for both the α and β-protons are very similar to those found in the bulk (and on the silica surface), all seemingly giving (within errors) a linear trend with a very shallow slope. The α-protons (bound to the carbon radical centre) display essentially no temperature dependence, though the hyperfine couplings of the β-protons do show some intra-molecular rotational T-dependence, closely following the trend seen in the bulk. Future beam shifts will obtain more data for ethylene-loaded HY, as well as additional temperature points for ethylene and isobutene in NaY zeolite.

Experiment 940
Thermoelectrics II: μSR in layered manganese oxides
(J. Sugiyama, Toyota CRDL Inc.; J.H. Brewer, UBC-TRIUMF)

Perovskite manganites, $A\mathrm{MnO_3}$ ($A = AE_{1-ny}\mathrm{RE}_{ny}$, AE = Ca or Sr, RE = rare earth element), are known to exhibit n-type conductivities, if the average valence of Mn ions ≥ 3.5 [Hejtmanek *et al.*, Phys. Rev. **B60**, 14057 (1999); Martin *et al.*, *ibid.*, **B62**, 6442 (2000)]. In addition, both transport and magnetic properties are reported to depend on the average ionic radius of the A-site ions. That is, for $(\mathrm{Sr}_{1-x-y}\mathrm{Ca}_x\mathrm{RE}_y)\mathrm{MnO_3}$ ($0 \le x \le 0.92$, y ∼0.1), the dependence of the resistivity ρ(573 K) on the tolerance factor Γ exhibits a broad minimum at around Γ ∼0.96 [Hirano *et al.*, Meeting Abstract, Phys. Soc. Japan **57**, 556 (2001) (in Japanese)] (see Fig. 145),

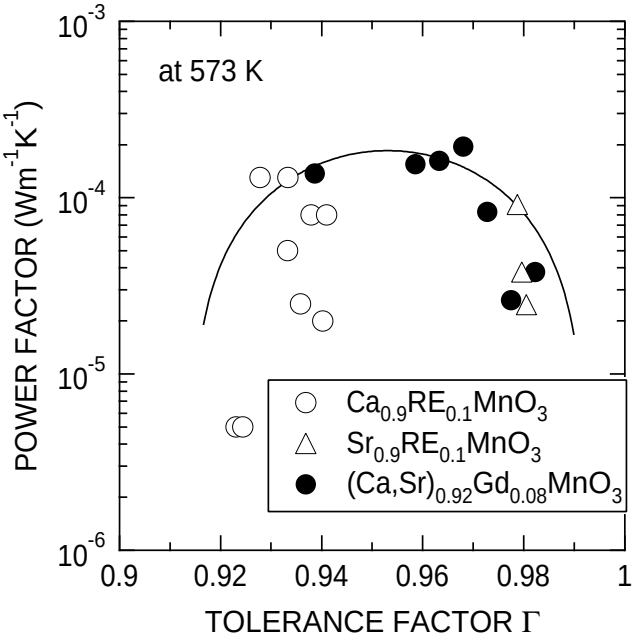

Fig. 145. Thermoelectric power factor ($=S^2/\rho$) at 573 K as a function of tolerance factor Γ of various $(\mathrm{Sr}_{1-x-y}\mathrm{Ca}_x\mathrm{RE}_y)\mathrm{MnO_3}$ samples, where y ∼0.1 and RE = rare earth elements. Since S is approximately independent of Γ, ρ exhibits a broad minimum at Γ ∼ 0.955.

where $\Gamma = (r_A + r_O)/\sqrt{2}(r_B + r_O)$; r_A, r_B and r_O are the ionic radii of the A-site, B-site and oxygen, respectively. This is considered to be a typical "chemical pressure effect" on ρ induced by the substitution of Sr by Ca. Since the Seebeck coefficient S is found to be insensitive to Γ, the magnitude of the thermoelectric figure of merit $ZT = S^2T/(\rho\kappa)$ (where T is the absolute temperature and κ is the thermal conductivity) approaches ∼0.18 at 800 K; this is the highest ZT value for manganese oxides at present.

According to dc susceptibility (χ) measurements on $(Sr_{0.92-x}Ca_xGd_{0.08})MnO_3$, antiferromagnetic (AFM) transitions were observed for the samples with $x \leq 0.5$, whereas ferromagnetic (FM) transitions for the samples with $x \geq 0.8$ (see Fig. 146). It should be noted that the highest thermoelectric power factor ($= S^2/\rho = Z/\kappa$) was obtained for the sample with $x \sim 0.5$ ($\Gamma \sim 0.96$); that is, in the phase boundary between AFM and FM phases. Therefore, the competition between AFM and FM interactions seems to be significant to increase ZT. Indeed, both direct and superexchange interactions between Mn ions should be altered by the substitution of Sr by Ca without a change in carrier concentration. In order to investigate the change in magnetism as a function of x, i.e., chemical pressure, we measured both weak (∼100 Oe) transverse-field (wTF-) μ^+SR and zero field (ZF-) μ^+SR time spectra in $(Sr_{0.92-x}Ca_xGd_{0.08})MnO_3$.

Figures 147(a) and (b) show the temperature dependences of the paramagnetic asymmetry A_{para} and the corresponding relaxation rate λ_{para} in the three $(Sr_{0.92-x}Ca_xGd_{0.08})MnO_3$ samples. The large decrease

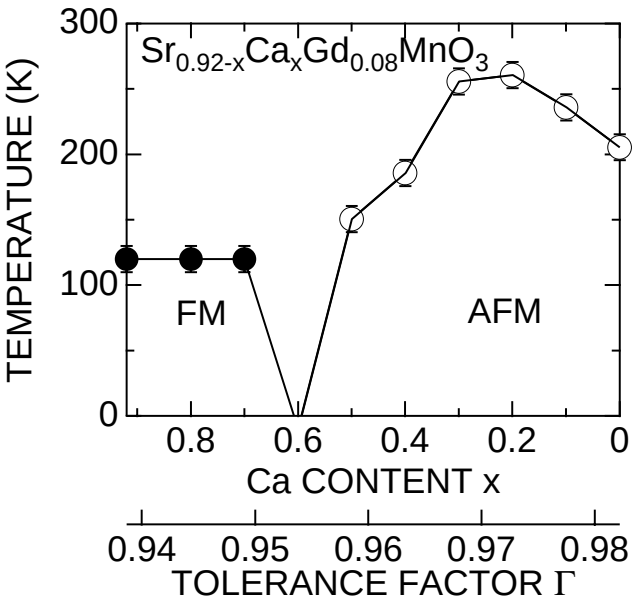

Fig. 146. Magnetic phase diagram of $(Sr_{0.92-x}Ca_xGd_{0.08})MnO_3$ determined by dc susceptibility measurements.

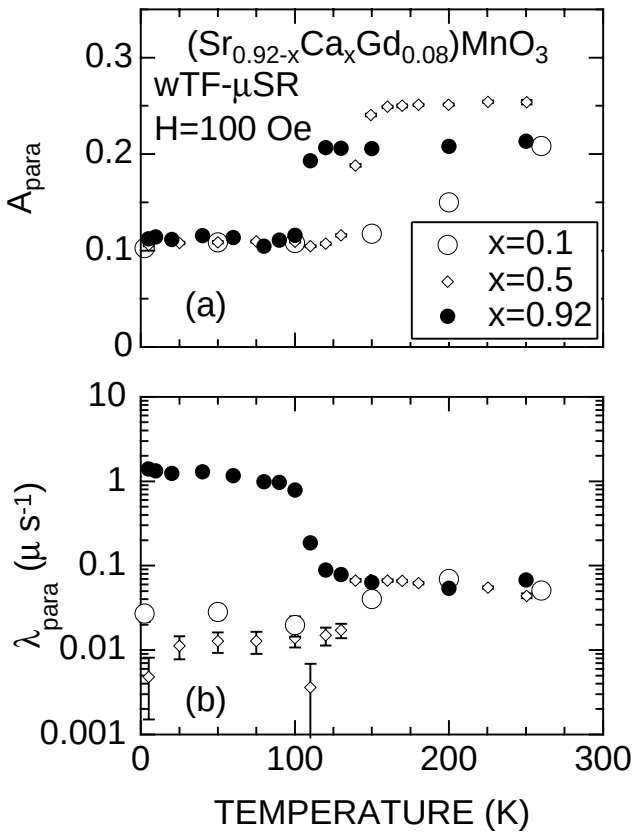

Fig. 147. (a) Paramagnetic asymmetry A_{para} and (b) relaxation rate λ_{para} as a function of temperature for the three $(Sr_{0.92-x}Ca_xGd_{0.08})MnO_3$ samples.

in A_{para} is clearly observed at T_C/T_N. On the other hand, as temperature decreases from 300 K, λ_{para} decreases at T_N, while it increases at T_C. It is worth noting that $A_{para} \sim 0.1$ even at 0 K for all the three samples indicating the phase separation, as reported for several perovskite manganites [Martin *et al., op. cit.*; Moritomo *et al.*, Phys. Rev. **B64**, 214409 (2001)]. Furthermore, ZF-μ^+SR spectra of the three samples at 2.5 K showed no muon precessions but probably very fast relaxations. This suggests an inhomogeneous or a fast fluctuating distribution of an internal magnetic field.

Experiment 942
Magnetic fluctuations near metal-insulator transitions in ruthenate pyrochlores
(S. Dunsiger, LANL; R. Kiefl, UBC)

The nearly free electron model may often successfully describe the band structure of a crystal, the highest band being completely filled for insulators or only partially so for metals. However, many transition metal oxides with partially filled d-electron bands have nonetheless been found to be poor conductors or indeed insulators. The origin of this behaviour is thought to be the Coulomb repulsion between electrons: strong

electron-electron correlations. Indeed, an otherwise insulating material may be driven into a metallic state in a controllable way with doping, chemical composition, pressure or magnetic field. Such metal-insulator transitions are widely observed in condensed matter physics.

The scientific interest in these materials is based on the fact that near the transition point the metal shows fluctuations of spin, charge and orbital degrees of freedom. There has been extensive theoretical and experimental work in the past 60 years to explain metal-insulator transitions driven by strong electron-electron correlations. Muon spin relaxation is one of the principal methods we use to characterize the dynamic behaviour since it is uniquely sensitive to the low frequency magnetic fluctuations which are often present in these systems.

The focus of Expt. 942 is the study of pyrochlores with chemical composition $A_2B_2O_7$ where only the B site is occupied by a magnetic ion, in particular $Y_{2-x}Bi_xRu_2O_7$. This system may be driven in a controlled manner from a geometrically frustrated insulator, $Y_2Ru_2O_7$, to a Pauli paramagnetic metal with increasing Bi doping.

Susceptibility measurements on $Y_2Ru_2O_7$ by Yoshii *et al.* [J. Phys. Soc. Jpn. **68**, 3034 (1999)] yield a Curie-Weiss temperature of $\Theta_{CW} = -1000$ K, indicating antiferromagnetic interactions between Ru moments. The system undergoes an ordering transition at $T_G \sim 76$ K. This suppression of T_G relative to Θ_{CW} is characteristic of a geometrically frustrated system. Macroscopically, the susceptibility of $Y_2Ru_2O_7$ is history dependent below the ordering temperature. Yoshii *et al.* argue that the observed behaviour is evidence of a spin glass transition. However, recent neutron diffraction studies [Ito *et al.*, J. Phys. Soc. Jpn. **69**, 888 (2000)] show an increase in intensity of resolution limited 111 and 220 reflections below the transition temperature. This is consistent with a non-collinear antiferromagnetically long range ordered state, even though the system appears spin glass-like macroscopically.

Muon spin relaxation measurements on four members of the family $Y_{2-x}Bi_xRu_2O_7$ (x = 0, 0.9, 1, 2) were undertaken during the autumn of 2002 on the M20 beam line at TRIUMF. The measurements were taken in a longitudinal field of 15 Oe. Above the transition temperature, the muon spin depolarization in $Y_2Ru_2O_7$ is too slow to be observed. This is likely because of the large value of the exchange coupling between Ru moments and associated rapid Ru spin fluctuation rate in the paramagnetic regime. In low longitudinal field experiments in the "motionally narrowed" limit of rapid spin fluctuations, the muon spin depolarization may be characterized by a single exponential $\exp(-t/T_1)$, where

$$1/T_1 = \frac{2\Delta^2}{\nu}.$$

The second moment of the internal magnetic field B_i ($i = x, y, z$) is given by $\Delta^2/\gamma_\mu^2 = \langle B_i^2 \rangle$, of the order of 1–2 kOe in $Y_2Ru_2O_7$; ν is the mean fluctuation rate for fluctuations in B_i, and γ_μ is the muon gyromagnetic ratio. As may be seen in Fig. 148, spontaneous muon spin precession develops below 76 K. This indicates a well defined static local magnetic field at the muon site, consistent with long range order. The precession frequency increases as the temperature is reduced, as a measure of the growing sublattice magnetization (see Fig. 149).

Doping with Bi on the Y site increases the lattice constant and the system becomes progressively more metallic as the Bi $6p$ states mix with $4d$ states of Ru

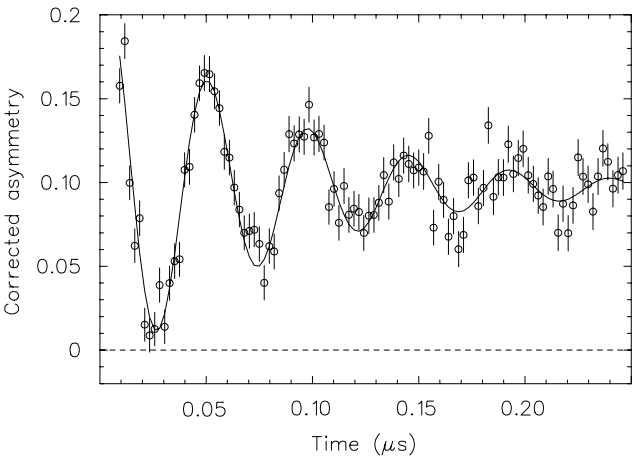

Fig. 148. Typical muon spin depolarization spectrum of $Y_2Ru_2O_7$ taken in a longitudinally applied field of 15 Oe at T = 2.4 K.

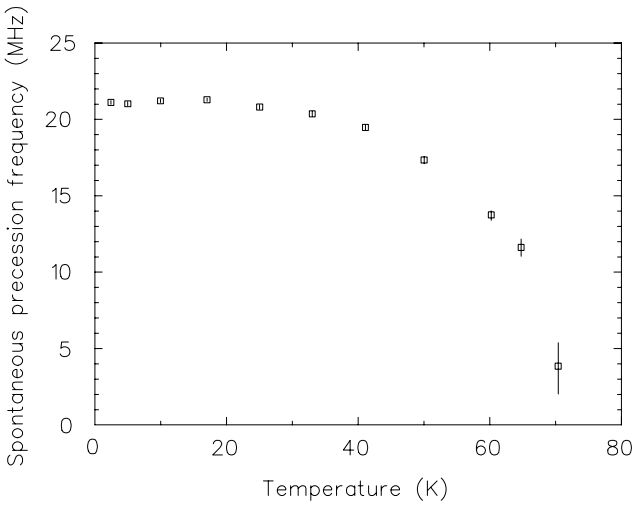

Fig. 149. Spontaneous muon spin precession frequency in $Y_2Ru_2O_7$ as a function of temperature.

via the framework oxygen [Cox *et al.*, J. Solid State Chem. **62**, 360 (1986)]. The ordering transition temperature is also suppressed and broadened. Muon spin relaxation measurements on $Y_{2-x}Bi_xRu_2O_7$ ($x = 0.9$, 1.0) in a longitudinally applied field of 15 Oe are summarized in Figs. 150 and 151. As the temperature is reduced, two components are observed in the signal: an increasingly rapid initial loss of polarization and a slowly relaxing "tail". The data have been analyzed using the fitting function

$$G_Z(t) = A_1 \exp[-(\lambda_1 t)^\beta] + A_2 \exp[-\lambda_2 t].$$

The peak in λ_2, the muon depolarization rate of the tail, corresponds to a peak observed in the zero field cooled dc susceptibility and the onset of history dependent behaviour. This is indicative of a freezing of the Ru spins. The depolarization rate λ_1 gives a measure of the static, highly disordered internal magnetic field which develops with decreasing temperature.

Bulk measurements by Yoshii *et al., op. cit.* indicate that the metal-insulator transition point occurs in $Y_{1.1}Bi_{0.9}Ru_2O_7$. It is interesting to note that as the metal-insulator transition is approached, the specific heat coefficient γ and Pauli paramagnetic susceptibility are enhanced compared to values expected from band theory. This attribute reflects a thermal effective mass m^* of the conduction electrons which is orders of magnitude larger than the bare electron mass. The effect is usually believed to derive from strong correlations.

From published work [Yoshii *et al., op. cit.*], T_G is expected to go to zero in $Y_1Bi_1Ru_2O_7$. The higher transition temperatures observed in the 2 non-stoichiometric samples used in our μSR study (see Fig. 151) indicate a lower Bi concentration than anticipated. The cause of this difference is currently under investigation.

Finally, as anticipated, the muon spin depolarization rate in $Bi_2Ru_2O_7$ is too slow to be observed using the μSR technique. This is fully consistent with the rates associated with Korringa relaxation in a normal metal [Abragam, Principles of Nuclear Magnetism (Clarendon Press, Oxford, 1961)].

Further μSR measurements on the family of compounds $Y_{2-x}Bi_xRu_2O_7$ are planned. In particular, new samples of $Y_{1.1}Bi_{0.9}Ru_2O_7$ and $Y_1Bi_1Ru_2O_7$ will be investigated, to shed light on the enhanced magnetic fluctuations associated with the metal-insulator transition.

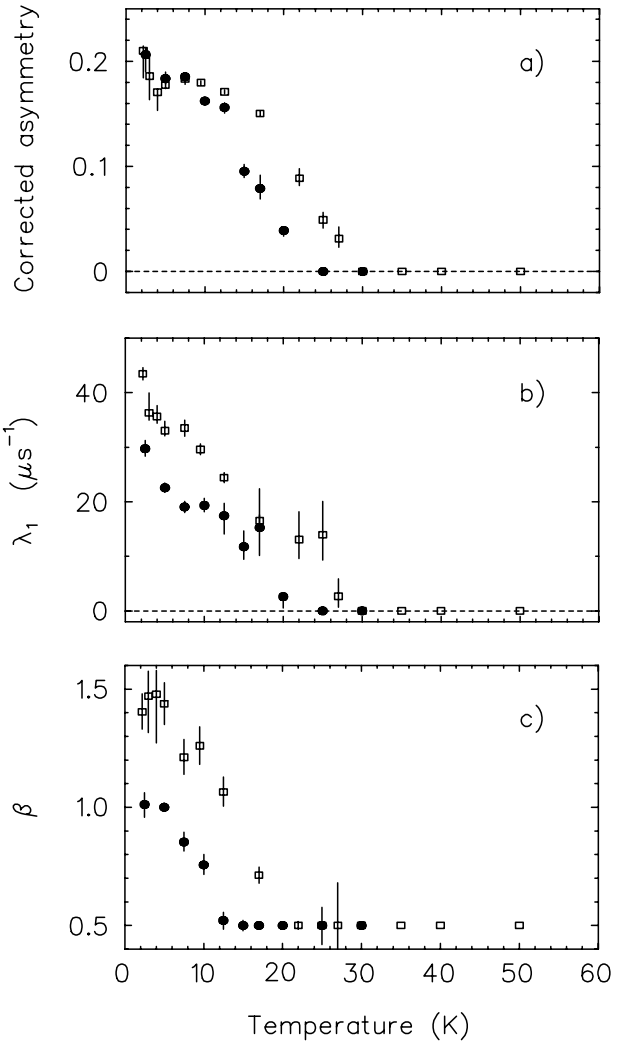

Fig. 150. (a) Corrected asymmetry A_1, (b) muon spin depolarization rate λ_1 and (c) parameter β as a function of temperature in $Y_{2-x}Bi_xRu_2O_7$ ($x = 0.9$, 1.0) in a longitudinally applied field of 15 Oe. The fitted function is described in the text. Filled circles and unfilled squares indicate data on $YBiRu_2O_7$ and $Y_{1.1}Bi_{0.9}Ru_2O_7$, respectively.

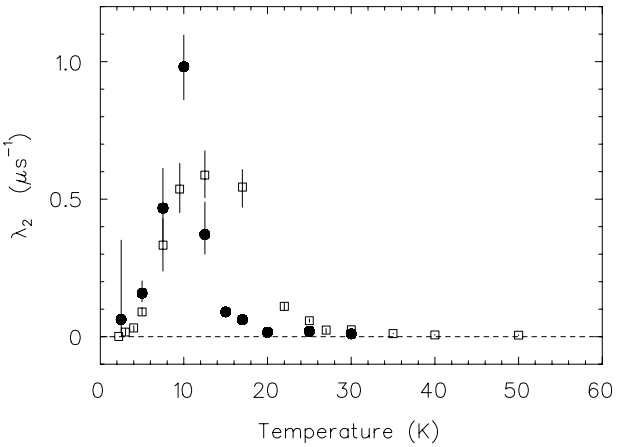

Fig. 151. Muon spin depolarization rate λ_2 as a function of temperature in $Y_{2-x}Bi_xRu_2O_7$ ($x = 0.9$, 1.0).

Experiment 943
Muonium and muoniated free radical formation and reactivity in sub- and supercritical carbon dioxide
(K. Ghandi, SFU)

The purpose of Expt. 943 is to study: 1) the radiation chemistry, 2) the free radical chemistry and 3) chemical kinetics of transient species in supercritical CO_2 ($ScCO_2$) and $ScCO_2$/cosolvents at the microscopic level using μSR as the experimental tool. These three areas are closely related by the common theme of green chemistry, a topic of significant recent interest (the entire ninth issue of 2002 Acc. of Chem. Res. was devoted to this topic).

Before giving the report on different stages of the project, we will list only a small number of the questions that were planned to be tackled during the course of this study:

1. Are these experiments feasible? Are muonium and diamagnetic species long lived under sub- and supercritical conditions?
2. Can radiation chemistry be tuned with the solvent thermodynamic state under sub- and supercritical conditions?
3. What kind of free radicals would react with CO_2 under sub- and supercritical conditions?
4. Are free radicals free or do some complex with CO_2?
5. Under what conditions are the fluctuations of the solvent cage significant?
6. Can we tune the electron wave functions of a radical by applying modest pressure in a supercritical fluid?
7. Under what conditions and for what kind of radicals do solvent cages exist? If there is a significant change in the solvent cage, how would that affect hyperfine interactions and chemical kinetics?
8. What are the optimum thermodynamic conditions for different types of reaction?

We have answered several of these questions during one-week (fragmented) data-taking at M9 and M15. Studies were first carried out in standard samples. This determined the scaling factors to convert muon signal amplitudes to fractions of initial polarization: PD, diamagnetic fraction, PMu, muonium fraction and PL = 1 – PD – PMu, the "missing fraction", which is of particular interest since it points to the mechanism of muon depolarization in the radiolysis environment. The muon spin precession frequencies were used to distinguish between muons in the muonium atom and those incorporated in diamagnetic molecules. The diamagnetic signals were measured in experiments at fields around 100 G and muonium signals were

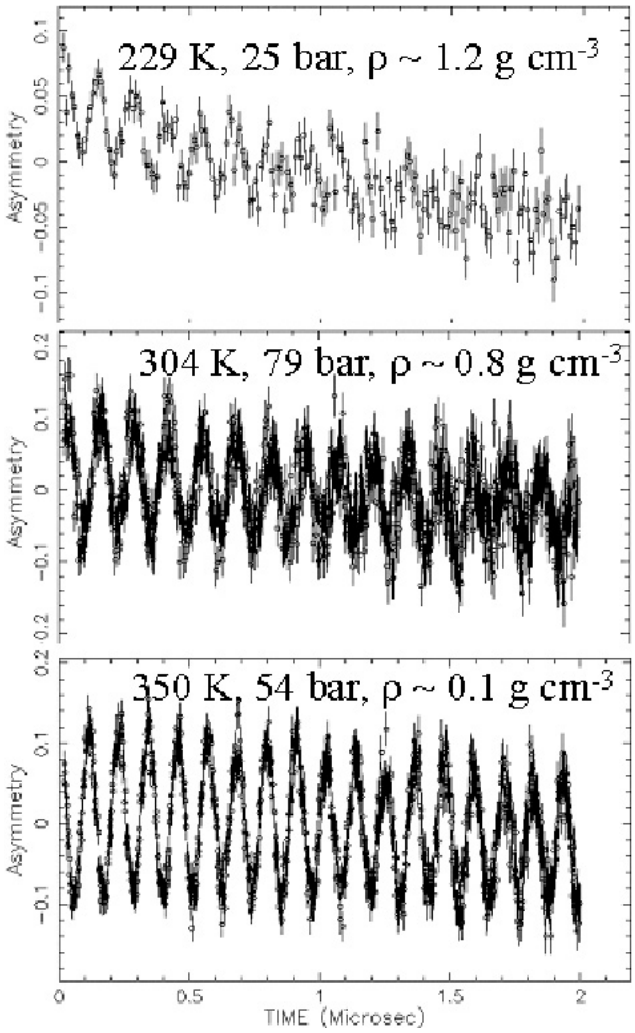

Fig. 152. Mu precession at 6G in CO_2.

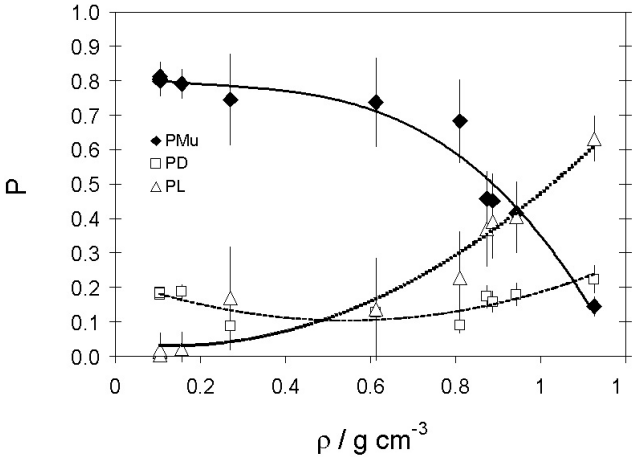

Fig. 153. Mu, diamagnetic and missing fraction in CO_2.

measured in fields smaller than 8 G, where a single frequency was detected (Figs. 152 and 153).

Based on our result, the answer to question 1 is that the experiment is feasible since Mu is formed and

long lived over a broad range of conditions from liquid to supercritical conditions (Fig. 152). However, the Mu fraction changes with density (Fig. 153). This may suggest that radiation chemistry can be tuned with the solvent thermodynamic state under sub- and supercritical conditions (question 2). More detailed studies are necessary to understand the factors affecting this significant change in Mu fraction.

At this stage our answer to question 3 is only limited to the reaction of Mu with CO_2 and our data suggest that Mu does not react with CO_2 under the conditions we have studied (thermal Mu does not add to CO_2). The only suspicious conditions are at very low temperature (–40°C) where the relaxation was significant (0.8 μs), which needs more experiment to explore the cause of this high relaxation; under all other conditions the maximum background relaxation was less than 0.3 μs.

A magnetic field around 100 G, transverse to the muon polarization was used to determine the hyperfine coupling in muonium. At these intermediate fields the muonium precession signal splits into two (Fig. 154). The splitting was used to determine muon hyperfine coupling in muonium. The results are presented in Fig. 155 and suggest that Mu is free at lower pressure (question 4) since the hyperfine coupling is not much different from the value for vacuum Mu, but at higher densities there is a significant intermolecular interaction between Mu and CO_2 molecules.

The local minimum close to the critical density probably suggests that the fluctuations of the solvent cage are significant under these conditions and lead to local density enhancement (question 5). Theoretical calculations to describe these results are in progress, however, the result itself is very significant since it shows that we can tune the electron wave functions of as simple a radical as Mu by applying modest pressure in a supercritical CO_2 (question 6).

To answer question 7 we need to study the temperature dependence of hyperfine interactions at constant densities, which is in our future plans.

In our original proposed plan for these experiments, we listed studies for the reactions of Mu with O2 and Br2. The first one was to study diffusion process and cage effects in $ScCO_2$ while the latter was a chemical reaction with no electronic barrier. In the interim we changed our plans and studied instead the reaction between Mu and NO for two reasons: 1) Br2 is corrosive and the addition reaction with NO is similar to Br2 in that both have no electronic barrier; 2) by studying Mu decay rates at two fields, one less than 8 G and one around 80 G, we could determine both the spin exchange rate and addition rate. Our preliminary results are shown in Figs. 155 and 156. Much more experimental data is needed but even from this little amount of data we can see that the addition of Mu to NO and likely to small molecules in general is much more efficient in $ScCO_2$ compared to the other usual moderators, particularly at higher densities.

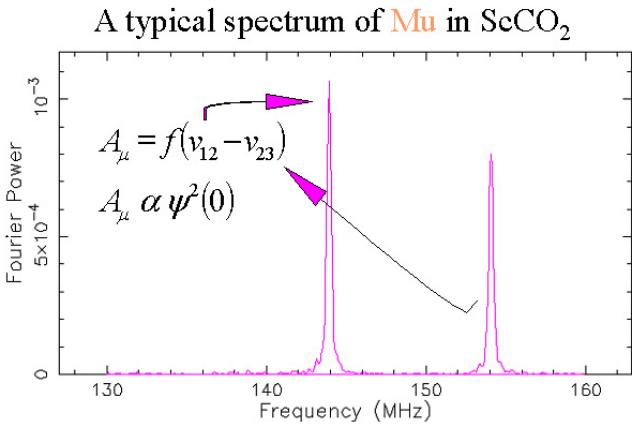

Fig. 154. $v12$ and $v23$ frequencies of Mu in 100 G magnetic field.

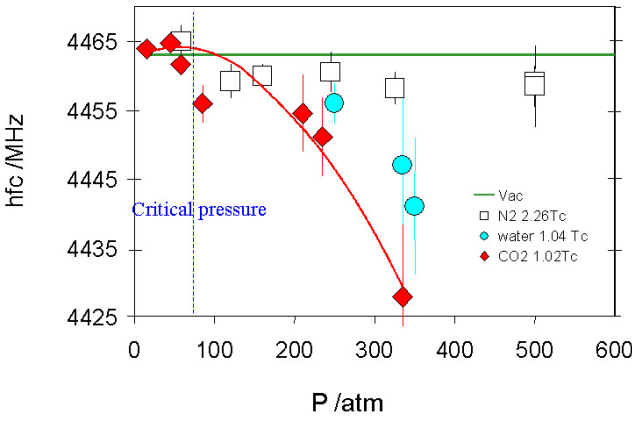

Fig. 155. Hyperfine coupling constants of Mu in $ScCO_2$.

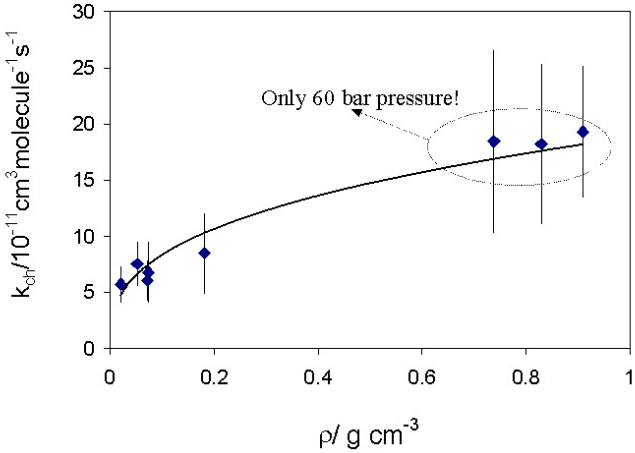

Fig. 156. Rate constants of Mu addition to NO in CO_2.

Experiment 944
Muonium in silicon carbide
(R.L. Lichti, Texas Tech.; K.H. Chow, Alberta)

TRIUMF Expt. 944 received its initial week of beam time late in 2002. Our main goal was to examine high frequency spin precession spectra for the three main structural phases of SiC; namely 3C, 4H, and 6H. High resistivity wafers of the two hexagonal structures were obtained commercially: the original source was Cree, Inc. The 3C sample is n-type at 2×10^{16}cm^{-3} and was provided by H. Nagasawa, Hoya Corp., from their substrate development program. The experiment was performed with the HiTime spectrometer in M15.

Our initial intent was to confirm the hyperfine values and then examine the temperature dependence for the three Mu^0 signals previously observed in 6H-SiC [Patterson *et al.*, Hyp. Int. **32**, 625 (1986)] and the two states seen in 4H-SiC. Cubic 3C-SiC is predicted to give a shallow donor state for H or Mu [Deak *et al.*, J. Phys. Cond. Mat. **13**, 9019 (2001)].

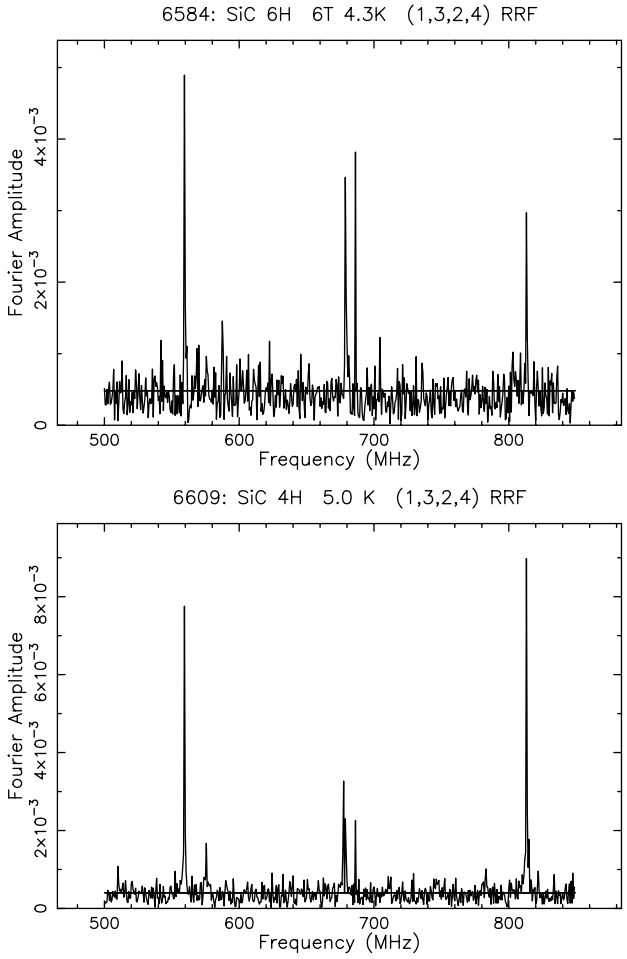

Fig. 157. Low temperature hyperfine spectra for 6H-SiC and 4H-SiC in a field of 6.0 T applied along the c-axis. The diamagnetic line is at 813 MHz and the other lines represent negative frequencies for Mu^0 ν_{12} transitions.

Figure 157 shows precession spectra obtained at low temperatures for the 6H and 4H structural phases. In both cases the magnetic field was nominally applied along the hexagonal c-axis, i.e. (0001). There do indeed appear to be three Mu^0 signals in 6H-SiC; however, these are not consistent with published hyperfine values. Spectra at higher temperatures imply that all three states are still there at 300 K in the present 6H sample, again contrary to earlier reports. The present data yield hyperfine values of 2826, 2984, and 2999 MHz for the three Mu^0 states at 4 K.

Figure 158 shows the detailed temperature dependence for the amplitudes and relaxation rates of each Mu^0 line and the diamagnetic signal in the 6H sample. The origin of the large amplitude variation for the Mu^0 states around 150 K is not understood at present. It is not completely reflected in the diamagnetic amplitude, and thus may represent Mu^0 motion in part. However, the hyperfine constants vary as expected for

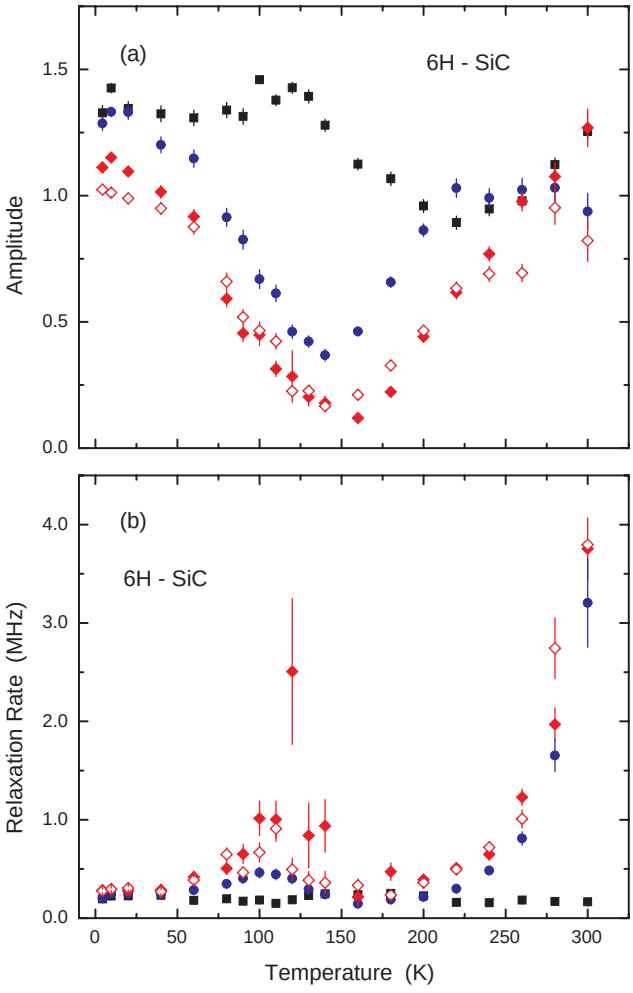

Fig. 158. Temperature dependence for amplitudes (a) and relaxation rates (b) for 6H-SiC (squares (black), μ^+, 813 MHz; circles (blue), Mu1, 559 MHz; filled diamonds (red), Mu2, 678 MHz; open diamonds (red), Mu3, 687 MHz).

individual Mu^0 states, so transitions among different types of Mu^0 sites are apparently not observed since that should lead to motional averaging of the relevant frequencies. The rate increase above 200 K is likely due to ionization. Higher temperatures are needed for confirmation.

In the case of 4H, five Mu^0 signals may be present at the lowest temperatures: the 678 MHz line appears to be split. Thus far we have only one other spectrum at 100 K where a single weak Mu^0 line is seen. It is not obvious whether the unexpected additional signals at low T are from a possible inclusion of a different structural phase (15R may be present and would have both 4H and 6H type sites) or from impurity-related sites. Most of the Mu^0 signals in 4H are very close to a 6H frequency.

We did not observe any Mu^0 signals in the n-type cubic (3C) SiC crystal. There is, however, a significant amount of relaxation in the diamagnetic signal which must arise from interactions between the muon and conduction electrons or with a magnetic impurity, given the very low fraction of host Si or C nuclei with magnetic moments. Both the absence of spectral evidence for a shallow donor and evidence of interactions between the muon and electrons in this sample are consistent with low-field results from measurements at ISIS a few months earlier.

We will need to examine additional samples of all three structures and obtain a more detailed temperature dependence for the 4H phase before drawing too many conclusions concerning differences with the older data and possible origins for the unexpected additional Mu^0 signals.